1991

Projection Presaturation: A New Approach To Producing Conformal Selective Excitation In Magnetic Resonance

Saryu Singh

PROJECTION PRESATURATION: A NEW APPROACH TO PRODUCING CONFORMAL SELECTIVE EXCITATION IN MAGNETIC RESONANCE

by

Saryu Singh

Department of Medical Biophysics

Submitted in partial fulfilment
of the requirements for the degree of
Doctor of Philosophy

Faculty of Graduate Studies
The University of Western Ontario
London, Ontario
April 1991

ISBN 0-315-66306-5

Canada

ABSTRACT

In recent years, several techniques of volume-selective excitation for extracting signals from a chosen region in a large sample have appeared for various applications in magnetic resonance (MR). Most of these techniques suffer from, at least, the T_2-decay problem, which rules out their application for short T_2 species. The remaining methods, while not suffering from the above limitation, are generally sensitive to errors in the radio frequency (rf) tip-angle and imperfections in rf profile, which cause inaccurate localization.

To overcome these problems, I have devised a new method for multi-dimensional spatial localization by accurate outer volume suppression. The method uses a series of selective rf pulses and a rotating gradient to saturate only the region outside the region(s) of interest (ROI), whose magnetization remains ideally unaffected during the localization. The magnetization within the ROI(s) is then interrogated with a readout pulse to acquire data. Suppression of the outer volume signal as well as signal loss from the ROI caused by rf imperfections are approximately estimated theoretically and compared against the measured values. The method virtually eliminates the tip-angle errors, greatly reduces the imperfections in rf profile, and thus increases the accuracy of localization.

Analytical methods are presented to design the rf pulses to localize one or more ROIs, whose shape and size can be tailored to match *in vivo* targets at arbitrary positions. Experimental results from a phantom and animal study using an MR imager demonstrate that ROIs of various shape and size (*e.g.* single or multiple cylindrical ROIs of circular, square, elliptical, etc., cross-section) at arbitrary positions within a 3D volume can be

localized by suppressing (> 99.9%) the magnetization of unwanted regions in 30 - 60 ms. Also shown are the efficacy of the method ir suppressing flow and aliasing artifacts in MRI, and in acquiring spectral/relaxometric data from a ROI.

The technique is suitable for short T_2 species, as it does not suffer from the T_2-decay problem. Most importantly, it can be implemented on any existing commercial MR scanner, as it does not require any special hardware. Because the method is accurate and versatile, it has many applications in MR.

ACKNOWLEDGMENTS

It is my pleasure to thank the members of my research Advisory Committee, Drs. B. K. Rutt (academic advisor), C. P. S. Taylor, A. Fenster, and T. Y. Lee for their advice, guidance and encouragement throughout my research work. The work reported in this thesis was carried out under the supervision of Dr. Brian K. Rutt. I must acknowledge his supervision of this research. In particular, I appreciate much of the help of Dr. Taylor for his valuable comments and suggestions on the preparation of the manuscript of this thesis. Helpful comments on the manuscript from Drs. A. Fenster and T. Y. Lee, and discussion with Dr. Sandy Napel are also appreciated.

I am indebted to the Department of Medical Biophysics at Western for providing me the opportunity of pursuing my graduate work here. The research work reported in this thesis was carried out on a Bruker Biospec magnetic resonance imaging system in the Imaging Research Laboratories of the John P. Robarts Research Institute. I acknowledge the help and generousity of Dr. Stephen J. Karlik for letting me use the Bruker imaging system.

Finally, I must acknowledge the Medical Research Council (MRC) of Canada for providing me an MRC studentship for the entire period (1988-91) of this research work. Partial funding received from the MRC, and the University through the department of Medical Biophysics is also acknowledged.

TABLE OF CONTENTS

LIST OF PHOTOGRAPHIC PLATES

LIST OF TABLES

LIST OF FIGURES

CHAPTER 1

Introduction

1.0

Spatial localization of a small region of interest (ROI) within a relatively large volume is becoming increasingly popular in nuclear magnetic resonance (NMR), since, a number of fruitful studies (some of which will be described later in this thesis) can be performed on such ROIs. While several methods for localizing a ROI have been published, I propose in this thesis a new approach to localization. In reviewing the present status of methods of localizing ROIs by NMR, it seems appropriate to begin with a brief introduction to the phenomenon of NMR itself.

1.1 *Background*

1.1.1 *NMR: A Nuclear Phenomenon*

Simply rephrasing that NMR is the abbreviated form of nuclear magnetic resonance does not convey much information unless the words nuclear, magnetic, and resonance are adequately explained. In the next few paragraphs, I will describe these phenomena as they appear in the sequence.

The term nuclear is a derivative of nucleus, which is a tiny core of atom. Atoms make up the elements of our universe. Certain atomic nuclei (nuclei of odd number of nucleons (protons or neutrons)) possess angular momentum arising from their inherent property of rotation or *spin*, a property first suggested by Austrian physicist Wolfgang

Pauli in 1924 to explain the fine structure of atomic spectra. Since nuclei bear charges, the spin corresponds to a current flowing about the spin axis, which, in turn, generates a small magnetic field. Thus, each nucleus of nonzero spin has a magnetic dipole moment.

In general, these dipoles point in random directions and the net effect will be a macroscopic or bulk magnetization vector in the sample of material of magnitude zero. When they are placed in a static magnetic field, the dipoles will tend to reorient themselves with the field's lines of force despite the randomizing effect of thermal motion. For nuclei of spin 1/2 (*e.g.*, hydrogen nuclei), quantum mechanics shows that there can be only two orientations of the dipoles: spin "up" which is parallel to the field, the lower energy state, and spin "down", antiparallel to the field, the higher energy state. In the case of protons (*i.e.* hydrogen nuclei), the difference in the number of dipoles between these two states is small: one part in 10^8, with slightly more dipoles oriented in the direction of the static field. This difference gives rise in the material sample placed in the static magnetic field to a net nonzero bulk magnetization vector **M**, which points in the direction parallel to the static field $\mathbf{B}_0$. Conventionally, this direction is defined as the z axis, as shown in Fig. 1.1a.

If the bulk magnetization vector **M** is tipped away from the z direction, **M** will precess about the z axis, analogous to a top or gyroscope precessing about the earth's gravitational field, because of the angular momentum of this system. Such a tipping can be achieved by applying a small rotating magnetic field, $\mathbf{B}_1$ (in the x'-y' plane), orthogonal to the static (nonrotating) magnetic field. The (x', y', z'=z) refers to the

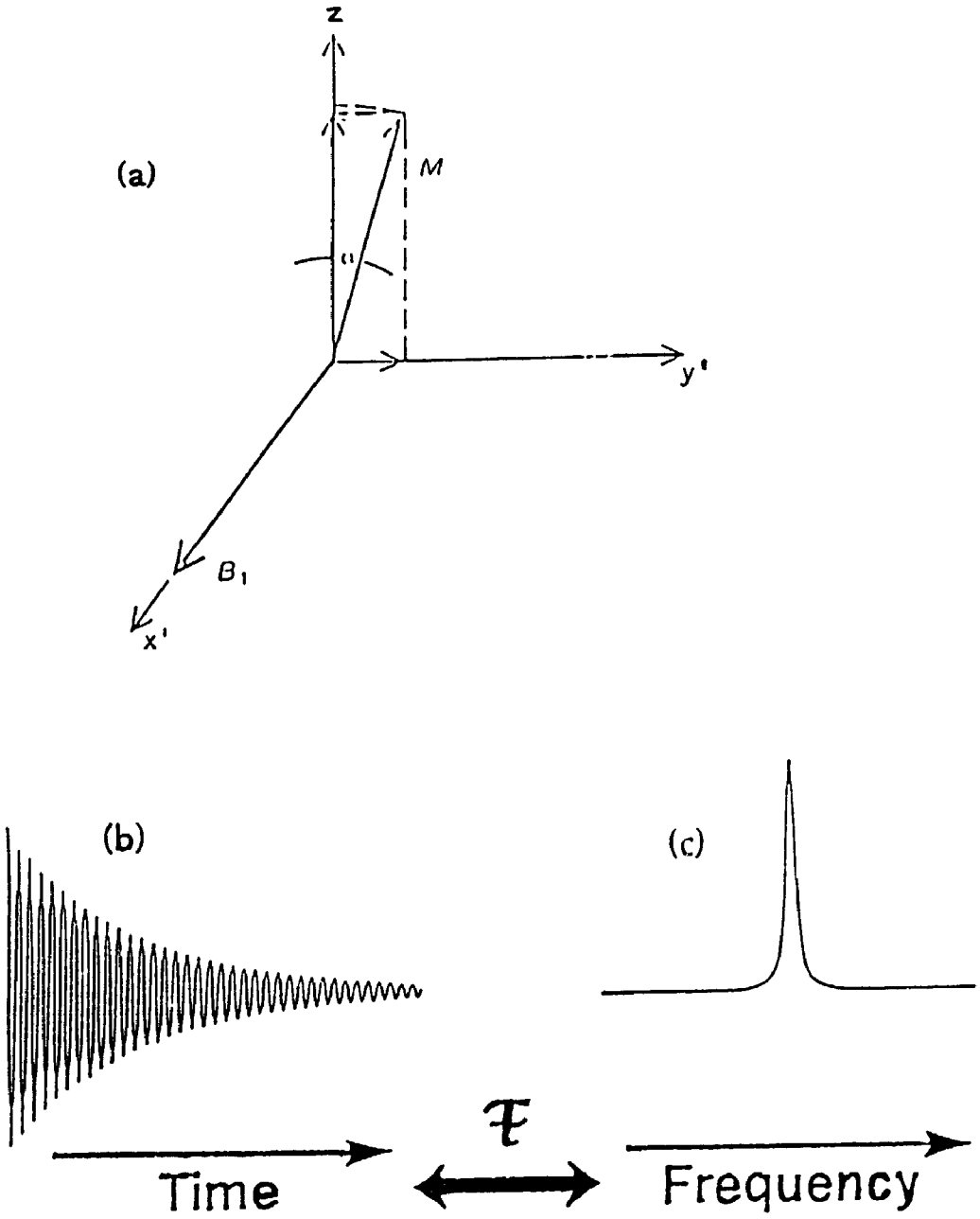

FIG. 1.1. The effects of static magnetic field and the rf excitation pulse on a sample of spin systems: (a) In the presence of a static magnetic field, the spins (magnetic dipoles) reorient themselves with a net magnetization **M** aligned parallel to the field (the z axis). The rf excitation pulse, whose magnetic field $\mathbf{B_1}$ is pointing along the x′ axis of the rotating frame, tips the vector **M** away from the z axis by an angle α, called the rf tip-angle; (b) Monoexponential decay of the time-domain NMR signal, called the free induction decay (FID), originating from the sample when the rf excitation pulse is turned off; (c) Same signal in the temporal frequency domain, obtained after Fourier transforming the signal waveform of Fig. b - the spectrum has a single peak centered at a single frequency, called the resonance frequency. Here, it is assumed that the magnetic field is uniform and that the spin system is homogeneous.

coordinate system of a frame in which $\mathbf{B_1}$ is stationary. This frame rotates about the z axis with respect to a fixed frame (x, y, z), called the laboratory frame. The rotating magnetic field is created by surrounding the sample with a coil connected to a source of radio frequency (rf) power. To tip the vector **M** (macroscopic spin vector), the frequency of the rf source must match (resonate with) the natural frequency of precession of the spin in the field $\mathbf{B_0}$, hence the term nuclear magnetic resonance.

The precessional frequency in an external static field B_0, also called Larmor frequency, is expressed by the Larmor formula

$$\omega_0 = \gamma B_0 , \qquad [1.1]$$

where γ, the gyromagnetic ratio, is a property of each nuclear species. At B_0 = 1 Tesla (10,000 gauss), the precessional frequencies for nuclei such as hydrogen (^{1}H), phosphorus (^{31}P), sodium (^{23}Na) are 42.57, 17.24, and 11.26 MHz respectively. These frequencies are in the rf band of the electromagnetic spectrum. The rf frequencies, far below those of x rays or even visible light, are not energetic enough to disrupt the molecules of living systems, thus making NMR a noninvasive scientific tool.

1.1.2 *Broadband (Non-Selective) Excitation*

The angle by which the vector **M**, initially pointing along the z axis when the sample is in equilibrium, is tipped away from the z axis toward the transverse plane is called the tip-angle, shown as α in Fig. 1.1a. The tipping of the vector **M** from the z axis into the x'-y' plane is quantum mechanically equivalent to exciting some of the spins in the sample from a lower energy state to the higher energy state. Such an excitation

can only take place when the energy of the quanta from the rf excitation source is equal to the magnetic energy difference between the two spin states. When this happpens, the spin system of the entire sample of a three dimensional volume is excited. This is called broadband or nonselective excitation of the spin system in the sense that the excitation is not confined to a particular region in the three dimensional volume of the spin system.

The experimental foundations of NMR excitation were laid by Felix Bloch (*1*) and Edward Purcell (*2*) in the 1940s, work for which they were awarded a Nobel prize in 1952. According to a classical description of NMR excitation, after the magnetization vector **M** is tipped away from the z axis and the rf excitation source (pulse) is turned off, the vector **M** returns to its equilibrium position (z axis) through free precession about the z axis. In doing so, it generates a small electromotive force that can be detected either by the same coil that transmitted the rf pulse or by a separate receiver coil. The emitted signal is called the free induction signal or free induction decay (FID), as shown in Fig. 1.1b.

The return of the vector **M** to equilibrium is characterized by two principal "relaxation" times, T_1 (the spin-lattice relaxation time or longitudinal relaxation time) and T_2 (the spin-spin relaxation time or transverse relaxation time). T_1 is characteristic of the time required for the spin system to return to thermal equilibrium with its environment (the "lattice") after the spin system has been excited (the rf pulse is turned off). T_2 is the time constant characteristic of the transverse magnetization decay to zero in an uniform field. In reality, the static magnetic field is never perfectly uniform, and, as such, the time constant defining the actual rate of signal decay in an imperfect field

is designated T_2^*. It should be noted that as the magnetization recovers along the longitudinal axis (z axis), it disappears from the transverse plane. $T_2 \leq T_1$ which is understandable, because magnetization can never recover completely without disappearing from the transverse plane.

1.1.3 *Selective Excitation (One Dimensional)*

The Fourier transform of the time-domain FID signal (see Fig. 1.1b) will be a single peak (assuming the presence of a single chemical entity in the sample only), as shown in Fig. 1.1c, centered at a single frequency, called the resonance (or Larmor) frequency. This means that the NMR signal, even though it has originated from the entire sample, has no spatial information in it since all the nuclei in the sample contributing to the FID signal are precessing at the same frequency (assuming that the static field is uniform). In order that the signal provides spatial information along a preferred direction, a frequency distribution of spins in that direction must be intentionally created. This frequency encoding of space is achieved by a magnetic field gradient, applied in the presence of a static magnetic field. Now I introduce the concept of frequency encoding and the associated selective excitation, that is, how to selectively excite (localize) only a narrow band of spins at a desired location (ROI) in a three dimensional volume, as this is key to the understanding of the more advanced class of selective excitation, later described in this thesis.

If a linear magnetic field gradient, G_x, is applied along the x direction, as shown in Fig. 1.2a, this means a linear increase of the magnetic field along the x coordinate in

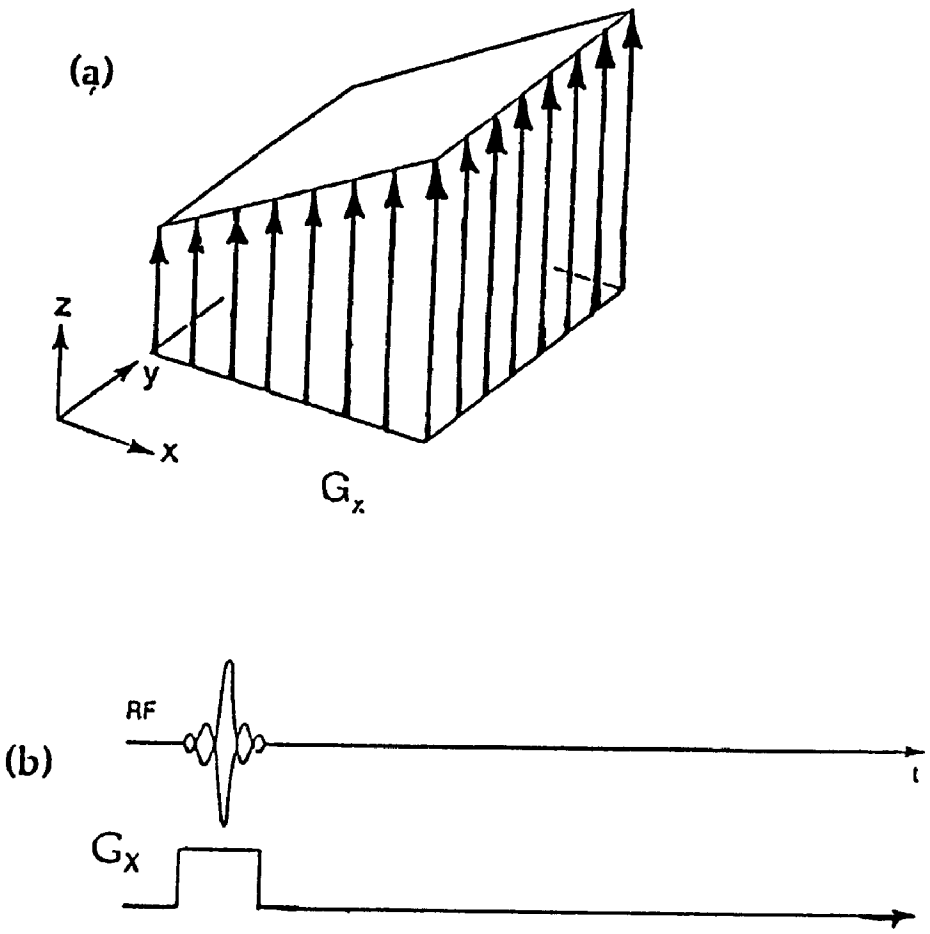

FIG. 1.2. Magnetic field gradient and its use in conjunction with a rf excitation pulse to select a slice (1D localization): (a) A linear magnetic field gradient G_x applied along x axis. Each vector in the diagram represents the magnitude of the static magnetic field acting at a particular site defined by x, y coordinates; (b) A sinc rf pulse in conjunction with G_x excites only a plane of spins orthogonal to the x axis, *i.e.*, no spins are excited from the regions outside the selected slice.

the sample. Each vector in Fig. 1.2a designates the magnitude of the static magnetic field acting at a particular point defined by the coordinates x and y. Since the Larmor frequency is proportional to the magnetic field (see Eq. [1.1]), the spins along the x direction now have a frequency distribution. In other words, using a gradient, we have encoded positional space as a function of frequency. The y and the z directions are the lines of isochromats (spins of same frequency), since spins along those directions are precessing at the same Larmor frequency. If we want to select (excite) a y-z plane (slice) of isochromats of thickness Δx, this can be achieved by using a frequency-selective rf pulse in conjunction with the gradient G_x, as shown in Fig. 1.2b. The frequency bandwidth $\Delta\nu$ of the excitation pulse should be such that

$$\Delta\nu = (\gamma/2\pi)\, G_x\, \Delta x. \qquad [1.2]$$

If the spectrometer frequency is at the resonance determined solely by B_o, the isolated slice of thickness Δx will be centered at the origin. By appropriately offsetting the spectrometer frequency with respect to resonance, such a slice of spins can be excited anywhere along the x axis. The same argument will apply if a slice were to be selected along y or z axis using G_y or G_z gradient respectively. The selection of an oblique slice involves, in general, all three orthogonal gradients via the resultant gradient vector

$$G = i\, G_x + j\, G_y + k\, G_z\,, \qquad [1.3]$$

where i, j, k are the unit vectors in x, y, and z directions, respectively. Thus, a frequency-selective rf pulse, together with a gradient, confines excitation to the nuclei in the slice, that is, no spins (signals) are excited or detected from the regions outside the defined slice.

The example presented above describes one-dimensional selective excitation (localization), and is universally used in magnetic resonance imaging (MRI) for planar (slice) imaging. The NMR signal (FID or spin echo, which is the refocussed signal of the decaying FID at some later time) of the excited slice is used to form an image in a single or multiple excitation mode. In order to acquire spatial information in the plane of the slice, two additional orthogonal gradients are further applied in the plane of the slice, once it is defined. One of the gradients encodes the position in one direction in the slice (image) plane as a function of frequency. This gradient is called the frequency-encode gradient. The other gradient, called the phase-encode gradient, encodes the position in the orthogonal direction in the image plane as a function of phase. These two together provide spatial information in the image.

1.2 *Selective Excitation (Multidimensional): A Need*

Two- and three-dimensional selective excitation has also been reported in the past, primarily for localized spectroscopy, but also for line scan and small field-of-view (FOV) imaging. Localized magnetic resonance spectroscopy (LMRS) is a new development in MR for measuring noninvasively biochemical concentrations *in vivo*. It is hoped that LMRS will provide for the early diagnosis of disease by being a means for discriminating between tissues according to their metabolic states. However, in order that the data acquired from a region of tissue be diagnostically reliable, the ROI must be accurately localized, with minimal signal contamination from the surrounding tissue volume. This requirement has led to the development of a number of selective excitation techniques in

magnetic resonance.

1.3 *Progress: Review of the Existing Selective Excitation Techniques*

In recent years, several techniques of volume-selective excitation for extracting signal from a selected volume of spins within an extended sample have appeared in the literature for various applications, primarily in LMRS, but also in MRI. These techniques can be broadly classified into two groups: techniques which achieve spatial localization by selectively exciting the spins within the region of interest (ROI) and those which saturate (suppress) all the magnetization of the region outside the ROI, whose magnetization is left untouched during the localization procedure.

1.3.1 *Methods That Localize by Exciting Only the ROI*

The techniques of this class have been introduced under a variety of acronyms, including DRESS (*3*), VSE (*4*), SPARS (*5*), ISIS (*6*), VEST (*7*) and STEAM (*8*). All these use selective, large-tip-angle rf pulses (typically of 90° or 180°), and linear static field gradients in one, or at the most, three orthogonal directions to selectively excite the ROI.

The DRESS (Depth-REsolved Surface-Coil Spectroscopy) sequence requires only a single, selective, 90° excitation pulse to be transmitted through a conventional volume rf coil or a large surface coil for providing a uniform rf excitation field over the sensitive volume, as shown in Fig. 1.3a. To restrict the field of signal reception/detection, a smaller diameter surface coil is used. The combination of the excitation pulse and the

FIG. 1.3. Some basic pulse sequences for localizing a single volume: (a) A DRESS pulse sequence - a 90° sinc pulse in combination with a gradient G_y directed co-axial to the coil excites a plane (slice) of spins parallel to the surface coil. NMR signal is acquired slightly before or as soon as the slice is refocussed by the negative lobe of G_y; (b) A VSE pulse sequence - a set of 45° selective, a 90° broadband, and a 45° selective RF pulses, all applied along the same axis (x' axis), in the presence of G_x, G_y, and G_z selects a volume element (intersection of three orthogonal planes) of negative z magnetization which is then observed with a broadband RF pulse; (c) A SPARS pulse sequence - the combination of three consecutive pulse trains for x, y, and z gradient directions selects a 3D ROI with preserved z magnetization, while the magnetization outside the ROI is dephased by the gradients. A non-selective, 90° RF pu[illegible] then interrogates the ROI magnetization to acquire data. Figures 1.3a, b, and c are photocopied from the *Journal of Magnetic Resonance* by the permission of the copyright holder, the Academic Press, Inc.

(a)

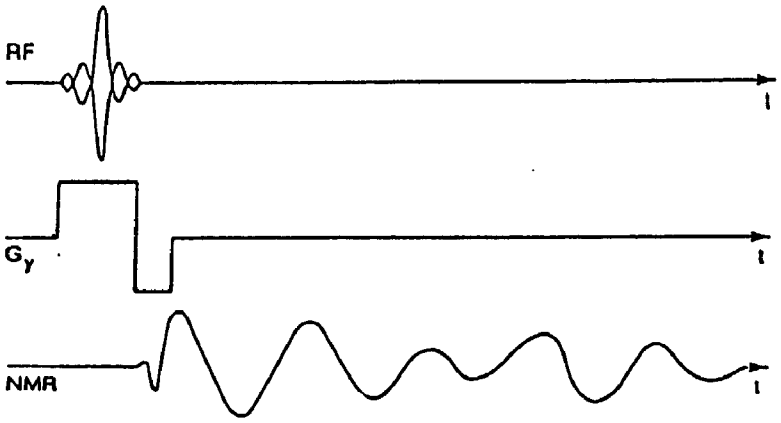
RF
t
G_y
t
NMR
t

(b)

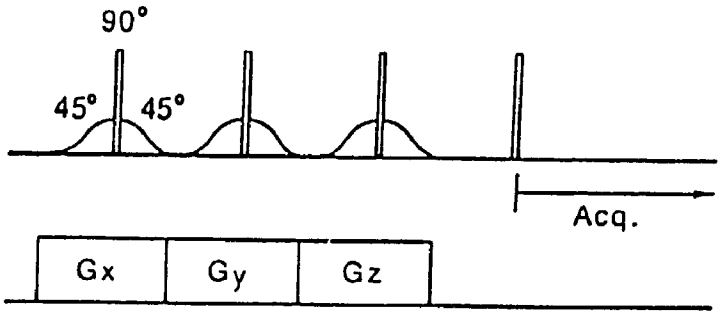
90°
45°
45°
Acq.
Gx
Gy
Gz

(c)

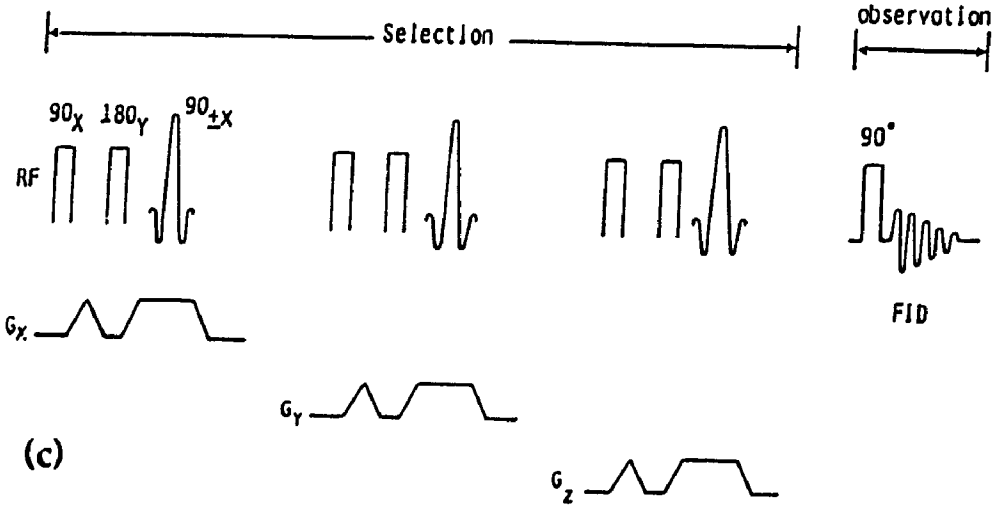
Selection
observation
90_X
180_Y
$90_{\pm X}$
RF
90°
FID
G_X
G_Y
G_Z

linear magnetic field gradient, whose direction is co-axial with the surface coil, excites a flat plane of nuclei parallel to the plane of the surface coil. The extent of the sensitive volume within the selected plane is determined only by the diameter of the surface detection coil and the distance of the coil from the sensitive plane. Because of the broad sensitivity profile of the surface detection coil, localization by DRESS in two of the dimensions (orthogonal to the slice selection direction) is relatively poor, uncontrolled, and depth-dependent.

The alternative VSE (Volume-Selective Excitation) sequence does provide gradient-controlled localization in all three dimensions. As shown in Fig. 1.3b, this method uses a $45°_{selective}(i)$ - 90° - $45°_{selective}(i)$ pulse sandwich in three orthogonal directions, where the index i = x, y, and z. The SPARS (SPAtially Resolved Spectroscopy), a derivative of VSE, uses the $90°(x)$ - $180°(y)$ - $90°_{selective}(i)$ pulse sequence of Fig. 1.3c. In VSE, as well as SPARS, the ROI is defined by the intersection of the orthogonal slices. The signal from the partial excitation of the non-intersection region is forced by the gradients to dephase in the transverse plane. The ROI signal is observed by a nonselective 90° readout pulse. These sequences are simple to implement and almost insusceptible to the rf tip-angle errors (deviations from the exact 90° tip-angle). However, these methods suffer from the loss of spatial discrimination due to T_1 relaxation that occurs in the time interval between the preparation of the localized ROI (volume) and the readout of the signal. For this reason, it is often necessary to use phase-alternated (cycled), selective excitation pulses in VSE and SPARS in combination with a data add/subtract cycle. Such a scheme is intended to subtract out all the spurious

signal from outside the ROI and add up the signal from the selected ROI. However, the methods suffer from subtraction errors, and lengthy tuning procedures.

VEST (Volume Excitation using STimulated echoes), as well as STEAM (STimulated Echo Acquisition Mode) employ the $90^{o}_{selective}(x)$-$90^{o}_{selective}(y)$-$90^{o}_{selective}(z)$ pulse sequence to localize a 3D ROI, and acquire the ensuing stimulated echo from the localized ROI. One of the problems associated with these sequences is that they give rise to a number of unwanted FIDs and echoes, which ought to be suppressed completely. Partial suppression is achieved by spoiler gradients (magnetic field gradients, which are used to "spoil" or dephase the transverse magnetization); however, for better suppression, these methods again require a lengthy phase-cycling and data add/subtract procedure.

The techniques described above use a number of rf pulses and static magnetic field gradients to achieve (1D, 2D or 3D) ROI localization. New techniques (*9-13*), recently developed, employ a single, tailored rf excitation pulse in combination with time varying oscillating gradients to achieve 2D selective excitation in a single shot. Localization by these techniques is fast (total localization time ~ 10 ms). However, they suffer from the problems of achieving accurate single on- or off-center localization leading to significant signal contamination of the ROI signal from outside. Also, these techniques may have problems in isolating multiple ROIs simultaneously. The major disadvantage of all of these techniques (*3-13*) except ISIS is that they perturb the magnetization of the ROI during localization in such a way that some attenuation of the ROI signal occurs prior to acquiring data. For this reason, each suffers from, at least,

the limitation of transverse magnetization decay. Since the transverse magnetization decays with a characteristic time T_2 or T_2^*, the signal from short T_2 (few ms, *e.g.*, 10 ms as for ^{31}P) species decays very fast, which causes a lower signal-to-noise (S/N) ratio in the ROI signal from such species. In literature, this decay problem has also been referred to as the T_2 or T_2^* decay problem.

Transverse magnetization decay during localization does not occur in the case of the ISIS method, because it uses all of the selective inversion pulses in combination with an add/subtract data-cycle. However, it suffers from subtraction errors and dynamic range limitations (large difference between the two signals, one strong originating from the large outer region, and other weak from the small ROI, may limit (saturate) the analog-to-digital converter range or scale down the ROI signal in an absolute scaling). These problems lead to a decreased S/N ratio in the final ROI signal. Both limitations have been minimized in OSIRIS (*14*), a modified form of ISIS that uses noise-modulated, selective rf pulses in the outer region to suppress the signal from the outside volume. However, both the ISIS and OSIRIS techniques involve a lengthy tuning procedure due to the requirement of several signal acquisitions (conventionally eight) and multiple inversion pulses to achieve final localization.

The techniques (*3-14*) described above are either hardware-demanding or lengthy. More importantly, they are less suitable for short T_2 species. A localization method is desirable, which is not only single-shot, but also T_2 independent.

1.3.2 *Methods That Intend to Render M = 0 outside the ROIs*

The localization techniques (second group) (*15-22*) which isolate the ROI by saturating the magnetization of the outer volume, while leaving the ROI unperturbed, are particularly attractive: they avoid the T_2 or T_2^* decay problem of selective excitation techniques(*3,5,7-13*), as mentioned previously. They have appeared in the literature under different acronyms with DIGGER (*15*) and LOCUS (*20*) as the pioneer techniques. In this approach, during the preparation period, the magnetization of the ROI is left aligned along the longitudinal axis, while the magnetization outside the ROI is tipped into the transverse plane and dephased by a static magnetic-field gradient. The magnetization of the ROI is then interrogated with an excitation pulse ("read pulse") to acquire data.

These presaturation techniques use successive applications of selective, large-tip-angle rf pulses (typically 90° or greater) and linear, static field gradients in one or more orthogonal directions. For example, Haase's LOCUS technique (*20*) uses a set of twelve frequency-offset rf sinc pulses, each pulse of tip-angle 90°, in three orthogonal directions (four pulses in each direction) to saturate the region outside a cuboidal volume. The tailored saturation technique of Garroway (*22*) first selects a plane (1D localization) by saturating the magnetization on either side of the plane and then selects a line (2D localization) by selecting a slice orthogonal to the plane (intersection of two planes is a line). The SMILE technique (*16*) uses SWIFT pulses (*17*) of uniform frequency spectrum to uniformly excite and presaturate the region outside the ROI more accurately.

Since each of these methods for localizing a ROI employs large-tip-angle (90°) pulses in only three orthogonal directions, each is prone to error for the following

reasons. The degree of suppression of the signal from the outer volume depends largely upon the accuracy of the tip-angle of the rf saturation pulses. Small errors in the tip-angle, which are likely to occur because of mistuned rf pulses and spatial inhomogeneities in the rf transmit field, result in incomplete suppression of the outer volume signal. Since the outer volume is usually much larger than the ROI, the unwanted signal from it may be much larger than that from the ROI. Also, the requirement for good rf homogeneity rules out the implementation of these methods using surface coils. Other problems associated with the large-tip-angle rf pulses used in these techniques are the consequences of imperfect slice-selection rf profiles: spins near the edge of the sample are not fully saturated while some magnetization is excited within the ROI. Thus, the ROI boundary is poorly defined.

Several methods have been proposed to deal with these inaccuracies in localization. Crawley (*23*) has attempted to modify the LOCUS technique by using two additional oblique angled saturations in order to improve the outer volume saturation; however, problems such as the requirement for good rf field homogeneity, tip-angle errors and the imperfections in slice-selection profiles persist because of the use of large-tip-angle (90°) rf sinc pulses applied in only a few directions.

Tip-angle error limitations do not arise in Hinshaw's sensitive point (*24*) or line scan (*25*) methods, both of which use a continuous string of phase alternated, hard, 90° tip-angle pulses in the presence of a rotating gradient for multiple excitations and dephasings of spins outside a gradient-defined "null-region" (ROI), a point (voxel) or a line (cylinder). However, in addition to requiring a lengthy procedure of signal

averaging, these techniques seem to be somewhat less suitable for off-center and multiple ROIs localization on whole-body imaging systems in which the gradient null-plane is always at the center, unless special gradient hardware is used to move the null-plane off-center.

Sauter (*26*) has used repeated applications of sinc pulses of varying tip-angles, in combination with a surface coil operating in transmit/receive mode, to saturate more completely a single slice off-center from the ROI. However, the saturation period (140 ms to saturate one slice) is so long that significant recovery of the longitudinal magnetization of the outer volume would occur if two- or three-dimensional outer volume presaturation were attempted.

1.4 *A New Solution to the Problem of Accurate ROI Localization*

To overcome the above-mentioned problems, I have devised a new single-shot method called Projection Presaturation (*27-33*) for multi-dimensional spatial localization by accurate outer volume suppression. The method uses a series of short, selective, small-tip-angle ($\sim 30^{o}$) saturation rf pulses, applied in the presence of a rotating gradient of constant amplitude, to saturate the region outside the ROIs, whose magnetization is ideally unperturbed during localization. The theoretical and the experimental details of the method will be presented in the subsequent chapters of this thesis.

1.4.1 *Advantages of Projection Presaturation Method*

There are several advantages of using Projection Presaturation. Since, the tip-

angle of the rf pulses is small, the saturation profile of these rf pulses is close to the desired (a rectangular profile), as predicted by the linear approximation Fourier transform method. So the consequences of imperfect slice-selection profiles, as mentioned previously, are automatically reduced.

The technique does not suffer from the tip-angle errors, which cause signal contamination from outside. Since the rf pulses are repeated an appropriate number of times until all the longitudinal magnetization of the outer volume is tipped into the transverse plane and dephased by the rotating gradient, the accuracy of outer signal suppression is ensured.

For the same reason, because it does not require high rf homogeneity, it can also be implemented using surface coils.

The technique does not require any special gradient hardware. Because a rotating gradient can be formed by vectorially summing two identical sinusoidal gradients with a 90° phase-shift between them (*e.g.*, cosinusoidal x and sinusoidal y gradients), the method can be implemented on any currently used commercial scanner.

Because the technique is robust and versatile, it has many applications in MRI, LMRS, as well as other areas of MR.

1.5 *Organization of This Thesis*

This thesis outlines the theory and experimental verification of Projection Presaturation. First, an analytical method based on the small-tip-angle approximation is presented in chapter 2 to design rf pulses to localize a single, centered, cylindrical ROI

(*27-30*). Parameters affecting the quality of outer volume suppression, such as number and spacing of rf pulses and interpulse gradient strength, are experimentally optimized. The efficacy of this new localization technique is demonstrated using phantoms and laboratory animals. Experimental results are obtained to support the theory. Next, in chapter 3, the method is generalized and extended to isolate one or more ROIs simultaneously, whose shape and size can be tailored to match *in vivo* targets at arbitrary positions, thus permitting imaging, spectroscopic or relaxometric studies to be performed on such targets under identical physiological conditions (*31-33*). Finally, some applications of the technique to imaging and localized spectroscopy (*35*) are demonstrated in chapter 4 (the contents of chapters 2, 3, and part of 4 have already been published in the **J. Magn. Reson.**) and to relaxometry (*34*) in the Appendix (a paper on the contents of the Appendix has been submitted to the **Magn. Reson. Med.**) before the success of spatial localization by Projection Presaturation is examined in chapter 5.

CHAPTER 2

Localization of a Single, Centered, Cylindrical ROI

2.1 *Introduction*

In this chapter, the basic framework of the Projection Presaturation localization method is laid down. The underlying principle of the method for achieving accurate volume localization is elucidated with theory followed by experimental verification.

The method uses a series of rf pulses in the presence of a stepwise rotating gradient to saturate only the region outside the ROI(s). As the rotating gradient vector sweeps a circle about an axis of rotation in a number of discrete steps, the rf pulse is applied at each gradient step. As a simple illustration, Fig. 2.0 shows the schematic of an ideal case of the saturation of the outer region as a result of rf excitations at three gradient steps (angles). Overlap of the hatching represents the degree of saturation: the darker the shading, the greater the degree of saturation. As the number of gradient angles is increased, the outer region is more and more saturated, thus, defining the ROI (unsaturated region) more clearly. In the subsequent sections, I will describe the physical basis of this phenomenon, using a vector model of magnetization, and demonstrate, theoretically and experimentally, the degree of saturation achieved using this approach.

2.2 *Principle and Measure of Outer Volume Suppression*

The concept of the Projection Presaturation method is based on the small-tip-angle

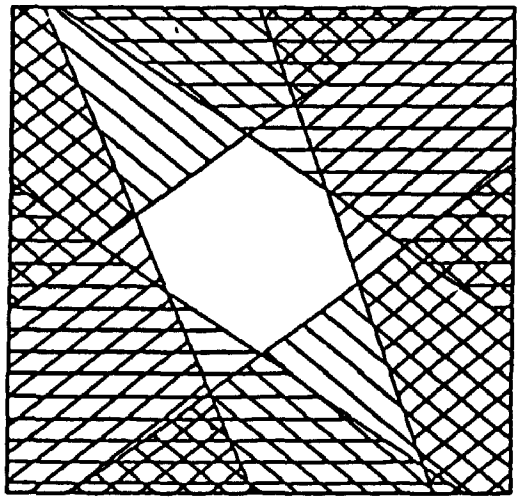

Fig. 2.0 A schematic diagram showing the process of saturation of the outer region by Projection Presaturation: Hatching represents the partial saturation produced by the rf pulses and the rotating gradient in a simple three gradient-steps (angles/directions) case. Parallel lines in a given direction may be thought of as the lines of isochromats (spins precessing at the same frequency) or the spin density of the outer region projected onto the gradient direction. Overlap of the lines represents the number of excitations "seen" by the particular regions, and, hence, the degree of saturation produced: the darker the shading, the greater the degree of saturation. As the number of gradient steps (directions of the set of parallel lines) is increased, while the rotating gradient vector sweeps a circle about an axis of rotation (orthogonal to the plane of the page, in this case), the outer region is more and more saturated, thus, defining the ROI (unexcited/unsaturated region) more clearly. This is essentially the presaturation of the projection of the outer region (hence, the name "Projection Presaturation") and in that sense this technique is conceptually analogous to the method of Back-Projection (*11*) of the CT image reconstruction.

approximation. The small-tip-angle approximation for selective excitation assumes both that the initial magnetization vector is aligned along the +z direction and that the effect of the rf excitation pulse is small, with the result that the z-magnetization is tipped away from the z axis toward the transverse plane by only a small angle ($\leq 30^{o}$), hence the name, small-tip-angle approximation. Under this approximation the solutions of the Bloch equations are linear, as shown by Hoult (*36*), with the result that the rf excitation profile is the Fourier transform of the rf excitation pulse itself.

In the Projection Presaturation sequence, each rf pulse or set of rf sub-pulses applied at a given rotation angle of the gradient tips the z-magnetization of the region outside the null region (ROI) by a small angle θ into the transverse plane, while the spoiler gradient pulse following the rf application destroys the phase coherence of the transverse magnetization so generated. Let us suppose that the total, equilibrium magnetization vector of the region outside the ROI(s) is of magnitude M_o, pointing initially along the +z axis of the rotating frame, as shown in Fig. 2.1a. After the first selective rf pulse in the series, applied along the x′ axis of the rotating frame (see Fig. 2.1a) in order to excite only the outer region, the resultant magnetization vector of the outer region will have as the longitudinal and the transverse components

$$M_z^{(1)}(\theta) = M_o \cos\theta\,, \qquad [2.1a]$$

$$M_{y'}^{(1)}(\theta) = M_o \sin\theta\,, \qquad [2.1b]$$

$$M_{x'}^{(1)}(\theta) = 0. \qquad [2.1c]$$

It is required that the spoiler gradient pulse applied after the rf excitation pulse randomize the spin population phase throughout the transverse plane in order that the net NMR

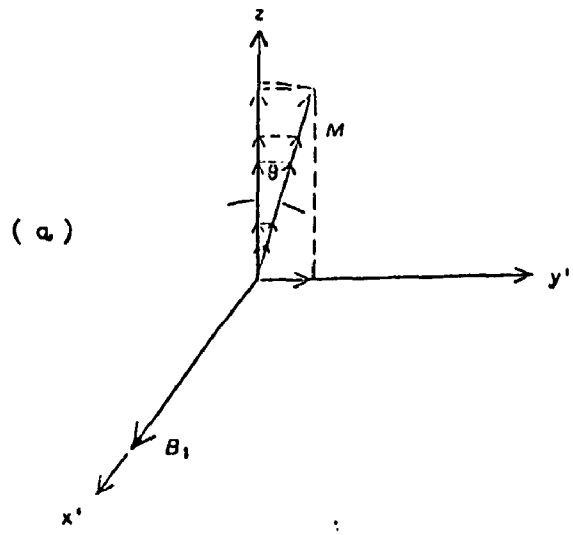

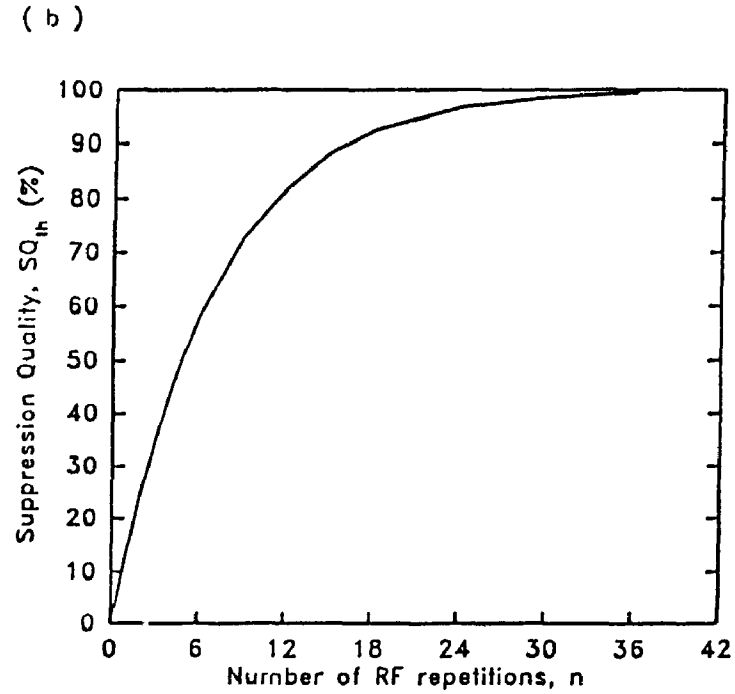

FIG. 2.1. Measure of outer volume suppression by Projection Presaturation: (a) The equilibrium magnetization vector $\mathbf{M}_0$ of the outer region pointing initially along the +z axis is tipped away from the +z axis into the transverse plane by a rf pulse of tip-angle θ. The transverse component of the tipped vector is forced to dephase by the gradient in the projection presaturation sequence; the longitudinal component of it becomes the initial magnetization for the next rf pulse in the series. The process of successive rf tipping, each followed by gradient dephasing, causes the equilibrium magnetization of the outer region to reduce. (b) the fractional "spoiled" magnetization of the outer region, called the theoretical suppression quality, SQ_{th}, versus number of repetitions, n, of the rf pulse of tip-angle 30°: the SQ_{th} increases monotonically with n.

signal after the gradient pulse be zero, i.e.,

$$\int_0^r [\gamma/2\pi \int_0^{T_g} G_r^{spoil}(t) r_i dt] dr_i = 0 \qquad [2.2]$$

The bracketted integral quantifies the phase variation imposed by the gradient pulse of amplitude $G_r^{spoil}(t)$ and duration T_g pointing along r direction on an i^{th} isochromat of spins located at distance r_i from the center. The outer integral sums these spin phase variations over the extent (r) of the object so that the net phase of all the spins in the transverse plane is zero. Assuming that the condition [2.2] is met by the appropriate choice of $G_r^{spoil}(t)$ of duration T_g, the spins forming the transverse components, given by Eqs. [2.1b] and [2.1c], fan out in the x'y' plane to yield an average transverse magnetization of zero. Thus, after each rf application, the resultant magnetization vector is still aligned along the +z axis but has a smaller magnitude $M_o \cos \theta$, and it becomes, in turn, the initial magnetization state for the next rf application in the sequence. Therefore, when the next small-tip rf pulse is applied along the same axis, the small-tip-angle approximation is valid, and further small-tip excitation and dephasing processes are carried out until the outer volume magnetization is adequately suppressed.

After n excitations and dephasings have occurred, the residual longitudinal magnetization outside the null region (ROI) will be equal to $M_o [\cos \theta]^n$. Therefore, the fractional longitudinal magnetization "spoiled", called the theoretical suppression quality, SQ_{th}, can be expressed as

$$SQ_{th} = 1 - [\cos \theta]^n. \qquad [2.3]$$

Equation [2.3] estimates theoretically the suppression quality for a given rf tip-angle θ

and the number of rf excitations n. It is shown in Fig. 2.1b that SQ_{th} increases monotonically with n. For a typical value of $\theta = 30^{\circ}$, n = 36, the $SQ_{th} = 99.43\%$, a suppression which should be adequate for most of the applications of this method to MR, *e.g.*, imaging. If needed (as for spectroscopy), a higher SQ_{th} can be achieved by appropriately choosing n and θ, including $\theta > 30^{\circ}$, the limit of the small-tip-angle linear regime. The consequences of the use of large-tip-angle ($\theta > 30^{\circ}$) rf pulses, and the steps to be taken to minimize the effects thereof on the excitation profile, will be discussed in the subsequent chapters in this thesis.

In arriving at Eq. [2.3], because it is assumed that the total time to achieve a given SQ_{th} is insignificant as compared to the T_1 of the outer volume species, any recovery of the longitudinal magnetization of the outer volume during this time (localization time) is thereby assumed negligible. In most cases, this assumption can be justified by making an appropriate choice of n and θ (which might include $n < 36$ and $\theta > 30^{\circ}$), while achieving adequate SQ_{th}, as estimated by Eq. [2.3].

Equation [2.3] further assumes that every spot in the outer region has "seen" all the n excitations. This is true for 1D localization, and, hence, Eq. [2.3] accurately estimates the suppression quality of the outer volume magnetization for 1D localization. However, for multidimensional spatial localization, Eq. [2.3] still remains a close approximation for SQ_{th}, as described below. For 2D localization, as the gradient vector rotates stepwise by one complete cycle about some axis with each gradient step followed by an rf application, the rf excitation profile, which includes null region(s), also rotate(s) with the gradient. As a result, some locations in the outer region (depending upon the

angular step size of the rotating gradient, width of the null region, etc.), will "see" fewer excitations, and hence exhibit slightly lower suppression quality than those which "see" all n excitations. In such cases, the overall SQ_{th} will be somewhat lower than estimated by Eq. [2.3]. However, for optimal values of n and θ chosen to achieve adequate suppression quality, this average SQ_{th} will not be significantly different from the one estimated by Eq. [2.3], as can be seen below.

For some idea of this average SQ_{th}, let us suppose that some locations in the outer region experience fewer, say, 32 excitations from a total of $n = 36$, $\theta = 30^{o}$. The SQ_{th} of such locations will be 98.99%, as compared to the SQ_{th} = 99.43% of the spots which have seen all ($n = 36$) excitations. Thus, the estimated overall SQ_{th} of the entire outer region will lie between 98.99% and 99.43%, and will not be significantly different from 99.43%, as estimated by Eq. [2.3]. Hence, for practical purposes, Eq. [2.3] still should hold to estimate the SQ_{th} even for 2D localization, and serve as a guide to set up the experiments in order to achieve adequate suppression. For the case of multiple ROIs, however, there will be some spots which may "see" far fewer excitations, and, thus, exhibit poor SQ_{th} as estimated by Eq. [2.3]. However, to achieve adequate SQ_{th}, Eq. [2.3] can again be used to find the appropriate θ of the pulse(s) exciting such spots, once the actual n for such spots is known. More details on this will be given in chapter 3.

2.3 *Organization*

The formalism of this method is restricted in this chapter to isolating a single, centered, cylindrical ROI (*27,28,30*). First, an analytical method is presented in section

2.4 to design the saturation rf pulse shape which, in a rotating gradient scheme, can be applied to saturate the outer volume, thus isolating a ROI. For practical purposes, the terms like suppression quality (SQ_{expt}) and the "ROI" are defined in section 2.5. In section 2.6, an experimental set-up to implement the Projection Presaturation localization sequence for isolating the ROI is described. The accuracy of the localization sequence is then tested experimentally on phantom and laboratory animals and the results are presented in section 2.7. Section 2.8 is devoted to discussions and conclusions.

2.4 *Designing saturation rf pulses*

In order to isolate a ROI by suppressing the outer-volume signal, the saturation rf pulse shape has to be tailored in such a way that it excites only the outer region. An ideal excitation profile is shown in Fig. 2.2. For a small-tip-angle, the shape of the saturation rf pulse can be determined by taking the inverse Fourier transform (analytically or numerically) of the desired response-profile in one dimension (*36*). For convenience, the performance of this technique is demonstrated by analytically transforming the profile. The analytical rf field, $B_1(t)$, corresponding to the response of Fig. 2.2, can be obtained by the following Fourier transform relation:

$$B_1(t) = \int_{-(\nu_1+\nu_2)}^{(\nu_1+\nu_2)} M_\perp(\Delta\nu)\, \exp(i2\pi\Delta\nu t)\, d(\Delta\nu) \qquad [2.4]$$

where $M_\perp$ is the magnitude of the transverse magnetization and $\Delta\nu$ is the frequency offset of the B_1 field. After performing the integration for the desired $M_\perp(\Delta\nu)$ of Figure

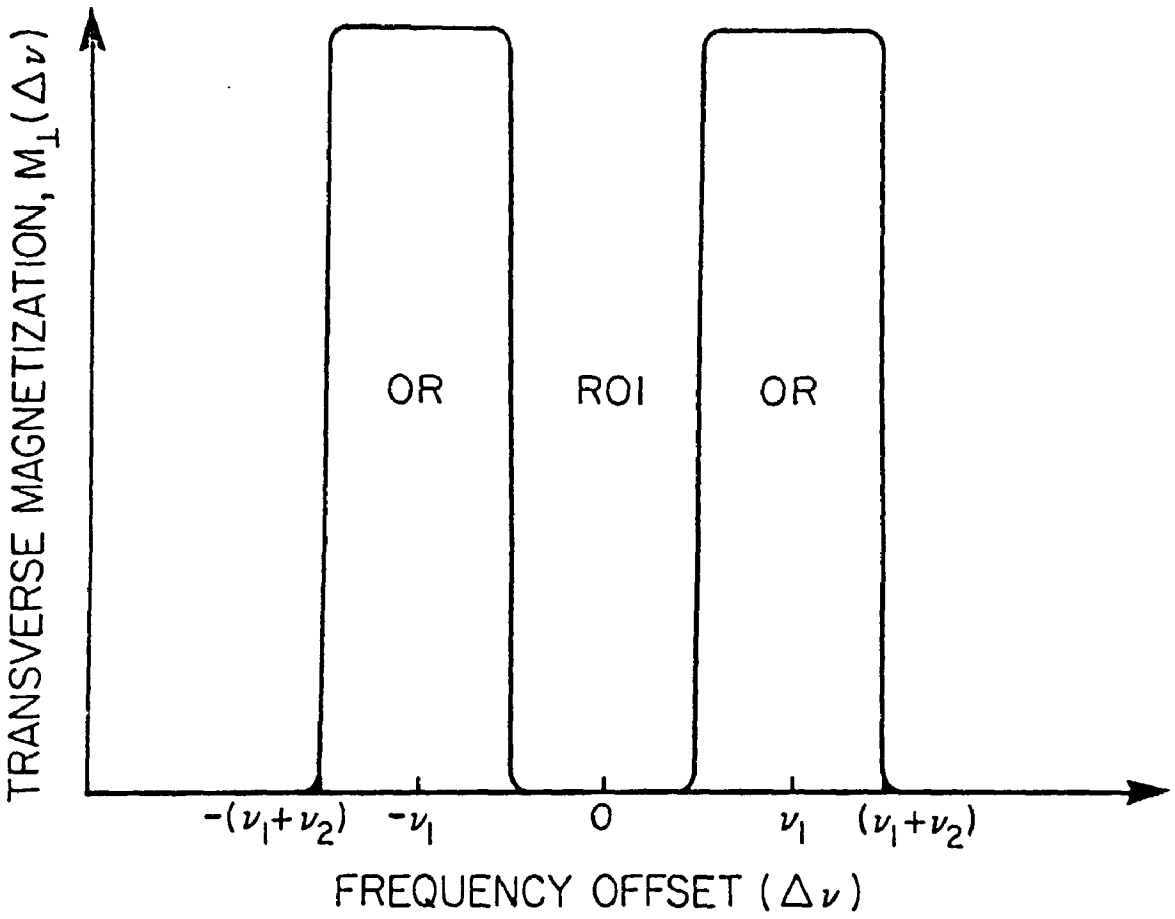

FIG. 2.2. Ideal one-dimensional response of a single selective saturation rf pulse: the pulse excites only the outer region. Repeated application of the pulse, in combination with a constant amplitude rotating gradient, excites the corresponding volume of revolution, leading to presaturation of a hollow cylinder (the outer region (OR)) about an unperturbed axial cylinder (the region of interest (ROI)).

2.2 and rearranging the terms, the rf field can be expressed as:

$$B_1(t) \propto \text{sinc}(2\pi\nu_2 t)\,[\exp(i2\pi\nu_1 t) + \exp(-i2\pi\nu_1 t)] \quad [2.5a]$$
$$= C\,\text{sinc}(2\pi\nu_2 t)\cos(2\pi\nu_1 t) \quad [2.5b]$$

where C scales the rf tip-angle. The shape of the rf field is a pair of frequency offset sinc functions (see Eq. [2.5a]) or equivalently an amplitude modulated sinc function (see Eq. [2.5b]). In this chapter, Eq. [2.5b] will be taken as the rf pulse shape for localizing a single, centered, cylindrical ROI; however, the choice of Eq. [2.5a] as the rf pulse shape could equally have been made.

The frequency ν_1 in Eq. [2.5] determines the width of the ROI (the notch region) of Fig. 2.2 for a given ν_2, since the diameter of the ROI increases as ν_1 increases. The frequency ν_2 (for a given ν_1) and hence the width of the central lobe of the sinc function determines the diameter of the outer region to be excited and ultimately saturated. The frequencies ν_1 and ν_2 of Eq. [2.5] can be expressed in terms of the diameter of the ROI, d, and the diameter of the outer region, D, viz:

$$(\gamma/2\pi)\,G_r d = 2\,(\nu_1 - \nu_2) \quad [2.6a]$$
$$(\gamma/2\pi)\,G_r D = 2\,(\nu_1 + \nu_2) \quad [2.6b]$$

where γ is the gyromagnetic ratio, and G_r is the constant amplitude of the rotating gradient. Substitution of Eq. [2.6] into Eq. [2.5b] yields:

$$B_1(t) = C\,\text{sinc}(2\pi K G_r(D-d)t)\cos(2\pi K G_r(D+d)t) \quad [2.7]$$

where $K = \gamma/8\pi$. Equation [2.7] gives the analytic expression for the shape of the

saturation pulse for an arbitrary choice of D and d. Repeated application of such pulses in the presence of a constant amplitude field gradient G_r rotating about an axis isolates an ROI, which is a cylinder of diameter d extended in the z-direction whose magnetization is virtually untouched by this pulse. A "read pulse", which can be made selective along the axis of rotation, will limit the extent of the cylinder, and a disk can thus be isolated. By appropriately setting the frequency-offset of the selective "read pulse", the disk (ROI) can be selected anywhere along the axis of rotation. Alternatively, the read pulse can be broadband (non-selective) to acquire T_2-independent spectral, imaging or relaxometric data from the whole cylindrical ROI.

2.4.1 *Consequence of the rf Imperfections: Signal Loss from the ROI*

The procedure described in section 2.4 to localize a ROI ideally assumes zero sensitivity of the rf profile (see Fig. 2.2) within the ROI. However, in reality, since the rf waveform (given by Eq. [2.5] or [2.7]) is truncated in the time-domain, there are side lobes in the rf profiles which produce non-zero intensity in the ROI. Repeated application of such a pulse to localize a ROI would, therefore, cause some signal loss from the ROI. This signal loss caused by the imperfection in the rf profile can be empirically estimated as follows:

Let us suppose that for a given shape (*e.g.* cossinc or a pair of off-centered sinc waveforms) of the rf pulse of tip-angle θ, the average profile magnitude within the ROI is p% of that of the outer region. This unwanted excitation in the ROI amounts to tipping the longitudinal magnetization in the ROI by an angle of

$$\theta_{ROI} = \sin^{-1}[(p/100) \sin \theta]. \quad [2.8]$$

After n such rf excitations, the residual longitudinal magnetization within the ROI will amount to $(\cos \theta_{ROI})^n$. Therefore, the percentage signal loss from the ROI in n rf repetitions can be expressed as

$$SL_{rf} = [1 - (\cos \theta_{ROI})^n] \times 100. \quad [2.9]$$

Equation [2.9] shows that for a given θ_{ROI}, and hence given p, the SL_{rf} increases monotonically with n. Recalling from Eq. [2.3] that the SQ_{th} also increases with n, a trade-off between the SQ_{th} and SL_{rf} must, therefore, be made.

It will be straight forward to generalize Eq. [2.9] for estimating SL_{rf} when p, and thus θ_{ROI}, is different at different angles of gradient rotation. This will happen when we attempt to localize off-centered ROI(s) or a centered, cylindrical ROI of non-circular cross-section, as will be seen in the next chapter. In that case, after n excitations, the residual longitudinal magnetization within the ROI will amount to $\Pi_{i=1,n} \cos \theta_{ROI}^{(i)}$. The signal loss can then be expressed as

$$SL_{rf} = [1 - \Pi_{i=1,n} \cos \theta_{ROI}^{(i)}] \times 100 \quad [2.10]$$

Equations [2.8 - 2.10] show that the undesirable loss of signal from the ROI can be reduced by reducing θ_{ROI}, which, in turn, can be reduced by making p small. In reality, however, p can never be zero, and thus some signal loss from the ROI is inevitable.

Apart from the rf imperfections, there are some other sources of signal loss from the ROI; however, these along with the application of Eqs. [2.8] - [2.10] will be treated in more detail in the next chapter.

2.5 *Some Definitions*

2.5.1 *The ROI*

The ideal one-dimensional saturation profile shown in Fig. 2.2, will always in reality exhibit finite transition zones between the region of maximum excitation and the region of minimum excitation, *i.e.*, the edges of the ROI will not be perfectly sharp. If the ROI is defined so as to enclose entirely the transition zones, then signal contamination from the outer region will be minimized at the expense of a lower S/N ratio from the ROI. On the other hand, if the transition zones are taken to lie entirely outside the ROI boundary then the S/N ratio from the ROI will be enhanced, but signal contamination from the outer volume will ensue. Even though the transition regions in the profile of a small-tip-angle saturation rf pulse are narrow, resulting in a ROI of sharp boundary, as will be shown later in this chapter, I compromised by defining the ROI diameter to be the full-width at 10% of the maximum (FWTM) of the image intensity profile along any diameter of the cylinder after presaturating the outer volume.

2.5.2 *Suppression Quality*

In order to measure experimentally the degree of suppression of the outer volume, I define the signal suppression quality parameter SQ_{expt} as follows:

$$SQ_{expt} \equiv \frac{I^S - I^L}{I^S} \qquad [2.11]$$

where I^S and I^L are the average pixel intensities of the outer region in the object, in the standard (normal) and localized magnitude image, respectively (with average "noise"

subtracted out from either intensity). For practical purposes, the average "noise" was taken as the estimated average pixel intensity of the region corresponding to air in the magnitude image.

Lawry (*37*) has used the total absolute signal from the entire outer volume (*i.e.* the total contaminant signal), instead of I^L, as a measure of localization quality. The absolute signal contamination, ASC, expressed as a ratio of the integral of absolute signal from the whole outer volume to that from the ROI in the localized image can be written as,

$$ASC = [I^L N]/[I^{ROI} n] , \qquad [2.12]$$

where I^{ROI} is the average absolute pixel intensity in the ROI in the localized magnitude image, and N and n are the total number of voxels, in the outer region and the ROI, respectively. By noting that N and n are proportional to the volumes of the respective regions, the absolute signal contamination can be finally expressed as,

$$ASC = [1 - SQ_{expt}] [(L/l) (D/d)^2 - 1]I^S/I^{ROI}, \qquad [2.13]$$

where the fact that the length l of the ROI will not necessarily be equal to the length L of the outer volume has been used. It is noted that the absolute signal contamination given by Eq. [2.13] is a size dependent parameter, not a global parameter as is SQ_{expt}. This can be seen as follows: For a particular case of D:d = 2:1, L:l = 1:1 and SQ_{expt} = 99.9%, the ASC using Eq. [2.13] is 0.3%. For the same SQ_{expt} but for a typical volume ratio of 99:1, *i.e.* D:d = 10:1 and L:l = 1:1, the ASC is now 10%. In making the above estimations, it has been assumed that $I^S = I^{ROI}$, i.e., signal loss from the ROI has been ignored. Thus ASC is size dependent. It should be pointed out that for a

volume ratio of 99:1, and SQ_{expt} = 99.5%, the ASC is now 50%. In other words, a large volume ratio places stringent requirements on SQ_{expt}. In localized spectroscopy, where absolute signal contamination is of critical importance, the ASC can be easily estimated using Eq. [2.13] once SQ_{expt}, D, d, L and *l* are known.

2.6 *Materials and Methods*

All the experiments were performed on a 1.9 T small bore (diameter 15 cm) Bruker Biospec NMR imager. To observe localization, a cylindrical phantom of inner diameter 11.5 cm and length 6 cm was filled with a solution of 1 mM copper sulphate and saline. The relaxation times of the doped solution were $T_1 \sim 1$s and $T_2 \sim 400$ ms. A case (D = 2d) of eq. [2.7] (*i.e.* $\cos(3\pi x)\ \mathrm{sinc}(\pi x)$) was taken as the waveform of the saturation pulse $B_1(t)$ to isolate a ROI of diameter (d) 5.7 cm at the center of the phantom by presaturating an outer cylindrical volume of diameter (D) 11.5 cm. The $B_1(t)$ waveform, truncated after eight zero-crossings, consisted of 512 complex points. The duration of the pulse was 0.5 ms and the tip-angle was about 30°.

Saturation pulses were applied in combination with a rotating gradient of amplitude 3.63 mT/m as shown by the pulse sequence of Fig. 2.3. The rotating gradient was formed by simultaneously applying two identical sinusoidal gradients with a 90° phase shift between them (cosinusoidal x and sinusoidal y gradients in Fig. 2.3). The resulting gradient vector of constant magnitude sweeps the x-y plane with the axis of rotation along the z-direction. The pulses were repeated at stepwise equal angular intervals over a single half cycle of the rotating gradient. The angular intervals of

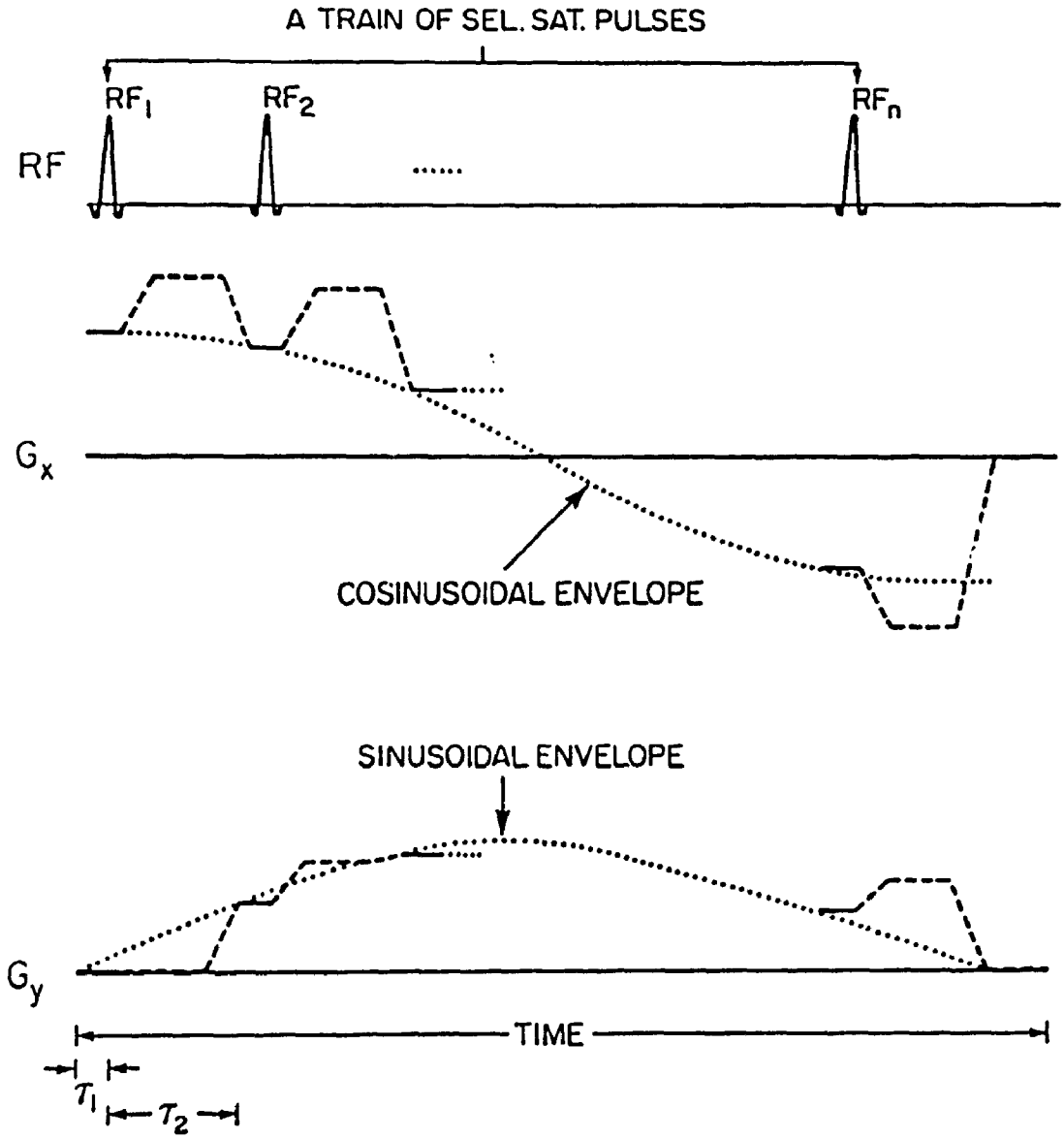

FIG. 2.3. Localization sequence to isolate the region of interset (ROI) described in Fig. 2.2 at the center of the phantom. Spoiler gradients (dashed lines) are needed when fast localization and/or presaturation of a large outer region (OR) is required. Otherwise, for the minimum rf pulse width τ_1 required for a given small ($\leq 30^{\circ}$) tip-angle, the strongest possible slice-select gradient (solid lines) can be chosen to keep the interpulse interval τ_2 short ($\leq$ 1 ms).

rotation were determined using $\Delta\theta_G = 180/n$, where n is the number of repetitions of the saturation pulses. The direction of the rotating gradient was held fixed at those angles at which the pulses were applied for an appropriate length of time before switching the gradient to the direction for the next excitation.

The optimum interpulse interval, (τ_2 in Fig. 2.3) was determined for a given gradient strength (note that the longitudinal magnetization of the outer volume recovers during the localization procedure, therefore, the optimum τ_2 time has to be determined to dephase the outer volume signal adequately with the least possible recovery of the unwanted longitudinal magnetization of the outer volume). τ_2 can be reduced by using the sequence of spoiler gradients shown by the dashed lines in Fig. 2.3. These spoiler gradients are created simply by increasing the amplitude of the rotating gradient appropriately during the τ_2 time. Such a scheme does not affect the size and sharpness of the edges of the ROI; however, it does allow the stronger spoiler gradients to dephase the transverse magnetization of the outer volume adequately in a shorter time.

Multiple excitation followed by continuous gradient dephasing of the transversemagnetization of the outer region leads to the suppression (spoiling) of the outer volume magnetization, thus isolating an axial rod (cylinder) of spins whose magnetization is virtually untouched by the sequence of Fig. 2.3. The observed diameter of the cylinder was about 5.7 cm as desired, and its length unlimited, in principle, in the z-direction.

The localization sequence, illustrated in Fig. 2.3, was then combined with a conventional 2DFT (spin warp) imaging sequence to image a transverse slice of the

isolated cylinder (phantom). The delay between the center of the last saturation pulse in the localization sequence and the center of the signal excitation pulse ("read pulse") was about 3 ms. The "read pulse" was made selective in the z-direction, limiting the length of the isolated cylinder to 7 mm. The field of view was 14 cm. A volume imaging coil was used in the transmit/receive mode, *i.e.* no surface receive coil was used to limit the field of signal reception. No signal averaging or phase cycling of the rf was performed. All the data were acquired from a single-slice, first-echo in the quadrature detection mode, with a sampling bandwidth of 25 kHz and an image matrix of 128 x 128.

2.7 *Experimental Results*

The experimental saturation profile of a single rf pulse as described in the previous section is shown in Fig. 2.4. The result demonstrates two non-ideal features. First, there is some unwanted excitation within the ROI. Second, the pulse excites the outer region non-uniformly: the profile exhibits oscillations within the ROI and the outer volume boundaries, the top portion is not flat as well, and the finite transition regions lead to imperfect definition of the ROI. These features arise from truncating the time-domain waveform of the rf pulse (after 8 zero-crossings in this case), an action whichintroduces oscillations (side lobes) in the profile in the temporal-frequency-domain. A slight asymmetry in the structure of the profile is also noted, which is a consequence of magnetic field inhomogeneities and not of the rf saturation pulse shape.

In accord with the localization sequence of Fig. 2.3, saturation pulses were repeated in combination with the rotating gradient. The effect of the number of

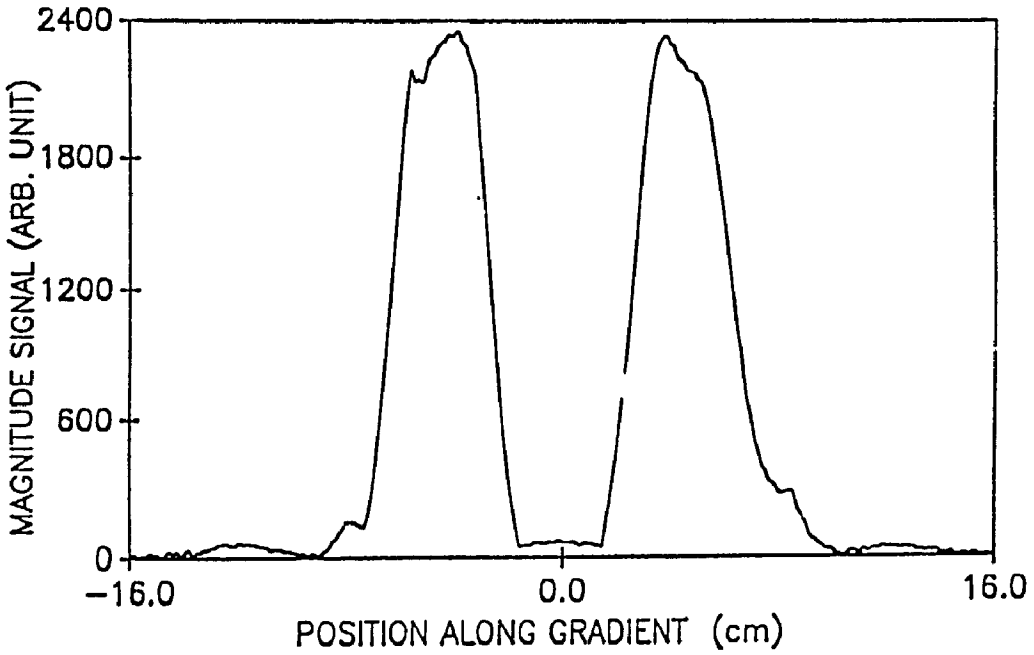

FIG. 2.4. Experimental one-dimensional saturation profile corresponding to Fig. 2.2, for a rf pulse of tip-angle about 30° and waveform $\cos(3\pi x)\ \mathrm{sinc}(\pi x)$, truncated after 8 zero-crossings.

repetitions on the suppression of the outer signal, as well as on ROI boundary sharpness is demonstrated in Fig. 2.5. Figure 2.5a shows the effect of the number of repetitions of these saturation pulses on the suppression quality factor SQ_{expt}. For comparison, also plotted in Fig. 2.5a is the SQ_{th} for the same rf tip-angle (i.e., 30°). The pulses were repeated 6, 12, 18, 24, and 36 times during the 180-degree rotation of the gradient. The images and image intensity profiles of the transverse slice of the cylindrical phantom for 0, 6, 12 and 18 repeats are shown in Figs. 2.5b, 2.5c, 2.5d and 2.5e, respectively. As is clear from Fig. 2.5, the outer volume suppression and the ROI boundary sharpness both improve as the number of repetitions is increased. The outer volume is suppressed adequately ($SQ_{expt} \sim 99.9\%$, $SQ_{th} \sim 99.43\%$) using 36 rf pulses (Fig. 2.5a).

In order to effectively dephase the transverse magnetization while allowing only a minimum recovery of the longitudinal magnetization of the outer region, the optimal τ_2 time corresponding to the rotating gradient strength of 3.63 mT/m was sought. For the case of 12 repetitions of the rf pulses, the effect of the length of τ_2 on the suppression quality, SQ_{expt}, is shown in Fig. 2.6. The optimum τ_2 for this case is about 3 ms. For longer τ_2 the outer volume signal suppression quality is degraded by the significant signal contribution from the outer region, which results from the partial recovery of its longitudinal magnetization. For τ_2 shorter than optimal, artifactual periodic modulation of the signal intensity from the outer region in the form of concentric circular bands was observed in the slice image. The spatial periodic modulation of the outer volume magnetization resulted because inadequate time was allowed to dephase the existing transverse magnetization after each excitation. The total

FIG. 2.5. (a) Suppression quality (SQ_{expt} - open circles, SQ_{th} - filled circles) versus number of repetitions, in a 180°-rotation of the gradient for about 30° tip-angle rf pulses. (b-e) Phantom transverse-slice images, and the corresponding intensity profiles along the phase encoding direction (horizontally here) for (b) 0, (c) 6, (d) 12 and (e) 18 repetitions. As the number of repetitions increases, the suppression quality and ROI boundary sharpness both improve. The total localization time for the cases (c)-(e) was 10, 20 and 30 ms, respectively, and the dead time was 3 ms in each case.

(a)

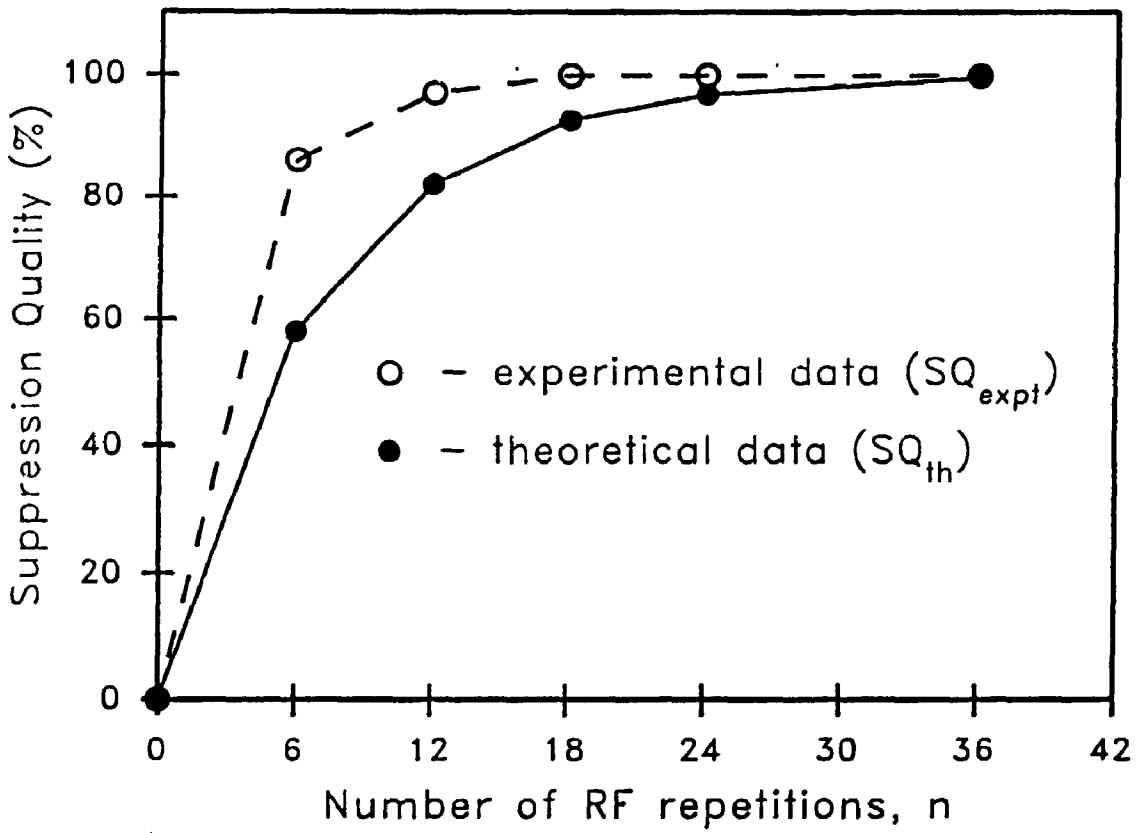
Suppression Quality (%)
100
80
60
40
20
0
0
6
12
18
24
30
36
42
Number of RF repetitions, n
O – experimental data (SQ_{expt})
● – theoretical data (SQ_{th})

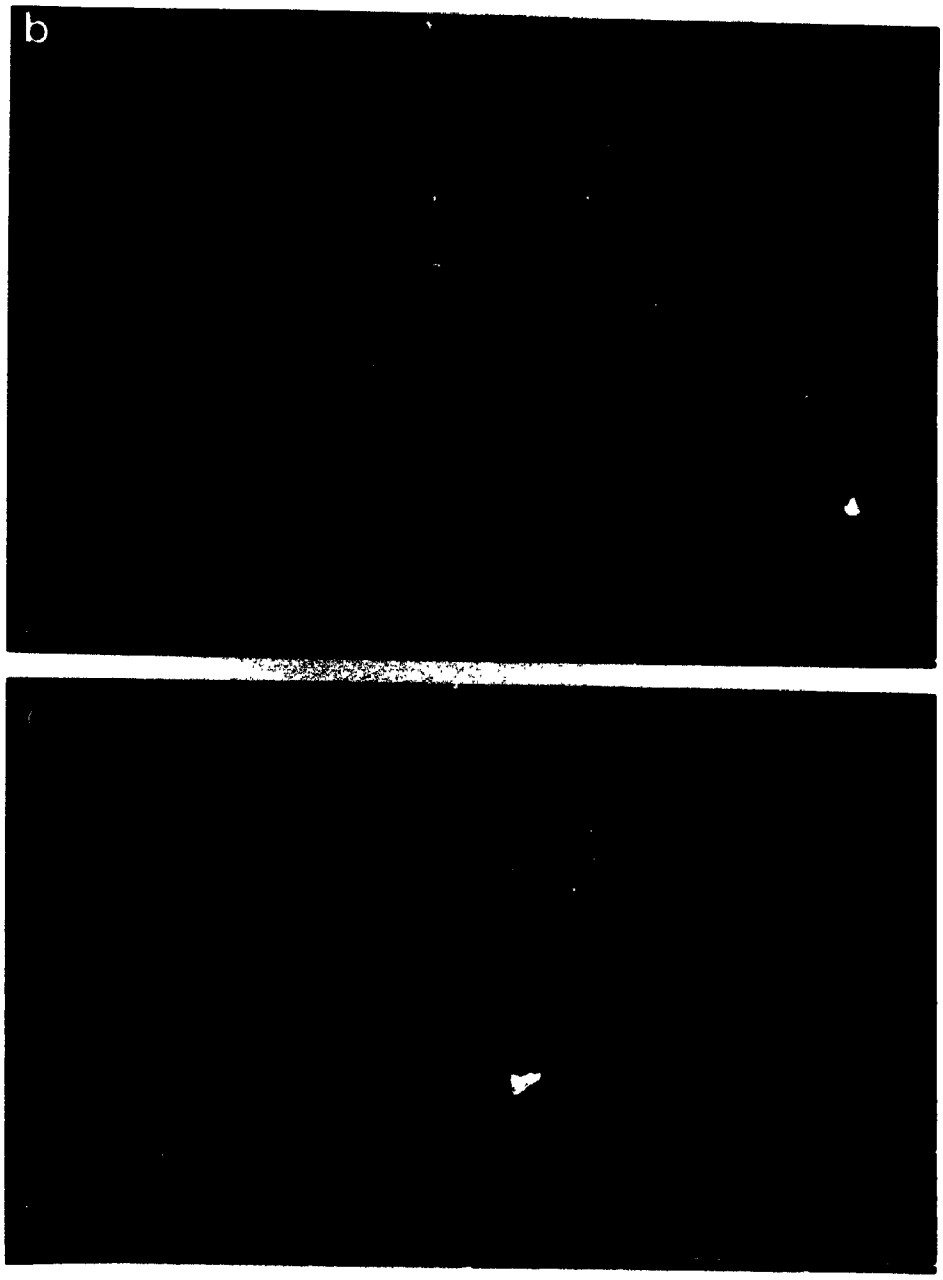

FIG. 2.5 continued .....

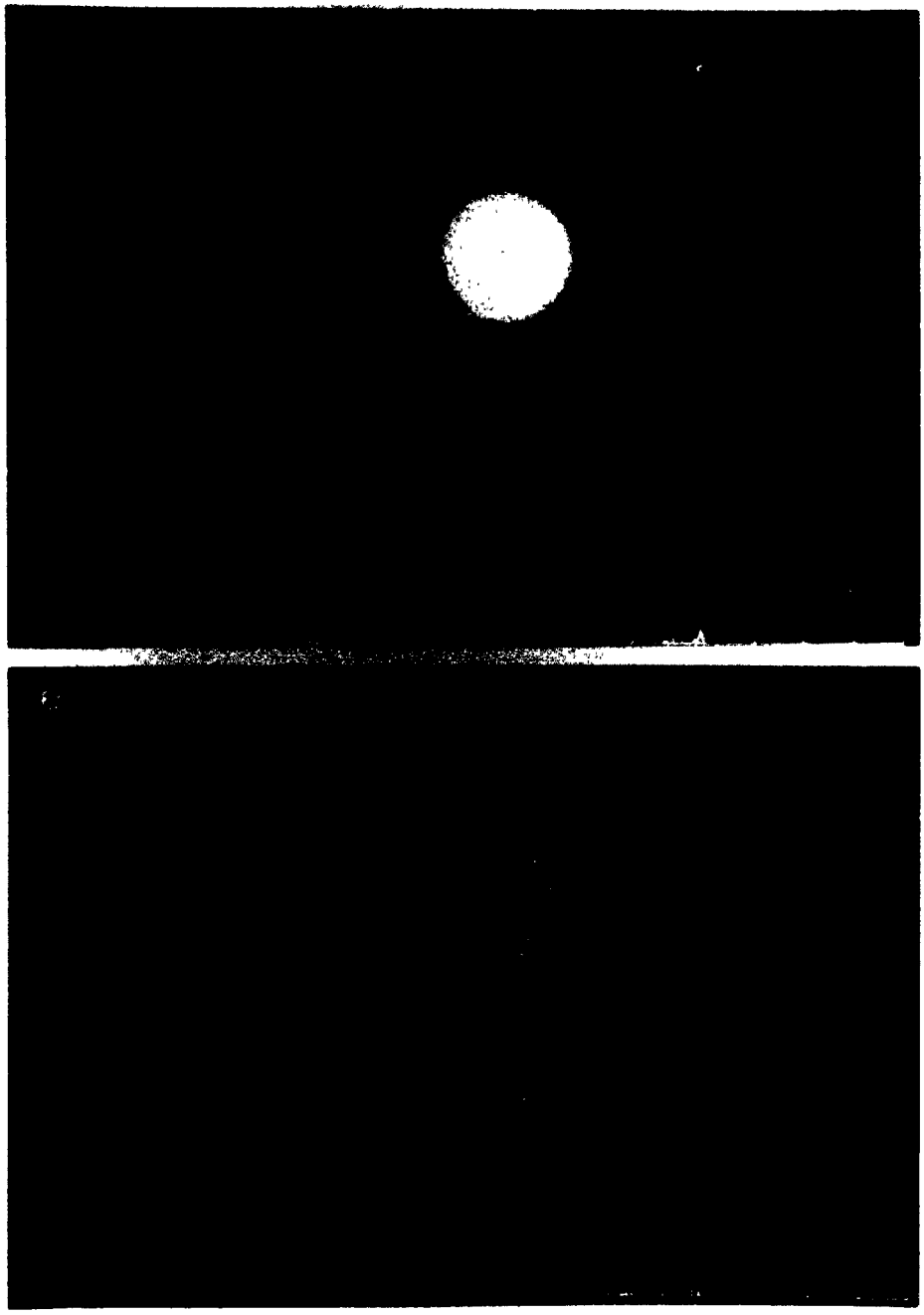

FIG. 2.5 continued .....

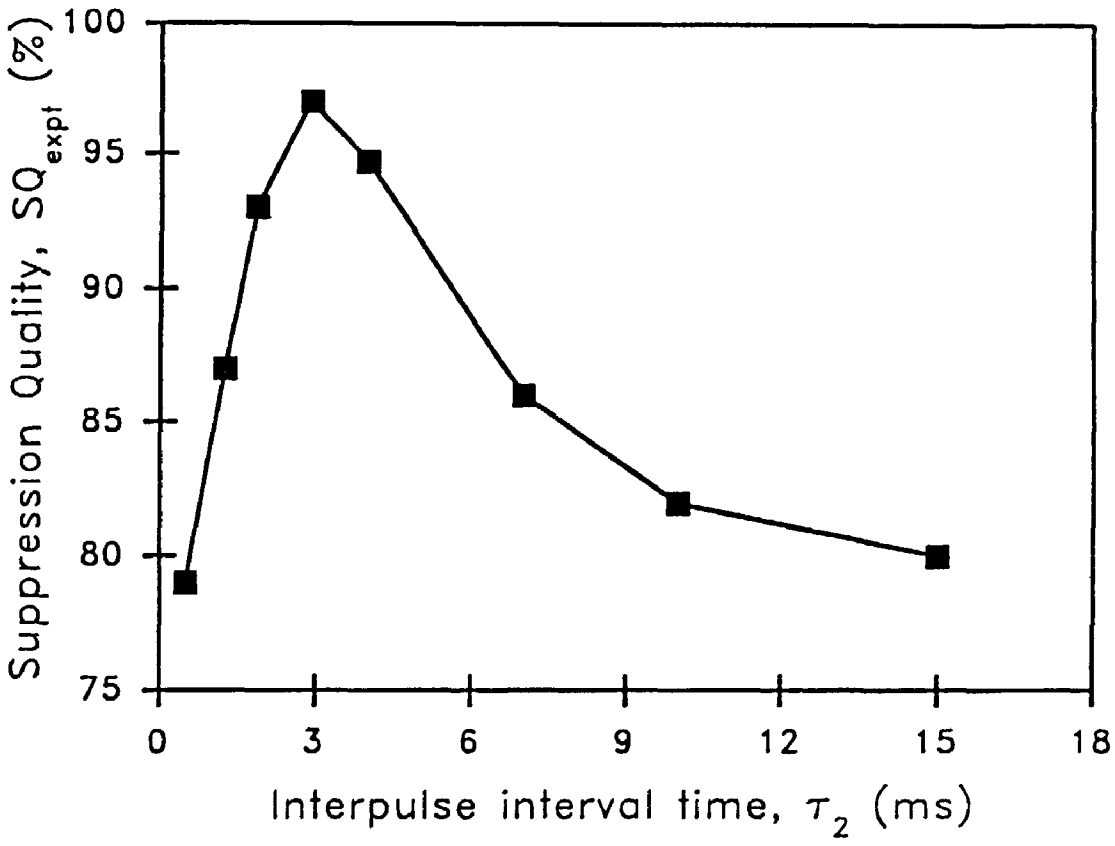

FIG. 2.6. Suppression quality SQ_{expt} (Eq. [2.11]) vs. interpulse interval time τ_2, for the case of twelve 30° rf pulses and a rotating gradient amplitude of 3.63 mT/m. The optimum occurs at τ_2 = 3 ms in this case.

localization time, TL, is TL = $n(\tau_1 + \tau_2)$, where τ_1 is the rf pulse width, τ_2 is the interpulse interval time and n is the number of rf pulses. Choosing the optimal value of τ_2 = 3 ms and n = 18 given in Figs. 2.5 and 2.6 leads to TL = 63 ms. When the optimal interpulse time τ_2 was reduced to about 1 ms by using a rotating spoiler gradient amplitude of 9 mT/m in the inter-pulse interval, the total localization time TL became about 30 ms. It was found that the rotating spoiler gradient depicted in Fig. 2.3 was very effective in scrambling the phase of the outer volume signal as shown by the fact that no unwanted spin echo or stimulated echo formation occurred as a result of the repeated application of selective saturation rf pulses.

The time delay (which I call "dead time") allowed between the end of the localization sequence and the onset of the readout pulse also affects the accuracy of spatial presaturation and hence the localization of the ROI, since the longitudinal magnetization of the outer region recovers during this time. Therefore, in order to reduce the effect of partial recovery of the longitudinal magnetization of the outer volum on the suppression quality, the waiting time should be kept to the minimum (though limited by the hardware) even using the optimized pulse sequence of Fig. 2.3.

The ability of this technique to isolate a ROI has also been demonstrated by an *in vivo* study (Fig. 2.7). A scout transverse-slice image was taken through the head of a guinea pig to select a ROI of diameter 2 cm and length 3 mm, which included the brain. Then transverse-slice images were obtained without and with localization of the ROI. These are shown in Figs. 2.7a and 2.7b, respectively. For 18 rf pulses, each

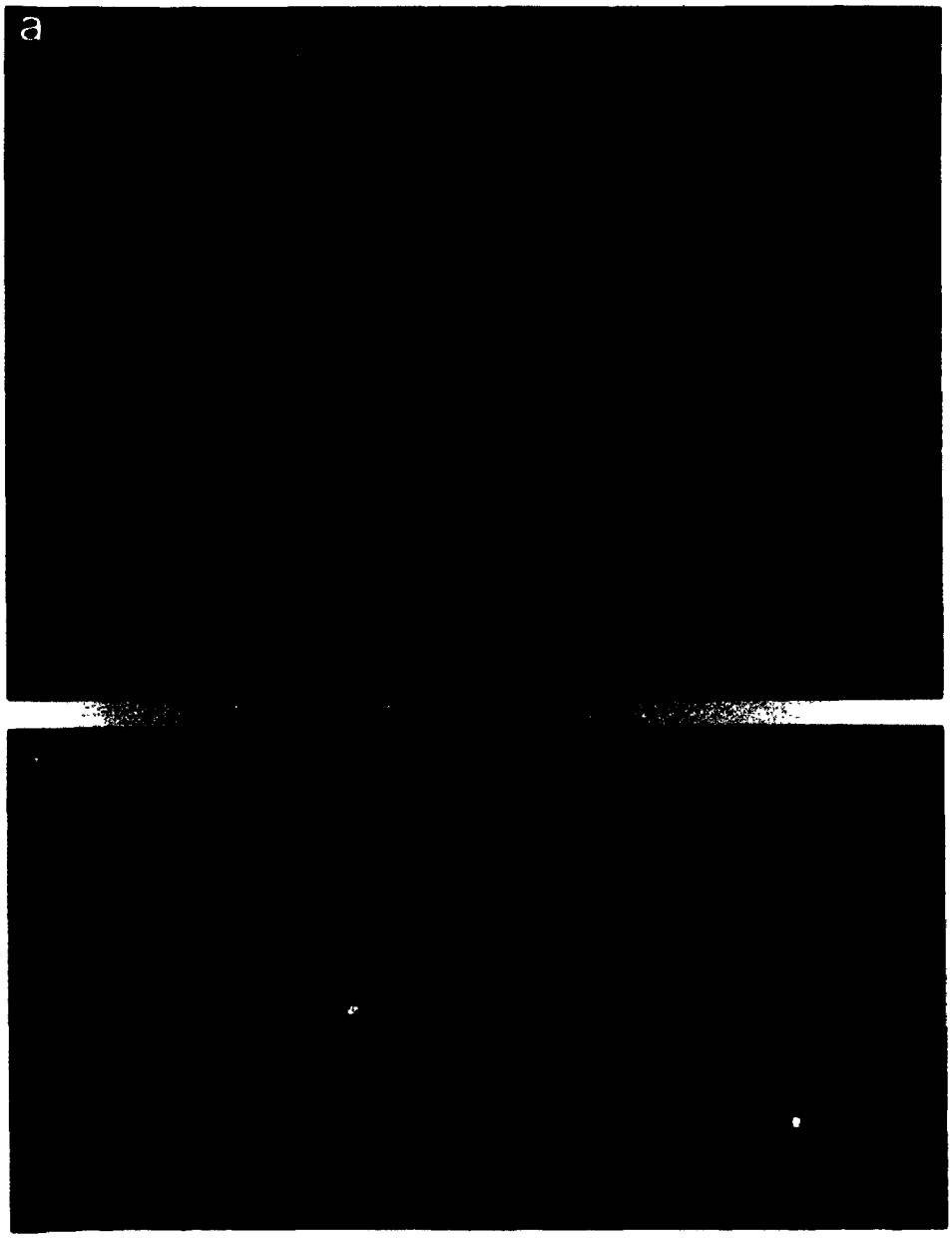

FIG. 2.7. Transverse images of the head of a guinea pig (a) without suppression; (b) with suppression of the outer region. Using 18 repetitions of about 30° rf pulses, a ROI (2 cm diameter by 3 mm length) has been isolated, by suppressing signal from the surrounding tissues to a suppression quality (Eq. [2.11]) SQ_{expt} better than 95%. The total localization time was 30 ms and the dead time was 3 ms.

pulse of tip-angle about 30°, and a rotating gradient of amplitude 5.435 mT/m, the outer region was suppressed adequately, as it is shown in Fig. 2.7b. Again, the volume imaging coil was used in transmit/receive mode and no signal averaging or phase cycling of the rf pulses was performed.

2.8 *Discussions and Conclusions*

In this chapter, a new technique for multi-dimensional spatial localization by selective spatial presaturation is introduced. An analytical method based on the small-tip-angle approximation was presented to design the shape of the small-tip-angle saturation rf pulses. The experimental work demonstrates that a series of such pulses, in combination with a constant amplitude rotating gradient, suppresses the signal adequately from the region outside of a cylindrical volume. For example, using 36 gradient angles and rf pulses, each pulse of duration 0.5 ms and tip-angle 30°, the outer volume signal was suppressed to a SQ_{expt} of ~ 99.9%. The use of a spoiler gradient of optimal amplitude and duration in the interpulse interval allowed us to reduce the total localization time to about 60 ms, thus making the localization technique relatively fast. The efficacy of the technique was demonstrated in a phantom as well as *in vivo*.

The suppression quality measured, SQ_{expt}, from the ROI of Fig. 2.5 was in close agreement with the corresponding theoretical value, SQ_{th} (see Fig. 2.5a). For example, for n=36, θ=30°, the SQ_{expt} was 99.9% which compares well (within 0.5%) with its counterpart $SQ_{th} \approx 99.5\%$. The slight difference between the two values arises possibly because of the uncertainty in rf power setting to produce a 30° tip-angle.

Spatial localization by Projection Presaturation is accurate since the technique does not suffer from the problems such as tip-angle errors and imperfections in slice-selection profiles. These problems are the major causes of inaccuracy in volume localization by existing techniques, as discussed in chapter I. For example, the LOCUS (*20*) technique, using twelve 90° frequency-offset sinc pulses, achieves only 95% suppression of the outer volume signal in about 40 ms. That the suppression is not better results from the fact that LOCUS requires high rf-homogeneity to saturate the spins outside the ROI more accurately. In reality, the inhomogeneity of the rf transmit field causes a tip-angle error in 90° sinc pulses (i.e. actual transmitted tip-angle is either > 90° or < 90° depending upon the uncertainty in rf power setting), leading to inaccurate suppression of the outer volume magnetization. Also, because of the use of large-tip-angle (90°) rf pulses, the degraded slice-profile results in a poorly defined ROI.

In contrast, Projection Presaturation is not susceptible to such errors because it employs repeated applications of small-tip-angle rf pulses. In principle, small-tip-angle saturation pulses (*i.e.* pulses of less than or equal to 30° tip-angle, for which the small-tip-angle linear approximation is valid (*36*)) can be repeated an appropriate number of times until all the longitudinal magnetization of the outer region has been tipped into the transverse plane and completely dephased by the rotating gradient. For practical purposes, as shown, 36 rf pulses of tip-angle about 30° are sufficient to suppress the outer volume signal adequately; however, more rf pulses can be used if a higher SQ is needed. Moreover, the localized ROI has a well defined boundary. This statement is verified by the result that the diameter (5.7 cm) of the localized cylindrical ROI, reported

in this chapter (Fig. 2.5e), was in excellent agreement with the desired theoretical value.

The choice of rf pulse tip-angle close to 30° (limit of the small-tip-angle regime) was made to keep n and TL both to a minimum, while achieving an adequate SQ_{expt}. To estimate the rf tip-angle, first the rf pulse width and the amplitude for a 90° tip-angle were determined, and then these parameters were scaled linearly to yield a small-tip-angle, *e.g.*, 30°. Such a procedure would lead to tip-angle errors in the presence of non-linearity in the rf amplifier. However, in the method of Projection Presaturation, the tip-angle accuracy is not critically important; what is important is the appropriate number of rf repetitions to achieve adequate suppression.

The use of a rotating spoiler gradient in the interpulse interval makes localizing a ROI by Projection Presaturation relatively fast (60 ms total localization time). Spoiler gradients of increased amplitude are needed when a large outer region (greater than about 10 cm outer diameter) is being suppressed, since, the excitation of such a region will require the use of a relatively weak gradient (solid lines in Fig. 2.3) in combination with a short rf pulse of tip-angle 30°. For presaturating a smaller outer region (*e.g.*, for laboratory animal studies), a strong (amplitude ~ 9 mT/m) rotating gradient (solid lines in Fig. 2.3), in combination with the same rf pulse, can be found which will alone be adequate to dephase the outer volume signal in a short time ($\tau_2 \leq 1$ ms).

The experimental saturation profile (Fig. 2.4) of the small-tip-angle rf pulse has non-zero (~ 3%) magnitude (instead of zero) in the ROI and finite, though narrow, transition zones which increase with the size of the exterior volume. These imperfections in the profile can be further improved by taking more zero-crossings in the time-domain

waveform of the cossinc rf pulse, at the expense of a longer pulse for the same tip-angle and therefore a longer localization time TL. A trade-off between the ROI sharpness and the total localization time and, hence, suppression quality must therefore be made.

Although optimized large-tip-angle (*e.g.* 90°) selective cossinc saturation rf pulses (*38*) can be applied in three orthogonal directions to localize a cubical volume, the suppression of the outer volume may not be adequate in the presence of mistuning of the rf pulses (tip-angle error) or spatial inhomogeneities in the rf transmit field. The accuracy of saturation can only be improved by repeated application of selective saturation rf pulses, although this is achieved at the expense of a longer localization time, TL. However, it must be noted that if TL becomes significant when compared to the T_1 of the outer volume species, the quality of outer volume suppression by Projection Presaturation or any other method based on selective spatial presaturation (as described in chapter 1) is degraded. The degradation in suppression results from the fact that the saturated spins of the unwanted regions (outer region) recover during the localization time TL due to the T_1 relaxation mechanisms.

The T_1-dependence of suppression quality achieved by Projection Presaturation raises concerns about the accuracy of localization in the presence of short T_1 species in the outer region. For a TL = 60 ms, the problem should not be a major one because the proton T_1 of human tissues is typically of the order of several hundred milliseconds or longer. The challenge of localization for T_1 comparable to TL can be met by using a non-selective 180° rf pulse that is alternately turned on/off in front of the localization sequence (*20,23,34,35*). Identical T_1 recovery will occur from the outer volume

following the localization sequence so the unwanted signal from exterior volume will cancel out on data subtraction, whereas the ROI signals will be of opposite sign and will add up. A real limitation of Projection Presaturation or any selective presaturation technique will appear when T_1 is comparable to the interpulse interval or the dead time. In that case, the ROI signals will be of the same sign and therefore the data subtraction cycle can no longer be used.

In vivo localized spectroscopy will certainly benefit from this new localization technique. Following the localization of a cylindrical ROI using Projection Presaturation, the magnetization within the ROI can be interrogated using a "hard" pulse to obtain the localized spectra from a 2D volume without any T_2 or T_2^* weighting. For acquiring localized spectra from a 3D volume in the case of short T_2 species (*e.g.* ^{31}P), T_2 or T_2^* independent spectra can be obtained by presaturating the third dimension (axis of gradient rotation) following the 2D Projection Presaturation localization sequence, using an optimized cossinc rf pulse of 90° tip-angle (*39*) and then using a "hard" pulse to acquire the spectral data from a truly 3D localized volume. Alternatively, the slice-selective sinc pulse can be replaced with a self-refocussed rf pulse to minimize or almost eliminate the effect of T_2 or T_2^* decay on the ROI signal. For example, a specially designed slice-selective excitation pulse sequence (*39*) for short T_2 species can be used in conjunction with Projection Presaturation to keep the ROI signal T_2 independent.

For *in vivo* application of this technique, the rf power deposition or more specifically the specific absorption rate (SAR) in tissues will be similar to single slice-multiecho NMR imaging techniques used in common clinical situations. For example,

the SAR of Projection Presaturation using 36 30° rf pulses, each of duration 0.5 ms, relative to a sequence of single 90°, and four 180° rf pulses corresponding to four echoes, each pulse of duration 3.2 ms, will be equal to 36 * [$(30)^2$ / 0.5] divided by [$(90)^2$/3.2 + 4 * $(180)^2$/3.2] which is approximately equal to 1.5. In the above calculation, the relation that SAR $\propto$ (tip-angle)^2/pulse-duration has been used. For the application of the method to imaging which does not require as high SQ_{th} as spectroscopy, Projection Presaturation pulses of smaller tip-angle, *e.g.*, 20° (for n = 36, SQ_{th} = 99.5% for θ = 30° and SQ_{th} = 90% for θ = 20°) can be used in which case the SAR of the method reduces to 66% of that of the four echoes sequence or to 126% of that of the two echoes sequence. Hence, from rf power deposition point of view, the use of this method in combination with a standard imaging sequence should be of no concern.

In summary, the method presented in this chapter allows one to isolate a ROI with SQ_{expt} ~ 99.9% in a relatively short time (about 60 ms). The description and implementation of the method was specialized to the case of a single, centered, cylindrical ROI only. It is desirable, however, that the method should allow one to isolate a ROI of any desired shape (not necessarily cylindrical) at predetermined positions without having to reposition the object physically. If this can be done, it will certainly increase the utility of this method for *in vivo*, and clinical studies. Furthermore, simultaneous isolation of multiple ROIs within a given object will be an attractive asset for many applications of this method to *in vivo* studies. These are the issues which I address in the next chapter.

CHAPTER 3

Localization of Multiple Regions of Interest: A Generalized Approach

3.1 *Introduction*

In a previous chapter the Projection Presaturation method was introduced for single-shot multi-dimensional spatial localization by spatial presaturation. It was shown how a series of selective, small-tip-angle (30°) rf pulses of cos-sinc waveform, applied during a constant amplitude rotating gradient, could localize a single, centered, cylindrical region of interest (ROI) by presaturating a hollow outer cylindrical volume. The technique proved to be relatively fast (30 - 60 ms total localization time) and accurate (> 99% suppression of signal from the outer region).

The simple Projection Presaturation method presented earlier is not ideal for three reasons: 1) It localizes a single ROI only. The ideal technique should allow for the simultaneous isolation of multiple ROIs, permitting spectroscopic or imaging data to be acquired from such ROIs under identical conditions. 2) It localizes cylindrical ROIs only. *In vivo* targets will not in general have cylindrical geometry, *e.g.*, tumour, myocardium, kidneys, lungs etc. Ideally, the ROI shape should be matched to the target, allowing a maximum S/N ratio with a minimum of signal contamination from outside the ROI. 3) It localizes only on-center ROIs. The ideal localization technique should be able to localize ROIs accurately at arbitrary positions within the three-dimensional volume. This chapter extends and generalizes the simple Projection Presaturation method by removing these restrictions.

A number of investigators have developed localization techniques which solve one or more of the above problems. Sharp et al. (*40*) described a conformal spectroscopy technique, called C-ISIS, for localizing irregular, polyhedral, *in vivo* targets. The technique uses ISIS inversion pulses applied in directions orthogonal to the faces of a polyhedron which has been designed to conform to the target shape. The addition of each extra side to the polyhedral ROI doubles the data acquisition time and requires additional inversion pulses, compared to the standard ISIS technique (*6*) for localizing a cuboidal volume. Thus, the more accurate conformation is achieved at the expense of a longer localization time and possibly a drop in S/N ratio within the ROI, because, in the time required for the additional inversion pulses, the longitudinal magnetization recovers partly. Nevertheless, the S/N ratio is enhanced by the more accurate matching of ROI to target.

A tilted gradient method (*41*) has been reported to isolate two ROIs simultaneously. However, the technique does not permit the independent positioning of each of the two ROIs, and is therefore of limited utility for *in vivo* studies.

To overcome the above mentioned problems, the Projection Presaturation technique has been extended to localize multiple, polyhedral, arbitrarily-positioned ROIs. Off-center localization by this technique is simple and accurate. Furthermore, T_2- or T_2^* -independent data can be acquired simultaneously from multiple ROIs. First an analytical method to design the saturation rf pulses for isolating such ROIs is presented. Next, the performance of this method is evaluated experimentally on phantoms.

3.2 *Theory*

In Projection Presaturation, a series of saturation rf pulses is applied during at least one half cycle of a "rotating" gradient. Figure 3.1 depicts the Projection Presaturation pulse sequence for one complete cycle of the rotating gradient. For the simple case of a single cylindrical, centered ROI, the saturation rf pulse shape is the same for all saturation pulses. This pulse shape has a one-dimensional profile containing an unexcited region at its center which encloses the projection of the ROI at all angles of gradient rotation. Now the simple theory is extended by deriving the profiles required to isolate a single off-center ROI which will be a cylinder of convex polyhedral section, then generalized to the case of multiple ROIs. Having derived these profiles, and assuming small-tip-angle excitation, the saturation rf pulse shapes are determined by inverse Fourier transformation of the corresponding profiles. In general, these rf pulse shapes will be different at each angle of application.

An ideal localization technique would optimize the S/N ratio from *in vivo* targets by conforming the ROI shape to a high order irregular polyhedron, which closely approximates the target shape. A transverse section of such a ROI is a polygon, as shown in Fig. 3.2a. Let the vertices of this polygon be described by a set of polar co-ordinates $\{(r_i, \theta_i)\} i = 1, m$ where m is the minimum number of sides needed to match the ROI shape to the target with desired accuracy. In general, the number of vertices should be less than the number of saturation rf pulses required for adequate outer-volume suppression (36 30° tip-angle rf pulses for outer volume suppression > 99%), so that the shape of the localized ROI will be determined by these vertices rather than

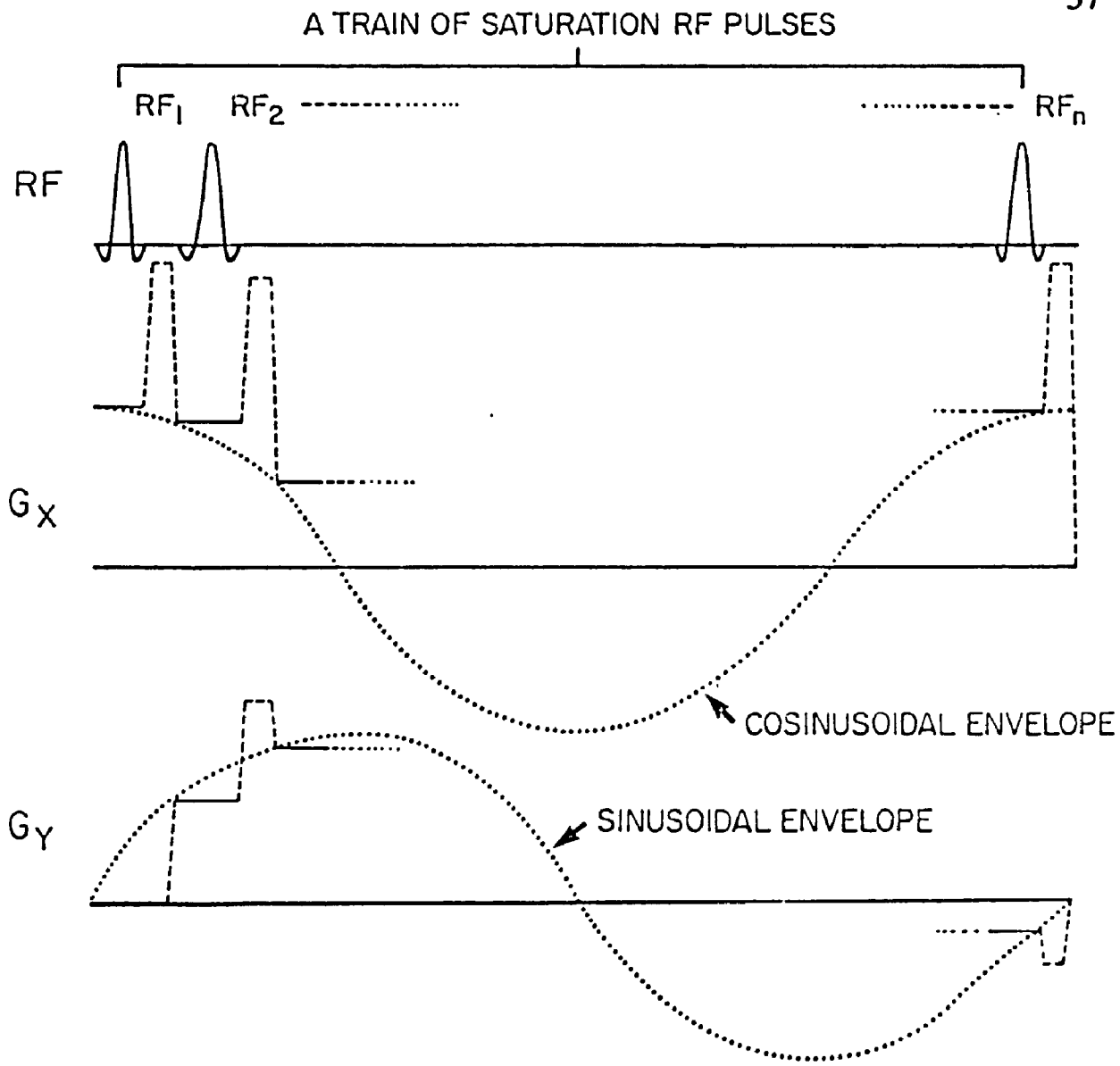

FIG. 3.1. General localization sequence to isolate regions of interest by presaturating the region outside the ROIs. The saturation rf pulse symbolically shown at a particular angle of gradient rotation represents a single or group of rf sub-pulses of appropriate shapes required by the particular experiment. To keep the total localization time short, spoiler gradients (dashed lines) of increased amplitude are used to dephase quickly the existing transverse magnetization after the application of rf pulse at each angle.

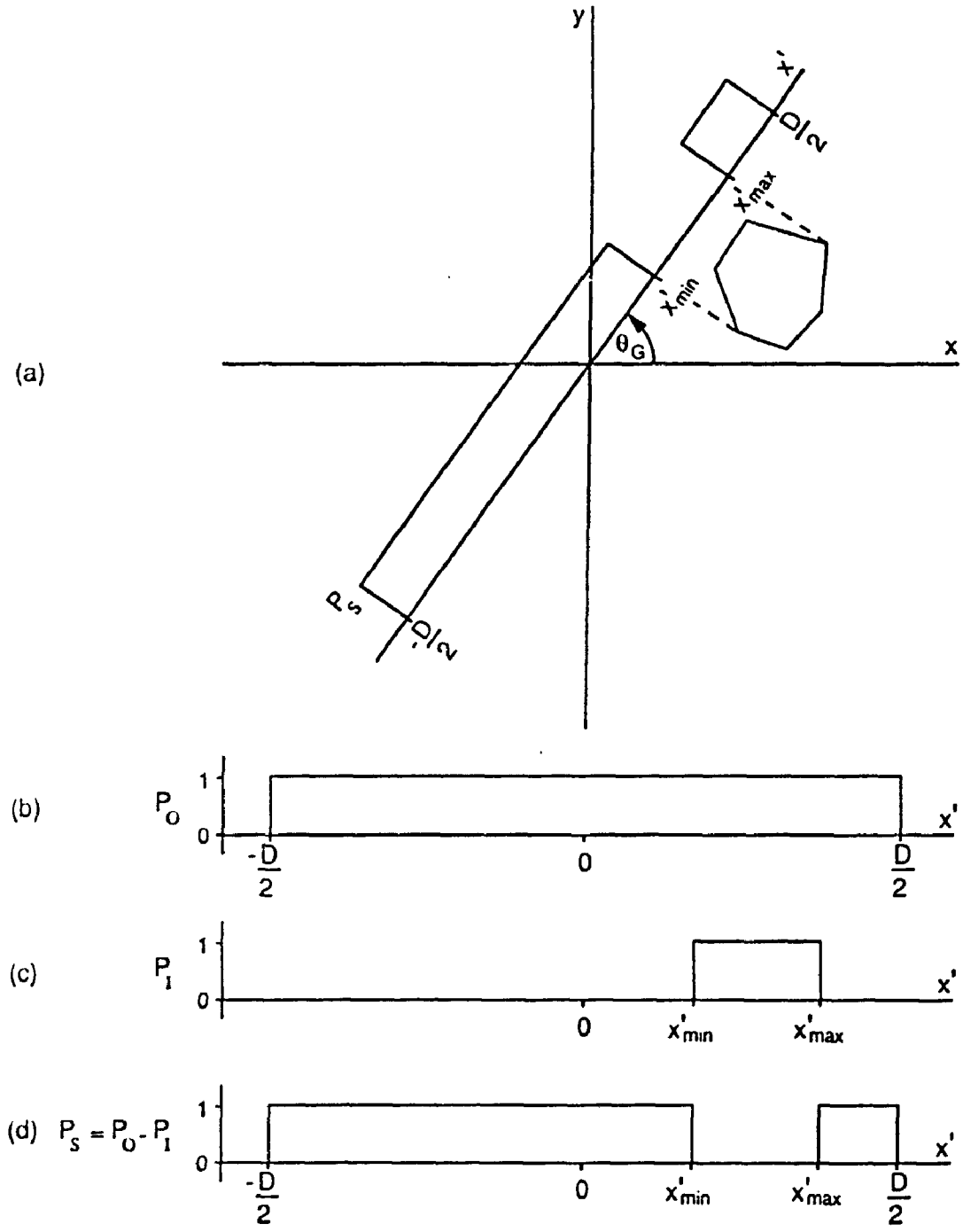

FIG. 3.2. Forming a single saturation profile for localizing a single, off-center, irregular polyhedral ROI: (a) a transverse section of an irregular polyhedral ROI and the saturation profile, P_s, required by Projection Presaturation at the given gradient angle θ_G; (b) a single profile, P_o, which, by itself, would excite the entire object of diameter D; (c) a single "inverted" profile, P_I, which, by itself, would excite a band encompassing the ROI; (d) the difference profile, P_s, of P_o and P_I, which is identical to the profile P_s in Fig. a.

by the finite number of projection angles. At a given angle of the rotating gradient, θ_G, the projected positions of these vertices are given by:

$$\{x'_i(\theta_G)\}_{i=1,m} = \{r_i \cos(\theta_G - \theta_i)\}_{i=1,m} , \quad [3.1]$$

where all the angles are measured from the positive x-axis and the sense of positive rotation is anti-clockwise. From these projected positions, let us define the maximum and the minimum:

$$x'_{max}(\theta_G) \equiv \text{MAX}\ \{x'_i(\theta_G)\}_{i=1,m} , \quad [3.2a]$$

$$x'_{min}(\theta_G) \equiv \text{MIN}\ \{x'_i(\theta_G)\}_{i=1,m} . \quad [3.2b]$$

Projection Presaturation requires the application of saturation rf pulses whose one-dimensional excitation profiles are zero within and unity outside the projection of the ROI onto the direction of the rotating gradient at the time of the rf application, as shown in Fig. 3.2a. Each single excitation profile P_s can be expressed as a difference of two individual profiles, shown in Figs. 3.2b - 3.2d, viz.

$$P_s(x', \theta_G) = P_o(x') - P_I(x', \theta_G) . \quad [3.3]$$

P_o by itself would excite the entire object, and is the same for all angles, and P_I by itself would excite a band encompassing the ROI, *i.e.* P_I represents the "inverted" saturation profile, and is a function of θ_G. P_o and P_I can be defined analytically as:

$$P_o(x') = \text{RECT}\ [x'/ D] , \quad [3.4a]$$

$$P_I(x', \theta_G) = \text{RECT}\ [(x' - x'_C(\theta_G)) / x'_W(\theta_G)] , \quad [3.4b]$$

where

$$x'_C(\theta_G) = [x'_{max}(\theta_G) + x'_{min}(\theta_G)] / 2 , \quad [3.4c]$$

and

$$x'_W(\theta_G) = [x'_{max}(\theta_G) - x'_{min}(\theta_G)] \quad [3.4d]$$

are the center position and the width, respectively, of the RECT function shown in Fig. 3.2c. D is the diameter of a circle which bounds the object (in the x-y plane). Equation [3.3] allows us to generate a series of profiles $P_s(x', \theta_G)$ at different angles θ_G of the gradient rotation. These profiles are then used to determine the saturation rf pulse shapes, which, when applied sequentially at equal angular intervals in the presence of a constant amplitude rotating gradient, will saturate all magnetization outside the single, polyhedral off-center ROI.

Now this single ROI formalism is extended to the case of multiple ROIs located within the same object. Multiple ROIs are treated by first deriving the profile, $P_s^{(j)}$, for each $ROI^{(j)}$ considered singly, using Eq. [3.3], then defining a multiple profile, P_M, as the product of the N single profiles:

$$P_M(x', \theta_G) = \Pi_{j=1,N} \{P_s^{(j)}(x', \theta_G)\}. \quad [3.5]$$

An example of the formation of the multiple-profile P_M from two single profiles is shown schematically in Fig. 3.3. Since each single profile $P_s^{(j)}$ has an unexcited region enclosing the projection of $ROI^{(j)}$ at angle θ_G, the multiple-profile P_M will have multiple unexcited regions, enclosing the projections of all ROIs.

Changing the spatial variable x' to temporal frequency ν through:

$$\nu = (\gamma/2\pi)\, G_r\, x' , \quad [3.6]$$

where G_r is the constant amplitude of the rotating gradient, the rf pulse shape, $B_1(t, \theta_G)$, required to excite only the regions outside the ROIs can be obtained using the small-tip-angle approximation, as:

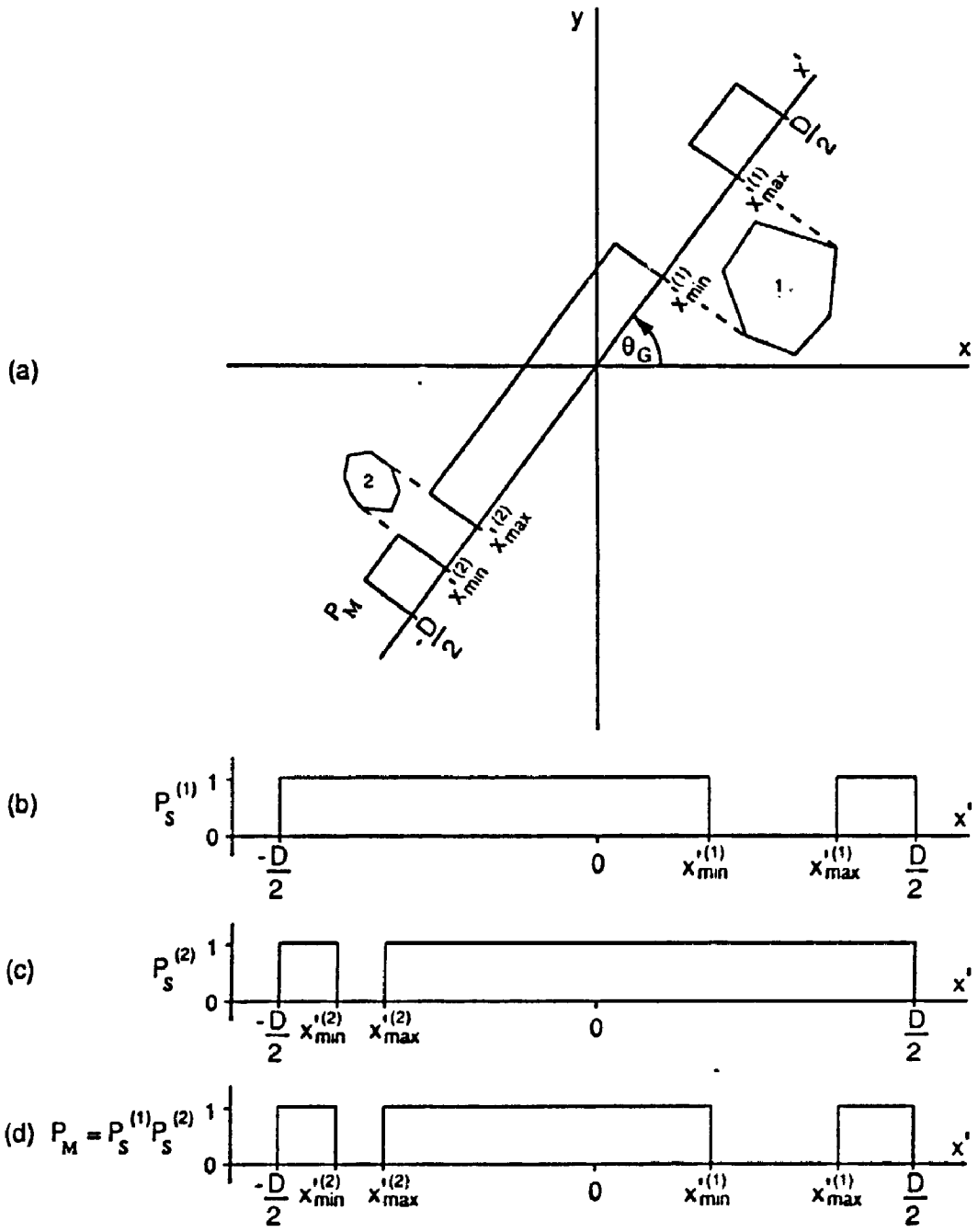

FIG. 3.3. The scheme for forming a single multiple-ROI profile, P_M, from a set of single-ROI profiles for the case of two ROIs: (a) two irregular polygons and the corresponding saturation profile shape, P_M, as required by Projection Presaturation; (b) single saturation profile, $P_s^{(1)}$, for ROI # 1 considered singly; (c) single profile, $P_s^{(2)}$, for ROI # 2 considered singly; (d) multiple profile, P_M, as a product of $P_s^{(1)}$ and $P_s^{(2)}$, which is identical to the profile, P_M, in Fig. a.

$$B_1(t, \theta_G) = FT_\nu^{-1} [P_M(\nu, \theta_G)] , \qquad [3.7]$$

where FT_ν^{-1} is the one-dimensional inverse Fourier transform integral operator. The Fourier integral in Eq. [3.7] can be evaluated either analytically or numerically to determine the rf pulse shapes. These rf pulses can then be applied at appropriate angular intervals in the presence of a constant amplitude rotating gradient to isolate multiple polyhedral ROIs simultaneously. Localization of the set of ROIs in the third dimension can be achieved by frequency-offsetting a selective readout pulse along the axis of gradient rotation, following 2D localization by Projection Presaturation. Alternatively, a non-selective readout pulse can be used to acquire data from multiple ROIs of polyhedral cylindrical shape.

The angles of gradient rotation can be chosen at equal angular intervals during one complete cycle of a constant amplitude rotating gradient. However, for localizing low order ROIs, e.g. rectangles, hexagons, etc., edge sharpness can be improved by choosing the angles of the gradient rotation as only those directions which are orthogonal to the sides of such ROIs. The saturation rf pulses as determined by Eq. [3.7] can then be applied multiple times alternately/cyclically at these angles to isolate this class of ROIs while presaturating the outside region adequately.

Though the technique presented above has been worked out for a gradient rotating in a plane (x-y) about an axis (z), and hence for localization in two dimensions (x and y) only, the method in a three-dimensional rotating gradient scheme can be used to localize true 3D volumes of irregular polyhedral shape, including conventional cuboids.

The multiple ROI profile P_M defined in Eq. [3.5] can be expressed alternatively

as a sum of non-overlapping RECT functions of various widths and center-offsets. Thus the analytical expression for the rf pulse shape which produces P_M is a sum of frequency-offset sinc functions. For example, for the case of a single ROI (N = 1), P_M in Eq. [3.7] can be expressed as a sum of two RECT functions as (see Fig. 3.2d):

$$P_M(\nu, \theta_G) = \sum_{j=a,b} \text{RECT}\,[(\nu - \nu_j(\theta_G))/\Delta\nu_j(\theta_G)]\,, \qquad [3.8]$$

where the widths and the center-offsets of the two RECT functions are given by

$$\Delta\nu_a(\theta_G) = (\gamma/4\pi)\, G_r\, [D - 2\, x'_{max}(\theta_G)]\,, \qquad [3.9a]$$

$$\Delta\nu_b(\theta_G) = (\gamma/4\pi)\, G_r\, [D + 2\, x'_{min}(\theta_G)]\,, \qquad [3.9b]$$

$$\nu_a(\theta_G) = (\gamma/8\pi)\, G_r\, [D + 2\, x'_{max}(\theta_G)]\,, \qquad [3.9c]$$

$$\nu_b(\theta_G) = -(\gamma/8\pi)\, G_r\, [D - 2\, x'_{min}(\theta_G)]\,, \qquad [3.9d]$$

The Fourier integral in Eq. [3.7] can then be evaluated analytically using the Fourier shift theorem to give the B_1 pulse shape as,

$$B_1(t, \theta_G) = \sum_{j=a,b} \text{sinc}(\pi\, \Delta\nu_j(\theta_G)\, t)\, \exp(i\, 2\pi\, \nu_j(\theta_G)\, t). \qquad [3.10]$$

Equation [3.10] gives the saturation rf pulse shape to localize a single, polyhedral, off-center ROI whose shape and size can be tailored using a set of points $\{(r_i, \theta_i)\}$ on its surface to match the ROI shape to the target. For an irregular polyhedral ROI, the values of $x'_{max}(\theta_G)$ and $x'_{min}(\theta_G)$ in Eq. [3.9] are determined using Eq. [3.2]. However, for the regular polyhedral case, including that of a right circular cylinder (noting that such a cylinder is an infinite order regular polyhedron), these projections can be determined at any angle θ_G from the center-co-ordinates (r_o, θ_o) and the diameter d (twice

the length of the perpendicular from the ROI center to its side) of such ROIs, viz.

$$x'_{max}(\theta_G) = r_o \cos(\theta_G - \theta_o) + 0.5\, d\,, \qquad [3.11a]$$

$$x'_{min}(\theta_G) = r_o \cos(\theta_G - \theta_o) - 0.5\, d\,. \qquad [3.11b]$$

Note that the extent of the projected ROI remains constant at all angles of rotation θ_G and is equal to the diameter of the ROI itself: $[x'_{max}(\theta_G) - x'_{min}(\theta_G)] = d = \text{constant}$. For the case of a centered, cylindrical ROI, $x'_{max}(\theta_G) = -x'_{min}(\theta_G) = 0.5d$, and the rf pulse shape given by Eq. [3.10] reduces to the following form:

$$B_1(t) = C \cos(2\pi K G_r (D + d) t) \operatorname{sinc}(2\pi K G_r (D - d) t)\,, \qquad [3.12]$$

where C scales the rf tip-angle and $K = \gamma/8\pi$. This is the cossinc rf waveform derived in the previous chapter to localize a single, centered, cylindrical ROI.

In a similar way, any multiple ROI profile P_M can be decomposed into a sum of several non-overlapping RECT functions and the corresponding B_1 pulse shapes can be determined using the Fourier shift theorem as above. In general, the rf pulse shape will be of the form:

$$B_1(t, \theta_G) = \sum_j \operatorname{sinc}(\pi\, \Delta\nu_j(\theta_G)\, t) \exp(i\, 2\pi\, \nu_j(\theta_G)\, t)\,, \qquad [3.13]$$

where $\Delta\nu_j(\theta_G)$ and $\nu_j(\theta_G)$ are the width and the center-offset of the j^{th} RECT function in the sum at the angle θ_G. Therefore, B_1 pulse shapes for Projection Presaturation can be obtained either analytically, using Eq. [3.13], or numerically, by evaluating Eq. [3.7] using the discrete Fourier transform.

3.3 *Method*

The accuracy of the extended Projection Presaturation method described in the

previous section for localizing polyhedral ROIs has been tested on a phantom, a hollow cylinder of inner diameter 60 mm and length 70 mm filled with water doped with copper sulphate to a T_1 of about 1 sec and T_2 of 400 ms. To localize a single ROI, Eq. [3.10] was used to determine the B_1 waveform. Similarly, Eq. [3.13] was used to derive the B_1 pulse shape to localize multiple ROIs. The individual frequency-offset sinc pulses composing the B_1 waveform at a given gradient angle, θ_G, were applied sequentially. The sinc waveform was truncated after four zero-crossings. The appropriate bandwidth of each sinc pulse at each angle θ_G was achieved by adjusting the pulse duration at that angle. The individual sinc pulse durations used in the experiments were in the range 0.57 - 1.787 ms. The rf power of each sinc pulse was scaled to a tip-angle of approximately 30°. The amplitude G_r of the rotating gradient (solid lines in Fig. 3.1) was 4 mT/m unless otherwise stated in the text, and that of spoiler gradients (dashed lines in Fig. 3.1) was 9 mT/m which was adequate to dephase the existing transverse magnetization after the application of the rf sub-pulses at each angle in 0.8 ms. A conventional spin warp imaging sequence was used following the localization sequence to image a transverse slice (x-y plane) of the phantom. All the imaging parameters were the same as before except that the field of view (FOV) was 75 mm unless otherwise specified in the text.

The rf pulses were applied at 36 gradient rotation steps to suppress the outer signal adequately. To localize high order ROIs (cylinder and ellipse), these gradient steps were chosen at equal angular intervals (10°) over one complete cycle (0 - 360°) of the rotating gradient. For localizing a square ROI, however, the 36 gradient steps were

selected only in orthogonal directions (*e.g.* 0° and 90°) to the sides of this ROI and the saturation rf pulses were repeated alternately at these angles.

The procedure described above, ideally, leaves the ROI unperturbed during localization; however, some excitation of, and therefore signal loss from, the localized ROIs is inevitable. Primarily, there are two sources of signal loss. First, gradient-induced eddy currents, and second, rf waveform truncation, as described in chapter 2, which causes unwanted side lobes and finite transition regions in the rf profiles, both of which extend into the ROIs. In order to measure the signal loss from the localized ROIs, as mentioned above, I define signal loss parameters SL_{eddy}, and SL_{rf} corresponding to signal losses caused by eddy currents and the rf, respectively, as follows:

$$SL_{eddy} \equiv [I^N - I^G]/I^N, \qquad [3.14a]$$

$$SL_{rf} \equiv SL_{total} - SL_{eddy}, \qquad [3.14b]$$

where the total signal loss, SL_{total}, is expressed as

$$SL_{total} \equiv [I^N - I^{ROI}]/I^N. \qquad [3.14c]$$

In Eq. [3.14], I^N is the average pixel intensity, in the normal image of the object, of the region corresponding to the spot of the ROI being localized (with average noise subtracted out from it); I^G is the average pixel intensity of the same spot, as above, in the image of the same object, obtained by first turning on only the gradients of the Projection Presaturation localization sequence used to localize the ROI in the object, followed by a conventional spin-warp imaging sequence. The I^{ROI} in Eq. [3.14c] has the same meaning, as already defined in Eq. [2.12], chapter 2.

The localization procedure, described above, provided the images of the localized

ROIs. These images, in combination with a spin-warp image of the same phantom (without Projection Presaturation), were then used to estimate SL_{total}. The procedure for estimating SL_{eddy} in each case of ROI localization involved spin-warp imaging of the phantom, using the same imaging parameters, except this time only the gradients (but not the saturation rf) of the localization sequence of Fig. 3.1 were turned on prior to the imaging sequence. The delay between the end of the localization sequence, used to localize the different ROIs, and beginning of the imaging sequence was 200 μs. The SL_{rf} was then calculated using Eq. [3.14b], once SL_{total} and SL_{eddy} were estimated.

3.4 *Experimental Results*

3.4.1 *Localized High Order ROIs*

Figure 3.4a shows an image of the phantom, demonstrating localization of a single, cylindrical, off-center ROI with its axis orthogonal to the transverse plane. The desired ROI had a diameter of d = 12 mm and center of (r_o = 15 mm, θ_o = 45°). The amplitude of the rotating gradient was G_r = 3 mT/m. The diameter (full width at 10% maximum of the ROI profile) and the position of the ROI in the image agree well (within 1%) with the desired values mentioned above. The measured suppression quality SQ_{expt} exceeded 99%. This is equivalent to that achieved for on-center localization of a single, cylindrical ROI. This result demonstrates that the technique for off-center localization is as accurate as the on-center case.

The feasibility of the technique to simultaneously localize two cylindrical ROIs

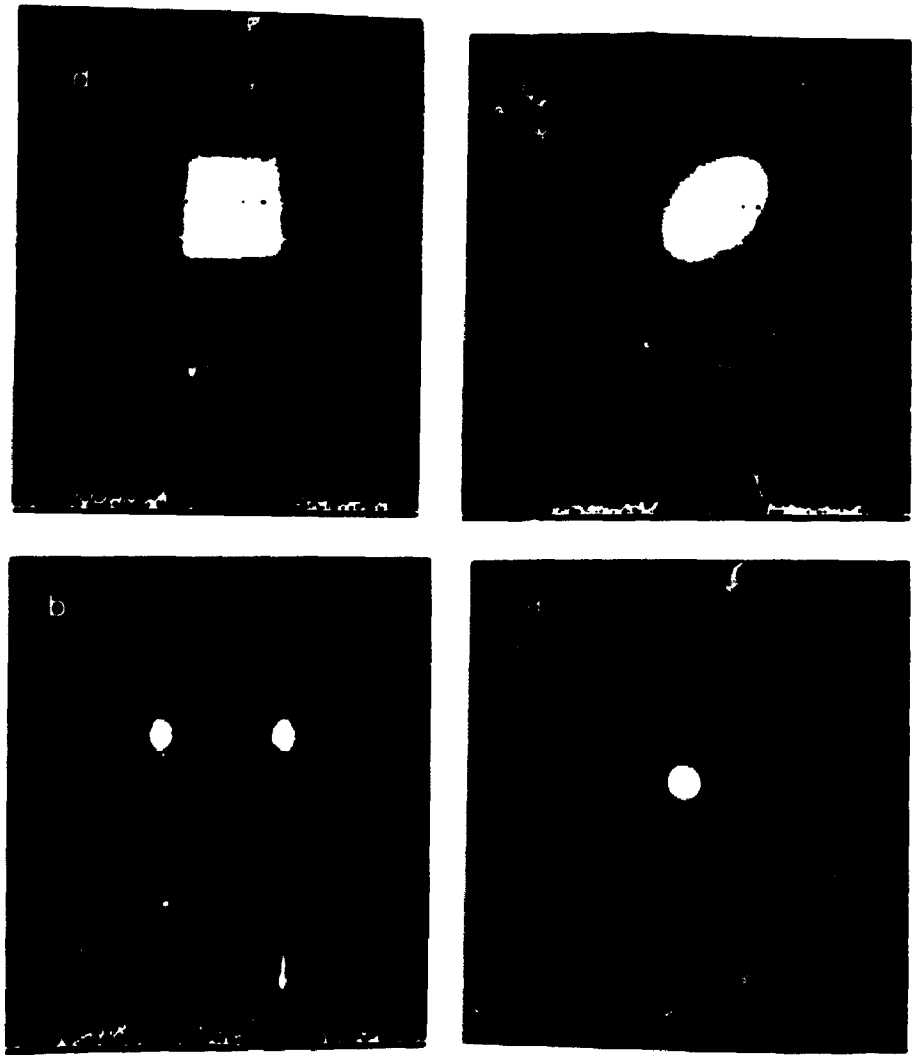

FIG. 3.4. Magnitude images and profiles of the phantom demonstrating the localization of (a) a single, cylindrical ROI of diameter 12 mm, centered at r_o = 15 mm, θ_o = 45°, (b) two cylindrical ROIs, each of diameter 10 mm, centered at $r_o^{(1)}$ = 18 mm, $\theta_o^{(1)}$ = 0°, and $r_o^{(2)}$ = 18 mm, $\theta_o^{(2)}$ = 180°, (c) a centered, elliptical ROI of major:minor axis = 3:2 with the 4 cm major axis inclined at 45° from the horizontal, and (d) a centered, square-piped ROI of side 2.4 cm. The "+" indicates the on-center position. A "zipper" (central horizontal line) in the images is a hardware artifact (an rf leak in the transmitter-receiver circuitry, causing a dc component in the images) and is not a characteristic of the localization technique. 36 30° tip angle rf pulses were used at 36 gradient steps to localize the ROIs of Figs. a-d.

of desired diameter ($d^{(1)} = d^{(2)} = 10$ mm) centered at ($r_o^{(1)} = 18$ mm, $\theta_o^{(1)} = 0^o$) and ($r_o^{(2)} = 18$ mm, $\theta_o^{(2)} = 180^o$), respectively is demonstrated by the image of the phantom shown in Fig. 3.4b. Again measurements of the diameters and the locations of the isolated ROIs in the image are in excellent agreement (within 1%) with the desired values. The measured SQ_{expt} exceeded 99%, demonstrating that the technique is robust even for localization of multiple ROIs.

Localization of an elliptical target (a cylinder of elliptical cross-section) is shown in Fig. 3.4c. An irregular polygon (ROI) of 32 vertices, chosen at equal angular intervals around the perimeter of a desired centered elliptical target, was used to approximate the ROI shape to the elliptical target. The ratio of major to minor axis of the desired ellipse was 3 : 2 with the 4 cm major axis inclined at 45° from the horizontal. The measured ROI parameters (size as well as orientation of the ellipse) in the image agreed within 2% of the desired values, demonstrating the ability of the technique to conform a ROI shape to the target with a high degree of accuracy. Again a suppression quality of $SQ_{expt} > 99\%$ was achieved, showing the accuracy of outer signal suppression.

3.4.2 *Localized Lower Order ROI*

An example of lower order ROI isolation is shown in Fig. 3.4d: the desired ROI was a cylinder of square cross-section of side 2.4 cm. For suppressing the outer signal adequately, 36 pairs of frequency-offset sinc rf pulses but only two gradient angles (0° and 90°) were used. As is clear from Fig. 3.4d, this low order ROI has sharp edges and

corners which might not have been achieved had the directions of the rf application not been chosen orthogonal to the sides of the ROI. This experiment demonstrates that Projection Presaturation can also be used to localize low order ROIs, such as the more conventional cuboidal/squarepiped ROIs.

3.4.3 *Signal Loss from the ROIs*

A standard spin-warp image and image intensity profile through the diameter of the phantom is shown in Fig. 3.5a. The image intensity profile through the horizontal diameter of the phantom in Fig. 3.5b shows the effect of eddy currents alone on the signal loss. This image was obtained by first turning on only the gradients of the sequence of Fig. 3.1, used for localizing an elliptical ROI of Fig. 3.4c, followed by a spin warp imaging. In Fig. 3.5c, the profile through the localized image of the elliptical ROI (same image as in Fig. 3.4c) shows the combined effect of eddy currents and the rf imperfections on the signal loss. The SL_{eddy} , SL_{total} and the SL_{rf} , corresponding to Fig. 3.5, are shown in table 1. A similar analysis of SL_{eddy}, SL_{total}, and SL_{rf} carried out for the remaining ROIs of Fig. 3.4 is also shown in table 1. The SL_{eddy} was the largest (26%) for isolating a square ROI, whereas the SL_{rf} was found to be the largest (24%) for the single, off-center ROI of Fig. 3.4a.

3.5 *Discussion*

The localization of the ROI shapes presented above demonstrates that Projection Presaturation can be successfully applied to isolate, both, low and high order polyhedral

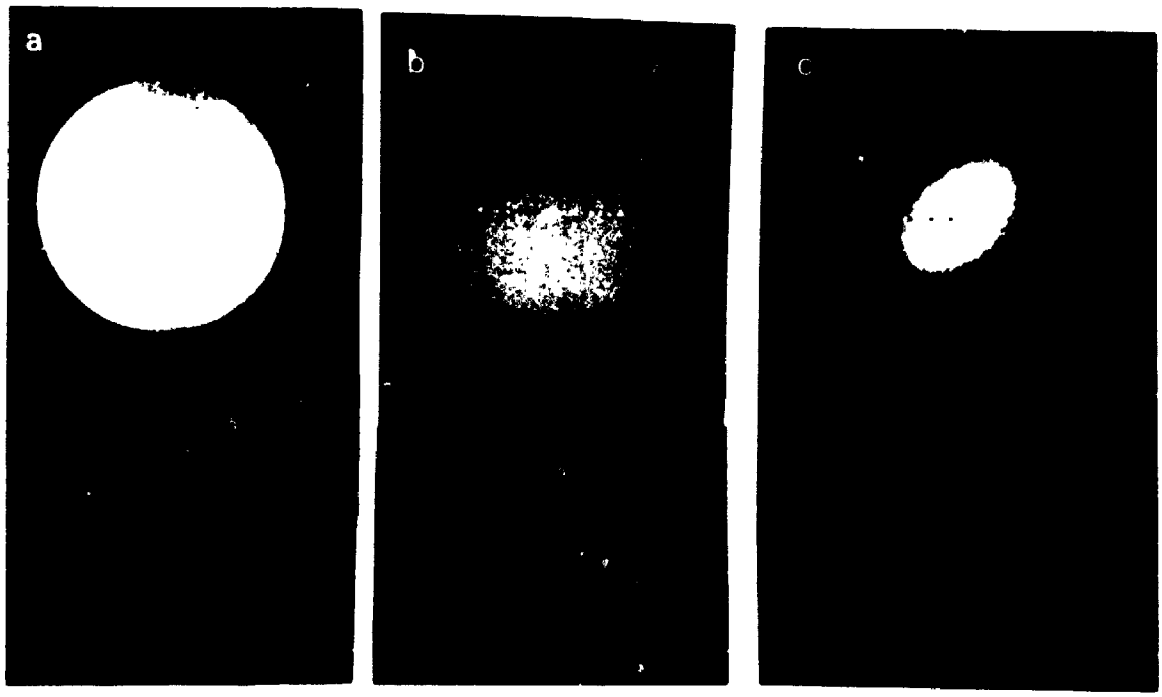

FIG. 3.5. Images and image intensity profiles through the horizontal diameter of the phantom, demonstrating the effect of eddy currents and the rf imperfections on signal loss from the elliptical ROI of Fig. 3.4c: (a) standard spin-warp image and the image profile; (b) image/profile of the same phantom obtained by turning on only the gradients of the localization sequence of Fig. 3.1, used to localize an elliptical ROI, followed by a spin-warp imaging sequence; (c) image/profile through the center of the localized elliptical ROI of Fig. 3.4c (shown again here for comparison). The imaging sequence had a TE of 34 ms and TR of 3s. 36 gradients angles were used in the sequence of Fig. 3.1. The amplitude of the rotating gradient was G_r = 4 mT/m, and that of spoiler gradient was 9 mT/m.

TABLE 1

Signal Loss[a] from the Localized ROIs of Fig. 3.4

	$SL_{eddy}(\%)^b$	$SL_{rf}(\%)^c$	$SL_{total}(\%)^b$
Single, off-center, cylindrical ROI (Fig. 3.4a)	17	24	41
Two cylindrical ROIs (Fig. 3.4b)	20	13	33
Elliptical ROI (Fig. 3.4c)	19	13	32
Square-piped ROI (Fig. 3.4d)	26	15	41

a All measurements have an estimated error of less than 10%.
b Measured as described
c Calculated by Eq. [3.14b]

ROIs, whose shape, size, number and location can be chosen arbitrarily. Using this technique, irregular *in vivo* targets can be accurately localized by choosing an appropriate set of points $\{(r_i, \theta_i)\}$ with the only requirement being that these points, when connected sequentially, must bound a convex shape. Most biological targets (organs) are of convex shape; however, the extention of the Projection Presaturation to permit localization of concave shapes would be desirable.

Application of this technique to localize multiple targets simultaneously requires careful implementation. For any arrangement of the targets within a 3D volume, a few projection angles exist at which the projections of two ROIs are separated by a narrow gap. To saturate these narrow band regions in the projection profiles practically requires sinc pulses of relatively long duration, whose use in the localization sequence will increase the total localization time inordinately. Such situations can be handled in several ways: 1) excite these narrow band regions separately by using shorter sinc pulses in the presence of a gradient of increased strength or 2) not apply the narrow band sinc pulses at all over the range of angles within which the gap between two ROIs is below some threshold or 3) not use the gradient angles at all at which the gap between two ROIs is below the threshold and use a suitable combination of the number of gradient steps and the rf tip-angle using Eq. [2.5] to achieve adequate saturation. In this work, the approach 2) was used; however, for a large number of ROIs, approaches 1) and/or 3) may be the preferred ones. In either case, the gradient angles θ_G^{thresh} need to be known at which the width of the rectangular profile between two ROIs, i and j, in the single multiple-ROI profile (see Fig. 3.3) falls below the threshold, $\Delta\nu_{thresh}$, *i.e.*, when

$$\left| \gamma/2\pi \, G_r \, [x'_{min}{}^{(i)}(\theta_G{}^{thresh}) - x'_{max}{}^{(j)}(\theta_G{}^{thresh})] \right| < \Delta\nu_{thresh}. \quad [3.15a]$$

From a knowledge of the set of ROIs projections calculated at equal angular intervals over 0 - 2π rotation of the gradient, a set of gradient angles $\theta_G{}^{thresh}$ satisfying Eq. [3.15a] can be known. Approach 3) requires a further knowledge of the total number, n^{rej}, of the gradient angles *rej*ected which simply will be equal to the total number of $\theta_G{}^{thresh}$. The actual number of gradient angles allowed, n', in a total of n^{total} can then be known using $n' = n^{total} - n^{rej}$ which, in turn, can be used to find an appropriate rf tip-angle θ' using Eq. [2.3] via

$$\theta' = \cos^{-1}[\{1 - SQ_{th}\}^{(1/n')}] \quad [3.15b]$$

to be used for all the rf pulses applied at n' gradient steps to achieve adequate SQ_{th}.

Although, Projection Presaturation is designed to leave the ROI magnetization untouched, the ROI signal is, as might be expected, not totally unaffected. The signal loss, SL_{eddy}, was found to be the largest for localizing the square ROI. Probably, this resulted from the fact that the square ROI required x and y gradients to be abruptly turned on/off alternately, causing the largest gradient change (9 mT/m), and hence, the strongest eddy currents on our uncompensated gradient system. Allowing an eddy current settling time (~ 35 ms on our system) between the Projection Presaturation and the spin-warp imaging sequence reduced signal loss substantially at the expense of a degraded SQ (SQ < 99%) because of T_1 recovery of the outer volume magnetization. This challenge of T_1 recovery during the eddy current settling time can be met (and has been met -- see chapter 4 and the Appendix) by using a non-selective 180° rf pulse that is alternately turned on/off in front of the Projection-Presaturation and using a data

subtraction cycle (*20,23,34,35*). In any case, this signal loss due to eddy currents will be system-dependent, and on a system with shielded or accurately compensated gradients, it is expected to be far less. As with other localization techniques, successful application of the Projection-Presaturation to *in vivo* localized spectroscopy may require some procedure for correcting the distortions in the spectra caused by eddy currents. Klose (*42*) has recently reported a correction method for *in vivo* proton spectroscopy in the presence of eddy currents.

The signal loss due to rf imperfections alone was quite significant. In particular, the SL_{rf} quantified from the single, off-center, cylindrical ROI of diameter 12 mm, as shown in Fig. 3.4a, was the largest. This resulted from the fact that the rf profile, for a given shape of the rf pulse (a sinc with four zero-crossings in this study), would have the widest transition regions in this case. The rf-induced signal loss could have been reduced to an insignificant level had the windowed sinc with more zero crossings been used. However, this could not be achieved because a sinc with six or more zero-crossings could not produce a rf tip-angle of even 30° (without increasing the rf duration, which is undesirable), given the maximum rf power available on our system.

The signal loss SL_{rf} (see Eq. [3.14b]) measured from the localized ROIs of Fig. 3.4 was expected and was in good agreement with the theoretical estimate of the SL_{rf}, as given by Eqs. [2.8] and [2.9]. For example, in the case of a square ROI of Fig. 3.4(d), the fractional average signal magnitude within the ROI, i.e. p in Eq. [2.8], in the single profile of two frequency-offset sinc pulses (see Fig. 3.6), each truncated after four

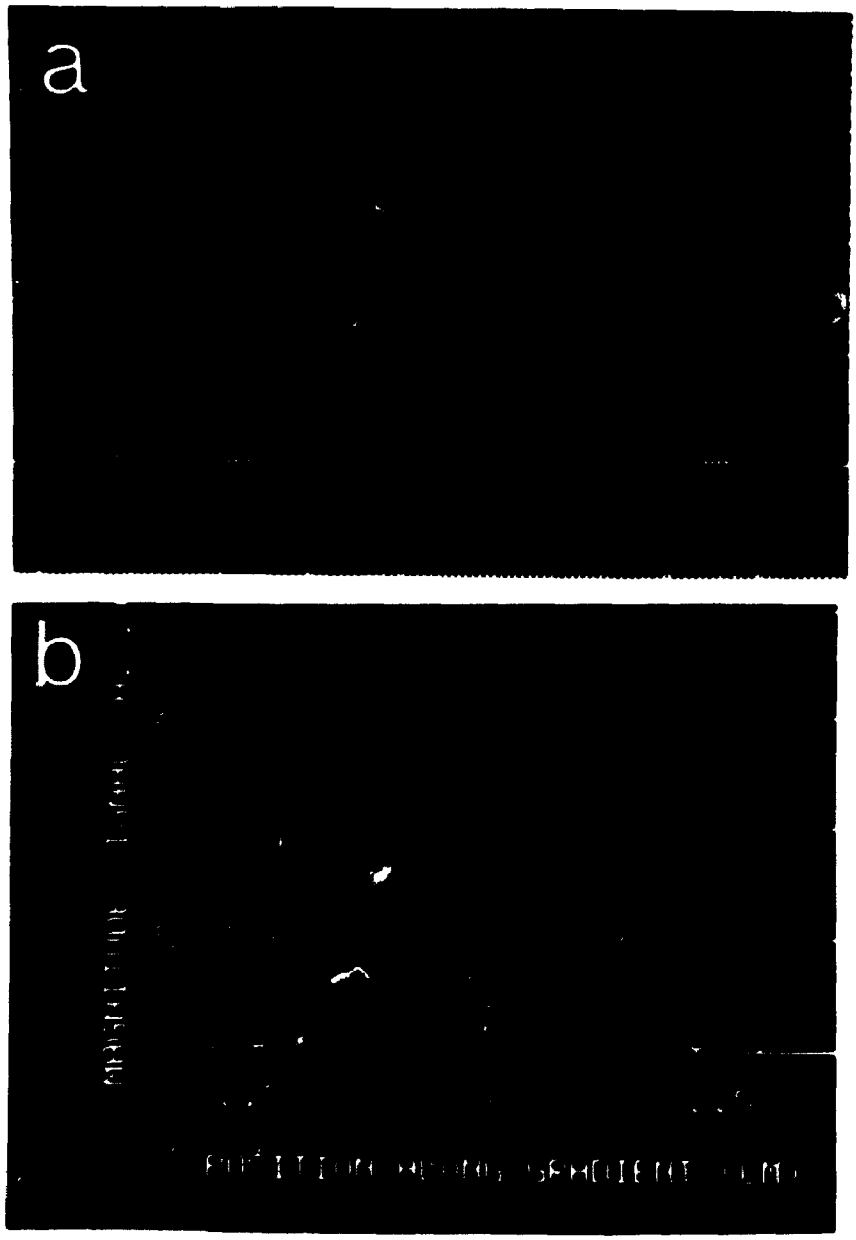

FIG. 3.6. Theoretical and the experimental profiles of a pair of frequency-offset rf sinc pulses (each truncated after four zero-crossings) used to localize the ROI of Fig. 3.4(d): (a) theoretical profile (Fourier transform of the rf waveform, as described above) - the mean signal magnitude within the ROI is about 18% of that in the outer region, i.e. p = 18 in Eq. [2.8]; (b) experimental profile of the same rf pulse corresponding to a tip-angle of ~ 30°. In this case, the value of p ≈ 18 agrees with the one in Fig. (a). The unequal signal magnitude in the outer region in Fig. (b) is possibly a consequence of the rf hardware in successive rf transmission of the two frequency-offset sinc pulses. The spatial modulation of the signal in the ROI of Fig. (b) along gradient direction arises possibly from the interference of the excitations produced by the side lobes in the profiles of the two truncated sinc rf waveforms.

zero-crossings, was about 18%. For an rf tip-angle of $\theta = 30^{\circ}$, n = 36, used to localize the square ROI of Fig. 3.4(d), the p = 18% (constant for all the rf profiles in this case) will cause the SL_{rf} = 13.6%, as estimated by Eqs. [2.8] and [2.9]. This is in close agreement (within 10%) with the measured SL_{rf} = 15% from the same ROI (Fig. 3.4d). In a similar way, Eq. [2.10] can be used to estimate the SL_{rf} against the measured values of the same from the remaining ROIs of Fig. 3.4, in which case 36 different p values from the same number of rf profiles have to be known. Thus, Eqs. [2.8] - [2.10] succeeded in estimating the SL_{rf} for chosen shapes of the rf pulse, and hence will serve as guidelines for minimizing this loss by reducing p.

In Projection Presaturation, the rf truncation effect (transition regions in the rf profile) remains the real and the global source of signal loss (assuming that the system-dependent signal loss due to eddy currents is minimized or eliminated using the approach as described previously). In reality, although this effect can not be eliminated, it can be minimized. To reduce the effect of finite transition regions (in rf profiles), which for a given shape of rf pulse scale with the size of tne exterior volume, the rf profile "edge sharpening" scheme introduced by Singh et al. (*29*), Haase (*20*), and Crawley et al. (*23*), can be used (and has been used in the Appendix for localized relaxometry). According to this scheme, the transition regions in the rf profiles are forced to be narrow in the immediate vicinity of a ROI, even when exciting/presaturating a large exterior volume, and results in a decreased signal loss from the ROI. Because the theoretical and experimental detail of the "edge sharpening" scheme will be presented in the Appendix, no more will be presented here.

Recently, some new developments by Rim et al. (*43*) and De Crespigny et al. (*44*) have been reported in the literature for localizing a single, on-center, cylindrical ROI using rotating gradients. Projection-Presaturation differs from these techniques in that it does not require any special gradient hardware (*43*) and because, it is based on selective presaturation, T_2- or T_2^*- independent data can be acquired from simultaneously localized multiple ROIs. Further, Projection Presaturation uses saturation rf pulses, whose frequency spectrum is uniform, as opposed to the technique (*43*), which uses noise modulated rf pulse of non-uniform spectrum. For uniform excitation and spatial presaturation leading to minimal signal contamination of the ROI signal from outside, the outer region should be uniformly excited which will be better achieved by using a rf pulse of uniform frequency spectrum.

In summary, Projection Presaturation has been found to be an accurate single-shot localization technique for isolating one or more off-center polyhedral ROIs, whose shape and size can be tailored to match *in vivo* targets. Analytical methods to design the saturation rf pulses to isolate these irregular ROIs have been described, and the shortcomings of the actual rf and gradients used on a particular instrument identified and quantified. The technique is robust (SQ_{expt} > 99%), even for off-center ROI and multiple ROI localization, although some signal loss, whose causes are identified, is inevitable. Because of its robustness and simplicity, the method has several applications, which will be demonstrated in the subsequent chapters.

CHAPTER 4

Applications of Projection Presaturation to Imaging and Spectroscopy

4.1 *Introduction*

The Projection Presaturation method described in the previous chapters has many applications in MR imaging, localized spectroscopy/relaxometry, and other areas of MR. In this chapter, I demonstrate applications of the technique to imaging and localized spectroscopy. The next chapter applies the method to acquiring relaxation data from an accurately localized volume (localized relaxometry).

4.2 *Applications to Imaging*

The diagnostic quality of conventional MR images is usually less than the optimal because of unavoidable factors, which cause image artifacts. Projection Presaturation can be used to improve MR image quality by suppressing certain image artifacts. For example, here, I demonstrate 1) suppressing "aliasing" when imaging a reduced FOV, and 2) suppressing flow artifacts.

4.2.1 *Small FOV Imaging*

Volume selective excitation techniques have applications in "zoom imaging": a method of imaging in which in-plane resolution is increased by restricting the image FOV. The consequence of a restricted FOV within an extended object is the fold-over

("aliasing") of the region outside the FOV onto the image-plane, thus obscuring details in the image. As a result, the phenomenon of aliasing limits the extent to which spatial resolution can be increased by exploiting the maximum strength of the frequency- and phase-encoding gradients, available on the current scanners, to image a small FOV. If Projection Presaturation is used to suppress the signal originating from outside the restricted FOV, high-resolution images are obtained with no aliasing artifact. This is demonstrated on a phantom described below.

The phantom consisted of three co-axial cylinders of diameters 60, 10, and 1 mm, filled with water doped with copper sulphate to a T_1 of 1 s and T_2 of 400 ms. In design, the phantom is analogous to a typical clinical situation, where the ROI (the two innermost cylinders) would be an *in vivo* target surrounded by other tissues (the outermost cylinder). The relaxation times of water have been chosen so as to fall in the range of biologically relevant T_1 and T_2 values. An image of the phantom is shown in Fig. 4.1a: the FOV was 70 mm and the image matrix was 128 x 128. If the FOV is restricted so as to enclose only the two inner cylinders (ROI), aliasing is expected. Figure 4.1b shows the standard image of the phantom when the FOV was restricted to 30 mm (keeping the matrix size the same). Image pixel resolution is increased; however, wrap-around (aliasing) has occurred in the phase encoding direction (horizontally here) and confuses details in the image. In Fig. 4.1c the aliasing artifact of Fig. 4.1b has been eliminated by saturating the region outside a centered cylindrical ROI of diameter 20 mm by the Projection Presaturation localization sequence of Fig. 3.1. In the sequence, a pair of frequency-offset sinc pulses, each of tip-angle 30°, was repeated at 36 equal angular

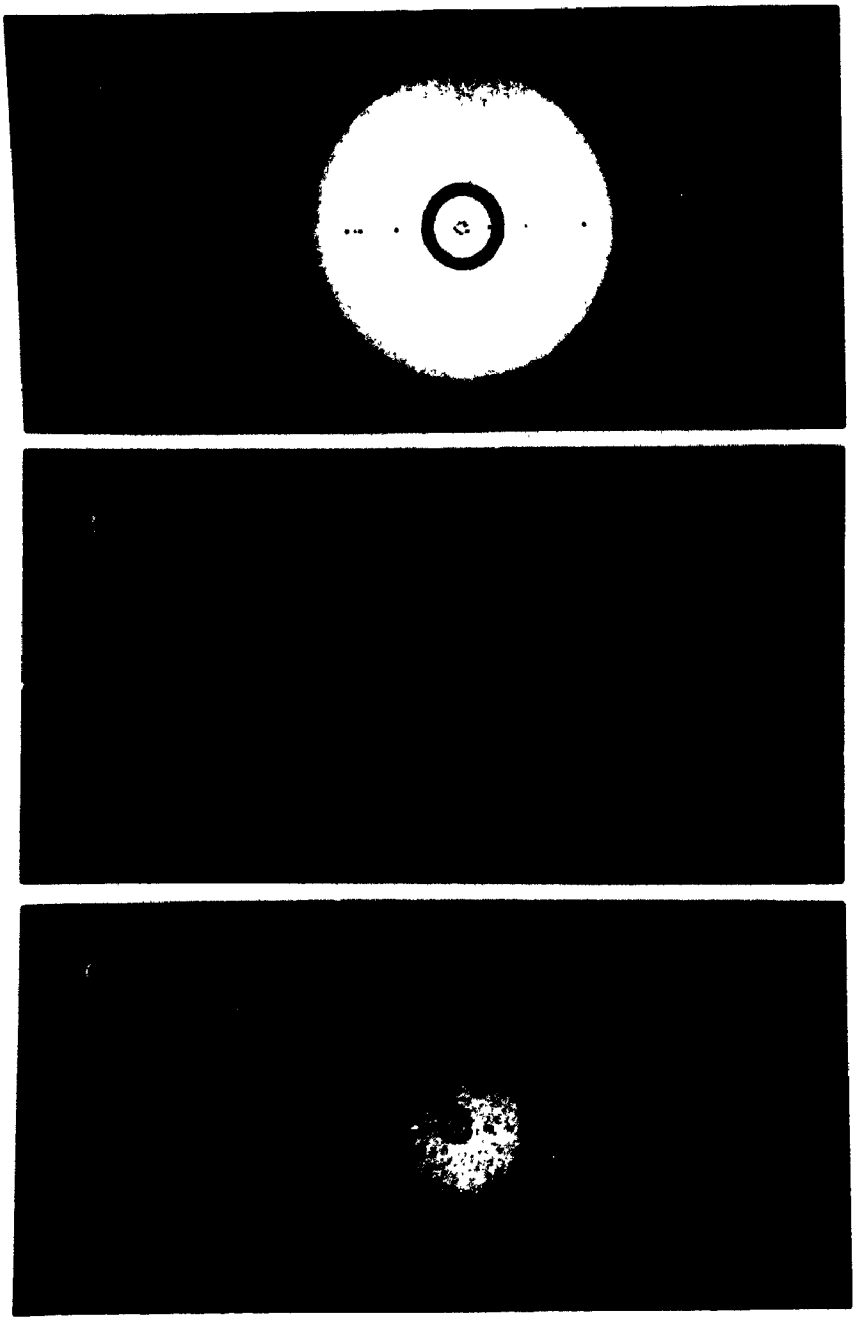

FIG. 4.1. Transverse-slice images of a phantom consisting of three co-axial cylinders of doped water of diameters 60, 10 and 1 mm: (a) standard image of FOV of 70 mm and matrix size of 128 x 128; (b) image exhibiting the aliasing artifact when the FOV was restricted to 30 mm, keeping the matrix size the same; (c) resultant image in which the aliasing artifact of Fig. b has been suppressed by presaturating the volume outside a centered, cylindrical ROI of diameter 20 mm. In the Projection Presaturation sequence of Fig. 3.1, a pair of frequency-offset sinc pulses, each of tip-angle 30°, was repeated at 36 equal angular intervals over one complete cycle of the rotating gradient.

intervals over one complete cycle of the rotating gradient. This experiment shows that the technique can be combined with fast imaging sequences, such as echo-planar imaging (*45*), to image a restricted FOV without introducing an aliasing artifact.

4.2.2 *Suppression of Flow Artifacts*

In clinical MR imaging, the diagnostic quality of examinations is often reduced by a variety of artifacts resulting from physiologic motion (*e.g.* cardiac, respiratory, cerebrospinal fluid motion etc.) and the pulsatile blood flow caused by the beating heart. Gating and other techniques have been useful to reduce motion artifacts, but even when cardiac and respiratory artifacts are absent, MR images are frequently degraded by streaklike artifacts caused by the pulsatile blood flow. In conventional 2DFT imaging, these flow artifacts radiate in the phase-encoding direction from vessels which pass through the image-slice, and thus obscure anatomic detail, and reduce the contrast. In high-resolution, small FOV studies, these artifacts are accentuated even further, thus making the diagnosis difficult. The Projection Presaturation technique can suppress the flow artifacts, as demonstrated below.

To demonstrate suppression of a pulsatile flow artifact, the phantom consisted of three parallel syringes filled with stationary water doped with copper sulphate to a T_1 of 1 sec and T_2 of 400 ms, and two parallel bottom tubes through which a pulsatile flow of water was running. The phantom simulates a common clinical situation, where the three syringes of static water are the objects of interest, that happen to be close to vessels conducting pulsatile flow. Normal imaging results in Fig. 4.2a, in which superimposed

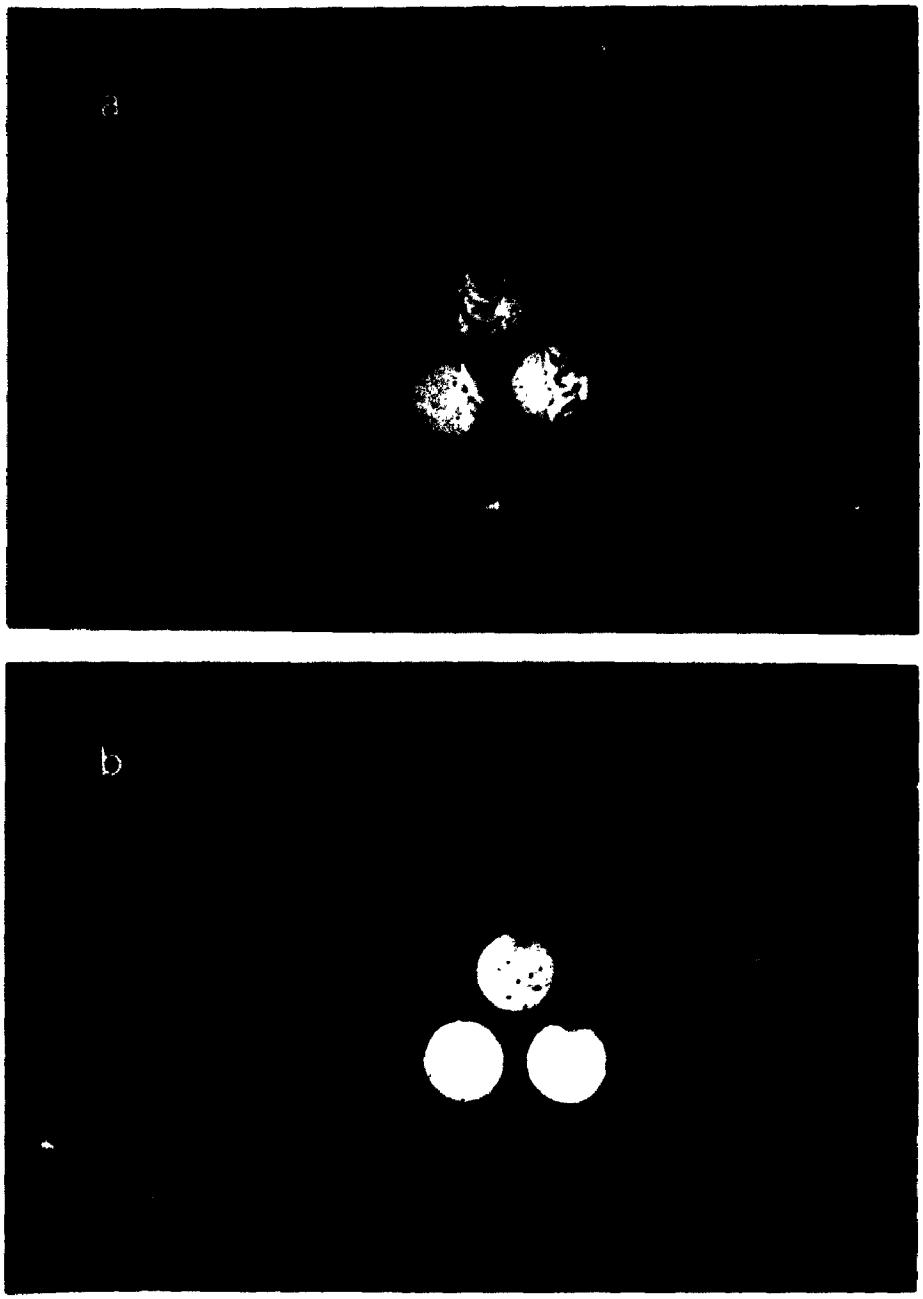

FIG. 4.2. Demonstration of flow artifact suppression by Projection Presaturation in a phantom study: (a) a standard transverse-slice image of the phantom when the pulsatile flow of water was running through the two bottom tubes (circles) into and out of the transverse image plane, causing zipper-like artifacts in the phase-encoding direction (vertically here). The following were the experimental parameters: FOV = 40 mm, TE = 34 ms, TR = 1s, slice thickness = 10 mm, mean flow rate = 6 ml/sec; (b) flow artifact suppressed using the Projection Presaturation technique. Localization sequence parameters were the same as in Fig. 4.1.

on the standard image of the phantom is a zipper-like artifact in the phase-encoding direction (vertically). By Projection Presaturation, the region outside a centered cylindrical region (ROI) which enclosed the top three circles (syringes) was saturated, thus eliminating signal from the region containing the flowing water. As shown in Fig. 4.2b, this suppressed the flow artifact completely. This experiment demonstrates quite clearly the utility of the technique to improve MR image quality in the presence of flow.

4.3 *Application to Localized Spectroscopy*

Numerous *in vivo* studies indicate that high-resolution MR localized spectroscopy can provide biochemical information from selected tissue regions without requiring any injection of contrast material in the body (*3,4*). In order that the information acquired from *in vivo* targets be medically reliable, the targets must be accurately localized, with a minimum of signal contamination from the surrounding tissues. In this work, the efficacy of the Projection Presaturation to acquire ^1H spectra from an accurately localized region (localized spectroscopy) is demonstrated in a phantom.

The phantom consisted of five tubes, as shown in Fig. 4.3a, with the central tube filled with absolute methanol. The other four tubes contained water doped with copper sulphate to a T_1 of 750 ms and T_2 of 250 ms. The spectrum acquired from the phantom (without localization) is shown in Fig. 4.3b: water peak lies between two methanol peaks. The objective of this experiment is to acquire methanol resonances from the methanol tube after suppressing the water resonance originating from the surrounding water tubes.

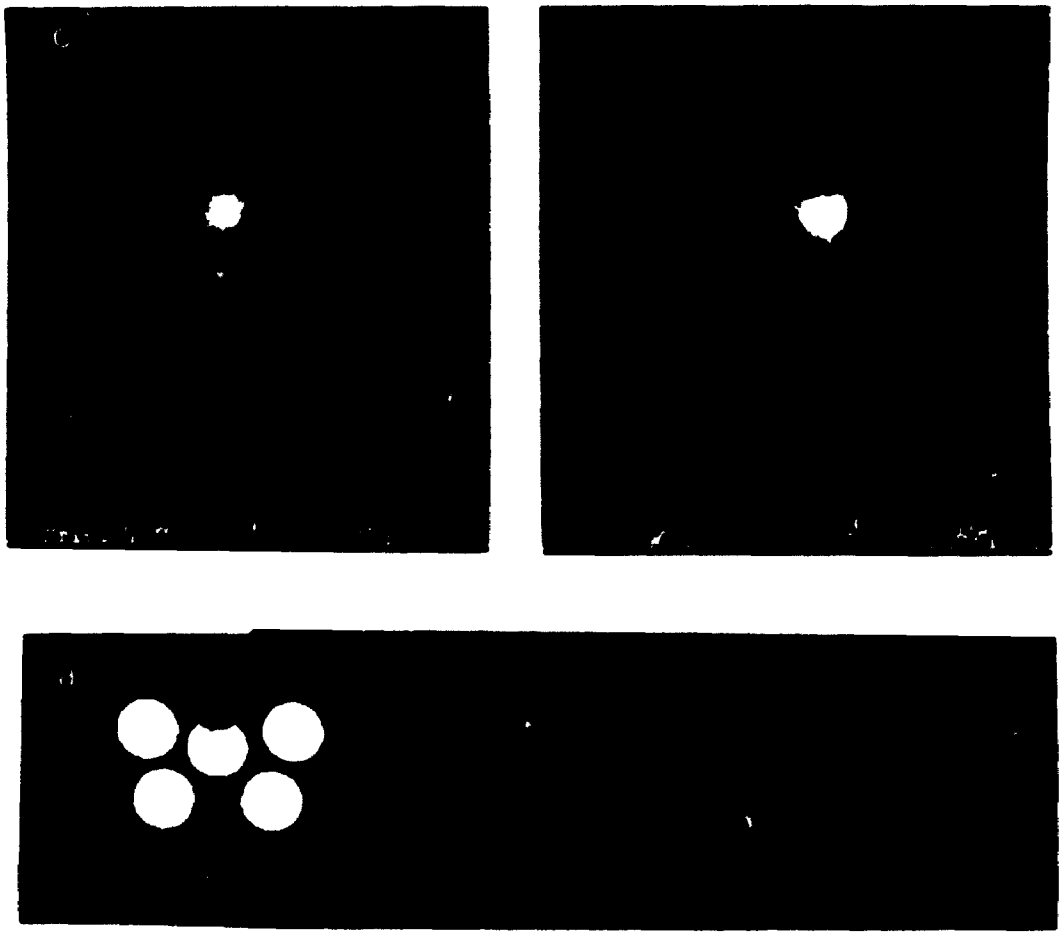

Fig. 4.3 Images and spectra obtained from the water + methanol phantom: (a) a transverse section of the phantom of five tubes (a central methanol tube surrounded by four water tubes); (b) spectrum from the phantom (the water peak lies between two methanol peaks); (c) a localized image of a cylindrical ROI of diameter 10 mm isolated within the methanol tube (the central tube in Fig. 4.3a) by presaturating the water signal: a SQ_{expt} of better than 99.9% is achieved with 24 gradient angles and pairs of frequency-offset sinc rf pulses (each pulse of duration 0.4 ms and tip-angle ~ 45°); (d) phantom image and a central intensity profile showing the partial recovery of the water magnetization in the waiting time (35 ms).

Figure 4.3c shows the localized image of the methanol tube (ROI) after presaturating the surrounding water tubes. The standard 2DFT imaging sequence followed immediately after the Projection Presaturation localization sequence (Fig. 3.1) to image the localized ROI. The outer volume was suppressed better than 99.9% by using 24 gradient angles and pairs of frequency-offset sinc rf pulses, each pulse of duration 0.4 ms and tip-angle ~ 45°, thus localizing a cylindrical ROI of diameter 10 mm at the center (within the methanol tube). The amplitude of the rotating gradient (solid lines in Fig. 3.1) was 9 mT/m, which was adequate to dephase the existing transverse magnetization in ~ 0.7 ms after each excitation. Spoiler gradients (dashed lines in Fig. 3.1) were not needed for this particular study.

Because of eddy current problems caused by the switching of the gradients in the localization sequence, a non-selective 90° read pulse was applied 35 ms (eddy current settling time for the imager used) after the localization sequence to acquire spectral data from the localized ROI. A waiting period of 35 ms resulted in a partial recovery of the longitudinal magnetization of the saturated water spins, leading to unwanted signal contamination of the ROI signal from outside. The effect of the waiting period (35 ms) on the magnetization of water is shown in the image of Fig. 4.3d: partial recovery of the magnetization of the saturated water spins of Fig. 4.3c occurs. The phantom image of Fig. 4.3d was obtained by applying the usual 2DFT imaging sequence 35 ms after the localization sequence of Fig. 3.1.

The effect of longitudinal recovery of the outer volume magnetization (during 35 ms waiting time) on the ROI spectral data was successfully eliminated by turning a non-

selective 180° rf pulse on/off in front of the Projection Presaturation sequence of Fig. 3.1, as shown in Fig. 4.4, and subtracting the two FIDs (*20,34,35*). Because the recovery of the outer volume magnetization is the same in both cases, the outer volume signals cancel out on data subtraction; whereas the ROI signals are of opposite sign and add up. As shown in Fig. 4.5, the localized spectrum (obtained after Fourier transforming the difference FID) from the methanol (ROI) is in accordance with (*e.g.* has the same frequency shifts as) the spectrum of pure methanol, although the peaks are somewhat broadened because of the residual eddy currents.

The result obtained above shows the potential usefulness of the Projection Presaturation for localized proton spectroscopy. The technique should also be well suited for short T_2 species (*e.g.* ^{31}P) because of ROI magnetization left unperturbed during localization.

4.4 *Discussion*

In this chapter, some applications of Projection Presaturation were demonstrated in imaging and localized spectroscopy. Phantom studies demonstrated the effectiveness of the method in eliminating the aliasing artifact or fold-over, thereby increasing the resolution of the image via small FOV imaging. Similarly, the efficacy of the method for eliminating flow artifacts was demonstrated. In localized spectroscopy, methanol proton spectra were acquired from an accurately localized volume which had the same peak locations as pure methanol spectra, although a slight broadening of the peaks was observed arising from the hardware imperfections.

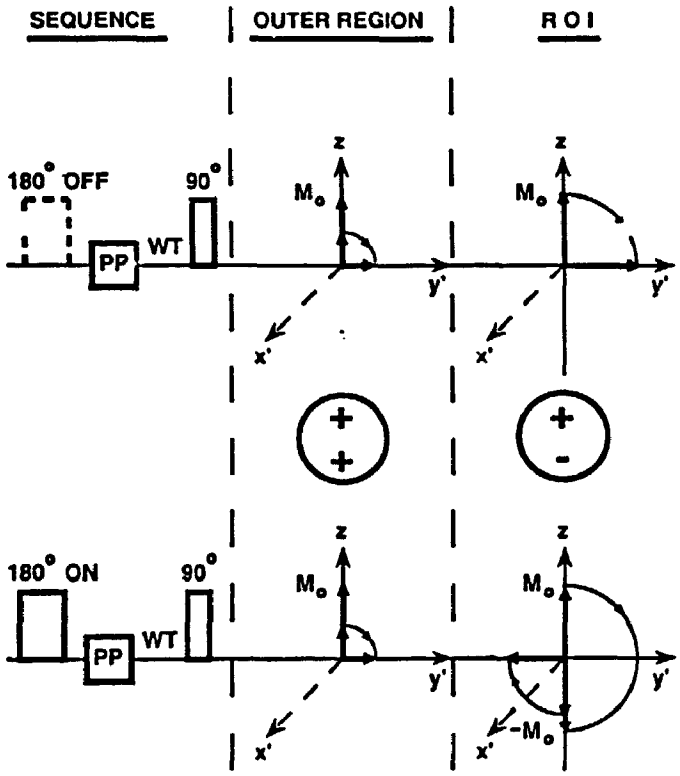

FIG. 4.4. A scheme for eliminating the effect of recovery of the longitudinal water magnetization, as observed in Fig. 4.3d, on the ROI data. Two runs are performed to eliminate this effect, one, without (top row), and the other, with (bottom row), a non-selective 180° rf pulse: the Projection Presaturation (PP) sequence, ideally, sets the magnetization of the outer region to zero in both runs; thus, in the "WT" time following the PP sequence, identical recovery of the magnetization of the outer region occurs; at the same time the ROI magnetization will be positive in the first run (top row), but negative and smaller in magnitude (because of partial longitudinal recovery in "WT" time) in the second run. On subtracting the acquisitions (FIDs) of these two runs, the signals of outer region cancel out, whereas those of the ROI add up.

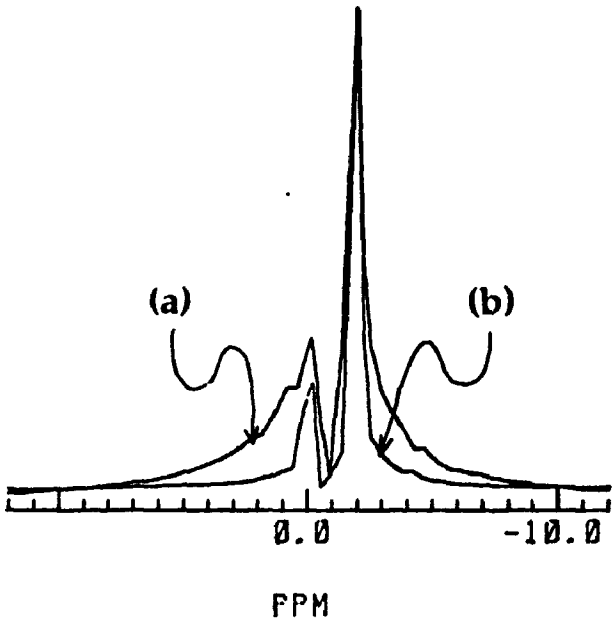

FIG. 4.5. The localized and the pure methanol spectra shown together: (a) a localized spectrum obtained after Fourier transforming the difference of the two acquisitions (FIDs) obtained by the two runs of Fig. 4.4; (b) the pure spectrum obtained after Fourier transforming a single FID acquired from the pure methanol. Both spectra are similar, although the peaks of the localized spectrum are slightly broadened because of the residual eddy currents.

In the past, localization methods have been used to suppress aliasing (*9,46*) and flow (*46*) artifacts. For example, in the case of flow artifact suppression, the method of Feinlee et al. (*46*) typically uses 90° or greater tip-angle rf pulses, and conventionally in one (or atmost three orthogonal) direction(s), to saturate slabs of volumes adjacent to the imaging slice. Because of the tip-angle errors, the flowing spins passing through these slabs remain partially unsaturated. As a result, the flow artifact, although greatly reduced, is not completely eliminated. Because of the same tip-angle error problem, and the requirement of high rf homogeneity, the aliasing artifact is not completely suppressed either (*9,46*).

Projection Presaturation does not suffer from the tip-angle errors, and as such aliasing-/flow-artifacts suppression is more accurate, as shown here. The method can be used to saturate the spins flowing into the image slice, as demonstrated here. Moreover, in a three-dimensional rotating gradient scheme, the technique can be used to saturate the spins flowing from any direction into the image plane, a situation which is commonly met in clinical MRI. The technique can also be used for conventional out-of-plane saturation. Appropriately thick saturation slabs can be saturated so that even fast spins flowing through these slabs remain suppressed. Thus the technique presented can be used as a clinical tool on today's clinical MR scanners to improve the diagnostic value of clinical images by eliminating flow and aliasing artifacts.

Projection Presaturation offers a novel tool to localized spectroscopy where a high degree of sensitivity is required. Though the technique was demonstrated on proton spectroscopy, it should be well suited for determining the chemical concentration of even

short T_2 species, *e.g.* ^{31}P metabolites, from localized region(s). The spectral broadening of localized spectra is a system-dependent problem and on an improved, well compensated gradient system, the broadening is expected to be far less, or even eliminated.

The phantom studies reported in this chapter show that Projection Presaturation can be particularly useful in eliminating certain image artifacts, and in localized spectroscopy. The method can also be applied to perform accurate relaxation time measurements from localized ROIs, and, as such, it may serve as a valuable tool for providing tissue-characteristic information for tissue characterization/discrimination. The use of Projection Presaturation in combination with the techniques of relaxation time measurement in acquiring relaxation data from a localized ROI is the subject of the Appendix.

CHAPTER 5

Discussions and Conclusions

5.1 *Discussions*

In this thesis, a new single-shot spatial localization technique called Projection Presaturation based on selective spatial presaturation has been presented. The analytical methods to design the saturation rf pulses to isolate single or multiple ROIs of desired shape and size by presaturating the region outside such ROIs were described. Experimental results were presented to demonstrate the accuracy of localization by this technique. The technique is robust ($SQ_{expt} > 99.9\%$) even for off-center ROI and multiple ROIs localization. The method proved effective in suppressing flow and aliasing artifacts in MR imaging. And finally, the efficacy of the method to acquire spectral and relaxometric data from accurately localized volume was examined.

Whiie the technique presented in this thesis has several potential applications in MR, there are a few factors which must be carefully considered when using it to achieve accurate spatial localization. First, and the most important factor, is the existing transverse magnetization after the rf application at each gradient rotation angle that must be adequately dephased prior to the next rf application or suppression of signal from the outside region will not be complete. If dephasing is not adequate, the spoiler gradient pulse will phase encode the transverse magnetization after each rf application and cause spatial modulation of the magnetization of the outer volume (*30,47,48*). It was determined experimentally that a spoiler gradient of amplitude 9 mT/m adequately

dephases any existing transverse magnetization in the fraction of a milli second.

Secondly, the presence of chemically shifted species in the outer region may limit the accuracy of definition of the ROI boundary achievable by this method. Therefore, for the application of this technique, particularly to *in vivo* localized spectroscopy/relaxometry, the effects of chemical shift must be properly treated. The difference in the resonant frequency $\Delta\nu$ between two chemically shifted species (*e.g.*, water and fat) will cause a positional shift Δr of each slice on either side of the ROI in the presence of a slice-select gradient by

$$\Delta r = \Delta\nu/(\gamma G_r). \qquad [5.1]$$

In a 2D or 3D rotating gradient scheme, the constant amplitude gradient G_r, for a given $\Delta\nu$, will cause the same positional shift Δr (see Eq. [5.1]) of each of the multi-dimensional slices in respective directions. If the carrier frequency is set on resonance for one of the species, the other species would cause uniform smearing (Δr = constant) of the ROI edges sharpened by the first species on-resonance, leading to poor definition of the ROI boundary and contamination of the ROI signal from outside.

In order to minimize these effects of chemical shift, the value of G_r in Eq. [5.1] must be set such that

$$\Delta r << d. \qquad [5.2]$$

The condition set in Eq. [5.2] will, in general, require a gradient of large amplitude, G_r. In order to cover the excitation of the outer region adequately (noting that the outer region is usually much larger than the ROI), a very short rf pulse, in combination with such (large) G_r, will be required. In a situation where rf power amplifier limitations

have been reached to produce an adequate tip-angle (*e.g.*, 30°) of such a short rf pulse, additional rf pulses, as used in the *edge sharpening* scheme in Appendix, can be used. To acquire ROI data from one species or the other at a time, a chemical shift selective saturation pulse (*49*) can be applied following the Projection Presaturation to saturate the unwanted species. In order to eliminate the effect of recovery of the outer volume magnetization during a chemical shift saturation sequence on the ROI data, a data subtraction scheme, as described and implemented in chapter 4 and Appendix, can be used.

Finally, in this technique the recovery of saturated spins of the unwanted regions due to T_1 relaxation during the localization sequence affects the accuracy of outer volume suppression. To achieve adequate suppression, the total localization time, TL, should be kept as short as possible, while using an optimal localization sequence. For most *in vivo* studies, the TL can be shortened (if needed) to the extent that it is much shorter than the shortest T_1 of outer volume species by using fewer (< 36) gradient angles/rf applications and larger tip-angles ($> 30°$) saturation rf pulses without sacrificing the suppression quality (see Eq. [2.3]). The use of an rf tip-angle greater than 30° extends beyond the small-tip-angle regime in the sense that the solutions of Bloch equations are no longer linear (*36*) for such rf excitations. To reduce the effect of the non-linearity of the Bloch equations on the rf profile because of the use of large-tip-angle rf pulses (resulting in increased signal loss from the ROIs), some optimization (*50,51*) of the sinc rf waveform may be needed.

Although the method described in this thesis was tested on an animal-model,

small-bore magnet, the technique should be accurate even on whole-body imaging systems. In a common clinical situation, a large exterior volume usually needs to be excited/saturated to localize a ROI within the body. This can be done by this method without increasing the localization time, and hence without sacrificing the SQ_{expt}. This is so, because for a given rf band width (pulse shape and duration), as used in this thesis, the excitation of a large outer region can be covered simply by reducing the amplitude G_r of the rotating gradient (solid lines in Fig. 3.1). A spoiler gradient (dashed lines in Fig. 3.1) of amplitude 9 mT/m, which is adequate to spoil the transverse magnetization after each rf excitation in a fraction of a millisecond, is achievable on whole-body systems. Thus, the total localization time for localizing a ROI on such systems will never be longer than that on the small-bore magnet, and, therefore, the localization quality should not be degraded. In fact, the performance of the technique on clinical scanners, which have better eddy current compensated units, should improve.

The advantages of employing this new technique for spatial localization are several: (i) since this technique enjoys the simplicity of the linear approximation Fourier transform method, the shape of the saturation rf pulses required for a desired shape of the saturation profile is easily and accurately determined; (ii) Projection Presaturation is conformal: *in vivo* targets of any shape can be more accurately conformed by irregular polyhedral ROIs with maximum S/N ratio; (iii) multiple ROIs can be localized simultaneously in a single presaturation cycle; (iv) localization by this technique is relatively fast (30-60 ms total localization time), though it can be made faster, if needed, by choosing large-tip-angle rf pulses and fewer gradient angles; (v) since the ROI is not

perturbed during the localization time, this method can be used for studying short T_2 species *in vivo*; (vi) the technique is tolerant of rf field inhomogeneity to a certain degree, because of the use of repeated rf applications to achieve saturation, a feature which should allow its implementation on surface coils; and (vii) because of the simple pulse sequences required, this technique can be easily implemented on any current clinical scanner.

Accurate spatial localization by outer volume suppression should have many applications in MR: (i) suppression of motion artifacts caused by blood flow in MR images; (ii) isolation of a group of spins for use as a natural flow marker in NMR flow studies; (iii) selective excitation of blood vessel segments for detailed quantification of flow and vascular anatomy; (iv) tissue characterization *in vivo* (since the ROI is not perturbed, even very short relaxation times from a localized volume can be measured accurately); (v) isolation of a tissue volume or volumes prior to performing localized spectroscopy for accurate determination of the metabolic states of tissue volumes *in vivo*, including those which have short T_2-species.

5.2 *Conclusions*

In summary, Projection Presaturation is an accurate, single-shot localization technique based on selective spatial presaturation. The technique does not suffer from the usual problems of accurate localization, being immune to tip-angle error problems, and therefore it achieves accurate localization with adequate outer volume suppression ($SQ_{expt} > 99.9\%$). Also, because of the use of small-tip-angle rf pulses, the slice-

selection profile is close to the ideal, and as such the localized ROIs have well defined boundaries. Furthermore, since the technique is conformal and also T_2-independent, the imaging, spectral or relaxometric data can be acquired with a high S/N ratio from accurately conformed *in vivo* targets. Because the method is robust and versatile and easily implementable on any current commercial scanner, it has many applications in clinical as well as research MR.

APPENDIX

Application of Projection Presaturation to Localized Relaxometry

A.1 *Introduction*

The spin-lattice relaxation time (T_1) and the spin-spin relaxation time (T_2) are the tissue-characteristic parameters in magnetic resonance. From a knowledge of tissue-specific T_1 and T_2, the imaging parameters can be optimized to achieve maximum contrast between normal and pathologic tissues by MRI. Furthermore, these parameters may even provide information for characterizing tissue, e.g. whether a lesion is benign or malignant. Obtaining this degree of tissue discrimination by differential relaxometry puts a much higher demand on the accuracy of measurement of tissue relaxation times. It is this goal which has led to the development of a number of techniques for measuring the relaxation parameters *in vivo*.

Conventional pulse spectrometer techniques, such as inversion recovery, IR (*52*) and the Carr-Purcell-Meiboom-Gill (CPMG) sequence (*53,54*) have been successfully applied to MRI to calculate relaxation times of *in vivo* samples from a set of MR images. However, the accuracy of calculation is severely limited because of the small number of data points used to sample the relaxation curves. For example, because of the frequency encoding of each echo, the echo time (TE) in clinical imaging is relatively large ($\sim$ 20 - 30 ms), and so the maximum number of echoes acquired in multi-echo MRI to sample the T_2 curve of short T_2 species (typically, 10 - 15 ms T_2 value) seldom exceeds ten. Similarly, because of the phase encoding of each image, the long time required to obtain

an adequate number of images, corresponding to different inversion times (TIs), for more accurate T_1 estimation may be prohibitive in clinical MRI. The total imaging time is usually compromised by taking fewer points (images) to sample the inversion recovery curve. Thus, the reduced number of data points used to sample the relaxation curves can lead to systematic errors in the multi-component analysis of tissue relaxation data, particularly in the presence of rf imperfections (*55*) and readout gradients. To explore the presence of multi-compartments in a tissue volume, the relaxation curves must be sampled with an adequate number of points.

In recent years, spatial localization techniques have been combined with pulse spectrometer techniques to measure the relaxation times of tissue regions *in vivo*. Since phase- or frequency-encoding is not needed in this procedure, the relaxation curves can be sampled sufficiently in a relatively short time to allow multi-component analysis.

A brief review of several techniques of spatial localization applied to localized relaxometry/spectroscopy has been presented in chapter 1. Since the techniques based on selective excitation (*3-13*) suffer from the T_2 decay problem, the total number of echoes acquired from the ROI, localized by these techniques, to describe the T_2 decay curve is severely limited. This, possibly, rules out the application of these techniques to multi-component short T_2-species. To obtain densely sampled data of high S/N ratio, a saturation technique must be used to isolate well defined ROI(s), whose magnetization is unperturbed prior to acquiring relaxation data.

Projection Presaturation should enable one to acquire multi-point relaxation data from accurately localized ROIs of any desired shape and size (*34*). Here (*56*), I present

the application of Projection Presaturation, properly combined with the techniques for measuring relaxation times, to acquire relaxation data from an accurately localized ROI. Results of a phantom study are presented to demonstrate the accuracy of the method.

A.2 *Methodology*

In this section, first, a specific strategy for more accurate localization of a small ROI (diameter $\leq$ 10 mm) by presaturating a relatively large exterior volume is presented. Then, the appropriate techniques for acquiring relaxation data from this ROI are pointed out and the scheme for further minimizing the contamination of the localized relaxometric data from outside is used.

As was described in chapter 3, a pair of frequency-offset sinc rf pulses is repeated at an appropriate number of gradient angles to localize a single ROI. If these pulses are used to cover the excitation of a large exterior volume, leaving a small ROI (typical diameter $\leq$ 10 mm) unperturbed within that volume, the transition regions in the rf profiles will be wide, thus defining the ROI boundary less accurately. In order to sharpen the ROI boundary, an "edge sharpening" scheme, as described briefly in chapter 3, is introduced here and described in more detail.

According to the "edge sharpening" scheme, each box on either side of the ROI in the rf profile is decomposed into at least two (the advantage of doing this will be clear soon). For example, for localizing a single ROI, each box on either side of the ROI projection in the single profile, P_s, of Fig. 3.2a is decomposed into two (see Fig. A.1):

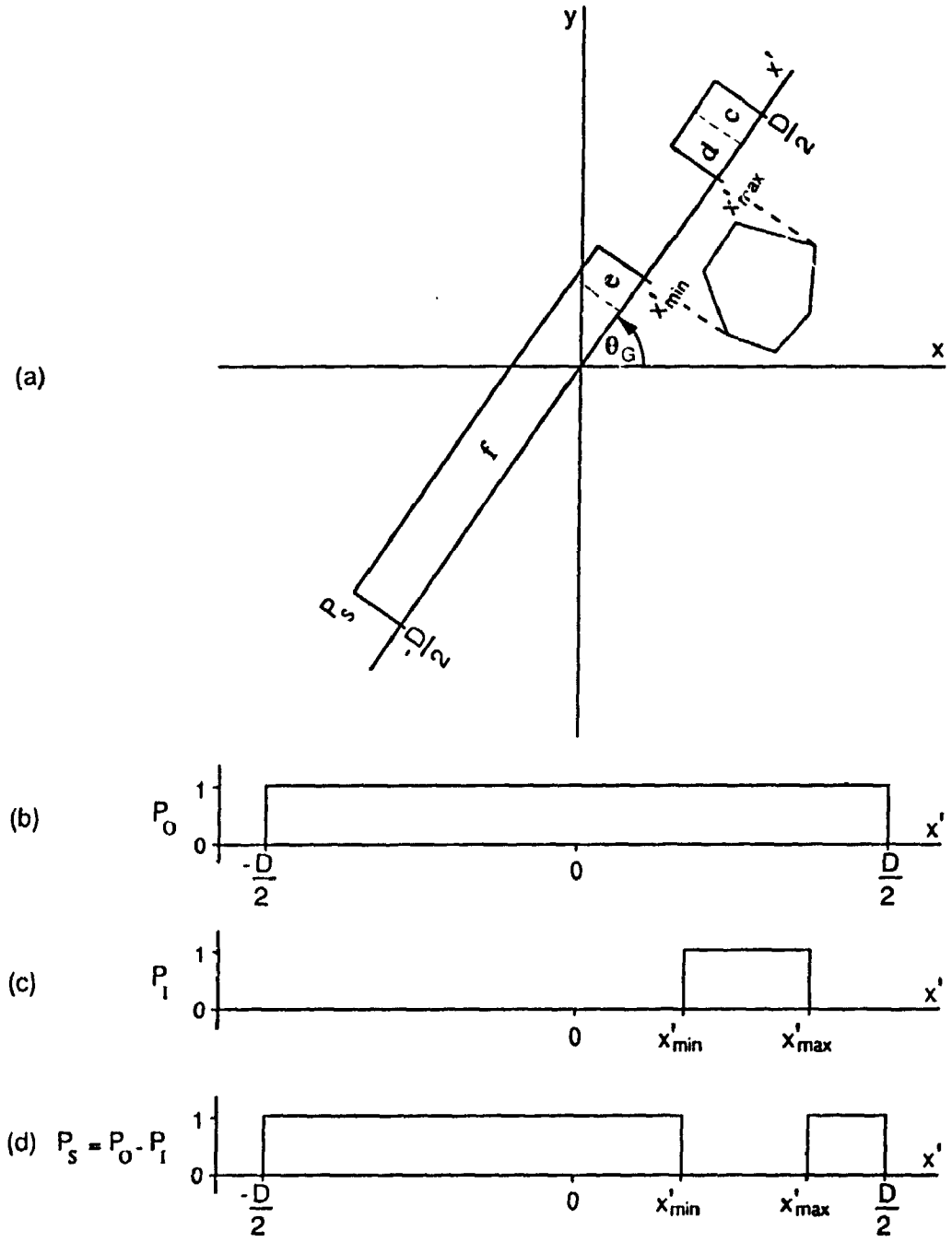

FIG. A.1. A scheme for sharpening the ROI boundary, while presaturating a large exterior volume of diameter D. Each box on either side of the ROI projection in the single profile, $P_s^{sharp}(\theta_G)$, at angle θ_G is decomposed into two: wide regions ("c" and "f") and narrow regions ("d" and "e") of equal width w in the immediate vicinity of the ROI projection. The saturation rf pulses, corresponding to the regions (d and e) of width w, will have sharp and identical transition regions, and, therefore, would lead to the isolation of a ROI with a sharp boundary. The rf pulses, corresponding to the wide regions (c and f), will excite the remainder of the outer region and presaturate the same.

narrow and wide regions, with the narrow regions of equal width "w" right next to the ROI projection. Note that the width, w, has been chosen constant and is the same at all angles of rotation, θ_G. The rf pulses, corresponding to the desired rectangular profile of width w, will have, in reality, sharp and identical transition regions on either side of the ROI projection at all gradient angles. Multiple application of such pulses, in a rotating gradient scheme, would isolate a ROI with well defined boundary. The rf pulses, corresponding to the wide regions in Fig. A.1, will excite the remainder of the outer region and presaturate the same. Thus the advantage of incorporating the "edge sharpening" scheme into the "conventional" Projection Presaturation is clear: the ROI will be sharper.

The rf pulse shape, corresponding to the desired profile of Fig. A.1, can be obtained, as follows:

The single profile, $P_s^{sharp}(\theta_G)$, of Fig. A.1 can be analytically expressed as a sum of RECT functions as

$$P_s^{sharp}(\theta_G) = \sum_{j=c,d,e,f} \text{RECT}\,[(\nu - \nu_j(\theta_G))/\Delta\nu_j(\theta_G)]\ , \qquad [A.1]$$

where widths of the RECT functions are given by

$$\Delta\nu_c(\theta_G) = (\gamma/4\pi)\, G_r\, [D - 2\,w - 2\,x'_{max}(\theta_G)]\ , \qquad [A.2a]$$

$$\Delta\nu_d \equiv \Delta\nu_e = (\gamma/2\pi)\, G_r\, w\ , \qquad [A.2b]$$

$$\Delta\nu_f(\theta_G) = (\gamma/4\pi)\, G_r\, [D - 2\,w + 2\,x'_{min}(\theta_G)]\ , \qquad [A.2c]$$

and center-offsets are given by

$$\nu_c(\theta_G) = (\gamma/8\pi)\, G_r\, [D + 2\,x'_{max}(\theta_G) + 2\,w]\ , \qquad [A.2d]$$

$$\nu_d(\theta_G) = (\gamma/4\pi)\, G_r\, [2\, x'_{max}(\theta_G) + w]\,, \qquad [A.2e]$$

$$\nu_e(\theta_G) = (\gamma/4\pi)\, G_r\, [2\, x'_{min}(\theta_G) - w]\,, \qquad [A.2f]$$

$$\nu_f(\theta_G) = -\,(\gamma/8\pi)\, G_r\, [D - 2\, x'_{min}(\theta_G) + 2\, w]\,. \qquad [A.2g]$$

In Eqs. [A.1] and [A.2], j labels the boxes, G_r is the amplitude of the rotating gradient, D is the diameter of the object, and x'_{max}, x'_{min} are the maximum, minimum projections, respectively, of the ROI vertices onto the gradient direction θ_G, as described in chapter 3. Under the small-tip angle approximation, the corresponding rf pulse shape, $B_1(t,\theta_G)$, can then be obtained by inverse Fourier transforming the profile, $P_S^{sharp}(\theta_G)$, of Eq. [A.1] as

$$B_1(t, \theta_G) = \sum_{j=c,d,e,f} \mathrm{sinc}(\pi\, \Delta\nu_j(\theta_G)\, t)\, \exp(i\, 2\pi\, \nu_j(\theta_G)\, t)\,. \qquad [A.3]$$

Multiple application of this rf pulse, in a rotating gradient scheme, will lead to the localization of a ROI with a sharper boundary. The individual sinc pulses, composing the rf pulse, $B_1(t,\theta_G)$, in Eq. [A.3] can be applied successively with their respective bandwidth (duration) and frequency-offset, as given by Eq. [A.2]. Because of the additional pulses included in the sequence, this version of Projection Presaturation requires a longer localization time for a given rf tip-angle. In order to keep the total localization time in the modified sequence much shorter than the T_1 of the outer volume species (so that the recovery of the saturated spins of outer volume during localization is insignificant), fewer gradient angles (< 36) and saturation pulses of large tip-angle ($> 30^o$) can be used (see Eq. [2.3]) to achieve adequate SQ_{expt} (*e.g.* $SQ_{expt} > 99.9\%$).

To acquire relaxation data from a localized ROI, the IR and CPMG sequences are

then combined with the modified localization sequence, as described above. In order to eliminate the effect of T_1 recovery of the saturated spins of the outer volume on the relaxation data, a data subtraction scheme, as described and employed in chapter 4, is used.

A.3 *Implementation*

The method, described in the previous section, for acquiring relaxation data from a localized ROI has been tested in a phantom study. The phantom consisted of two hollow, co-axial cylinders of length 103 mm and inner diameters 83 and 18 mm. The outer cylinder ("bath") was filled with water doped with copper sulphate to a T_1 of about 1 s and T_2 of 400 ms. The inner cylinder was refilled with aqueous solutions of copper sulphate of various concentrations in the range 1 - 6 mM. A standard 2DFT image of the phantom is shown in Fig. A.2a.

The localization-sequence parameters were chosen so as to localize a single, cylindrical ROI of the desired diameter, d ($= x'_{max}(\theta_G) - x'_{min}(\theta_G)$) = 10 mm at the center of the phantom by presaturating the outer cylindrical volume of diameter D = 100 mm. The width w of the box in Fig. A.1 was chosen to be 20 mm. Four sinc waveforms, each truncated after four zero-crossings, composing the rf pulse $B_1(t,\theta_G)$ in Eq. [A.3], were applied successively with their respective offsets, as given by Eqs. [A.2d - A.2g], at each gradient angle. The duration of each of the two sinc pulses producing excitation in the immediate vicinity of the ROI was 521.8 μs, and that of each of the remaining two exciting the remainder of the outer region was 417.5 μs. The rf power

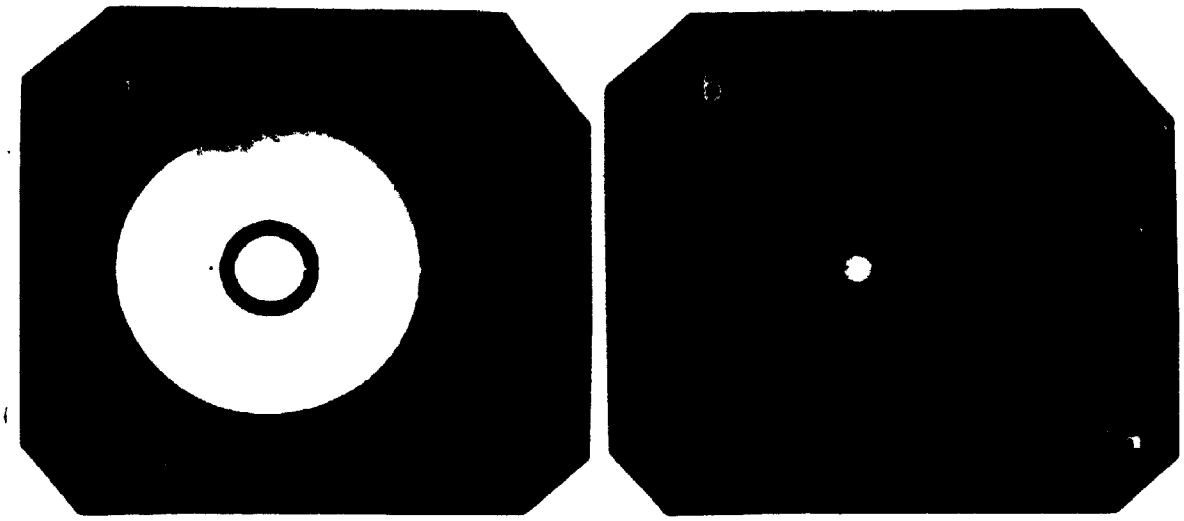

FIG. A.2. Normal and localized image of a phantom, used for localized relaxometry by Projection Presaturation: (a) a standard transverse image of the phantom consisting of two hollow, co-axial cylinders of length 103 mm and inner diameters 83 and 18 mm; (b) a transverse image of the same phantom after presaturating the outer volume, thus localizing a cylindrical ROI of diameter 1 cm at the center of the phantom. Twenty four gradient angles and four frequency-offset sinc pulses, each of tip-angle 45°, applied at each gradient angle were used to presaturate the outer volume to a $SQ_{expt} > 99.9\%$.

of each pulse was scaled to a tip-angle of about 45°. Twenty four gradient angles were used at equal angular intervals over one complete cycle of the rotating gradient. The amplitude of the rotating gradient (solid lines in Fig. 3.1) was G_r = 9 mT/m, which was adequate to dephase the existing transverse magnetization of the outer region in ~ 0.7 ms after rf excitation at each angle. The spoiler gradients (dashed lines) were not needed for this particular study. A volume imaging coil was used in the transmit/receive mode. No signal averaging or phase cycling of the rf pulses was performed. A standard 2DFT image of the phantom after presaturation is shown in Fig. A.2b: the outer volume is suppressed better than 99.9%.

As is clear from Fig. A.2b, the localized centered, cylindrical ROI has well defined boundaries. This could not have been achieved had only two frequency-offset sinc pulses (see Eqs. [3.8] and [3.9]), instead of four (see Eqs. [A.2] and [A.3]), been used in the localization sequence to localize the desired ROI. As is shown in Fig. A.3, the unexcited region (ROI) at the center in the composite profile of the set of four offset sinc pulses (see Fig. A.3b) has a better defined boundary and lower magnitude of unwanted excitation than that in the composite profile of two offset sinc pulses (see Fig. A.3a). This feature of the former set of pulses, in a rotating gradient scheme, produces a ROI of sharp boundaries, as demonstrated in Fig. A.2b.

To acquire T_1 relaxation data from the localized ROI of Fig. A.2b, an IR sequence was combined with the localization sequence, as described above. The 180° inversion pulse of the IR sequence was applied before the localization sequence, with a

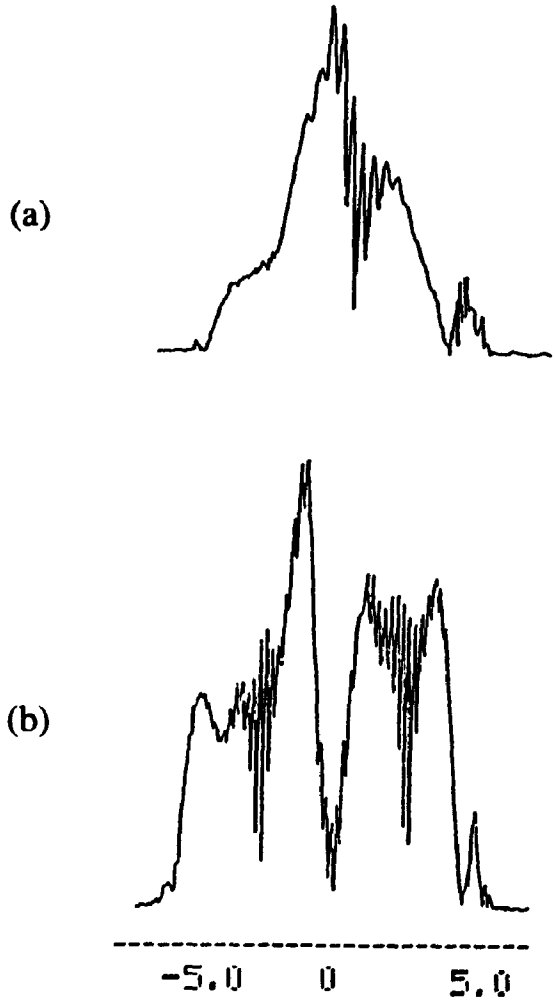

Fig. A.3. Slice profiles of a set of two and four frequency-offset sinc rf pulses shown together: (a) slice-profile of a pair of two offset sinc pulses (Eqs. [3.8] and [3.9]), obtained in a single spin-echo experiment; (b) Slice-profile of a set of four offset sinc pulses (Eqs. [A.2] and [A.3]), used to localize the ROI of Fig. A.2b. In each case, each sinc rf waveform was truncated after four zero-crossings, and each sinc had a tip-angle of 45°. In the slice-profile study, the composite slice in both cases (a and b) had a desired thickness (extent) of 100 mm with 10 mm unexcited region at the center. The spatial modulation of the signal intensity in both profiles is a consequence of the interference of the sub-slices defined by the individual sinc pulses and the slice-select gradients in the spin-echo experiments.

variable delay (VD) between it and the localization sequence, as shown in Fig. A.4a. Because of the eddy current problems on our imaging system caused by switching the gradients, the non-selective 90° pulse of the IR sequence was applied 35 ms (eddy current settling time) after the localization sequence. The durations of the non-selective 180° and 90° pulses in the IR sequence were 218 and 109 μs, respectively. In order to eliminate the effect of the recovery of the longitudinal magnetization in the outer region on relaxation measurements during the 35-ms waiting time, an additional, non-selective 180° pulse was turned on/off in front of the sequence of Fig. A.4a, as shown in Fig. A.4b. The difference of the two acquisitions was used to sample the IR curve. Twenty VDs, ranging from 0 to $5T_1$ were used to sample the IR curve. The Beginning part of the curve was sampled more densely than the later part for more accurate curve fitting to the relaxation data.

For T_2 measurements, a CPMG sequence was applied after the localization sequence, as shown in Fig. A.5. Again, because of the eddy current problems, the 90° pulse of the CPMG was applied 35 ms after the localization sequence, and the effect of recovery of the outer volume magnetization on T_2 data was eliminated using a similar scheme to the above. In this study, the echo time was 12 ms for samples of higher concentrations (*e.g.* 6 mM) and 20 ms for those of lower concentrations (*e.g.* $\leq$ 2 mM). The T_2 decay curve was sampled with twenty points.

The T_1, T_2 measurements of the same concentrations were performed on separate vials using the IR and CPMG sequences on the same imager running in the spectrometer mode (gradients off). Twenty TIs were used to sample the IR curve and the same

FIG. A.4. Pulse sequence to acquire longitudinal relaxation data from a localized ROI, and a data subtraction scheme to eliminate the effect of partial recovery of the saturated spins on the data. (a) A 180° rf pulse of the IR sequence applied before the Projection Presaturation (PP) sequence with a variable delay (VD) between it and the PP. The 90° read pulse can be applied immediately after PP on eddy current compensated systems to acquire longitudinal relaxation data from the localized ROI. (b) A non-selective 180° rf turned on/off in front of the sequence of Fig. a to eliminate the effect of partial recovery of outer volume magnetization (recovered during eddy current settling time (WT), allowed between PP and the 90° pulse on an uncompensated system, on relaxation data. Because of identical recovery, the outer volume signals cancel out on data subtraction; whereas ROI signals are of opposite sign in the two cases (180° on/off) and add up.

(a)

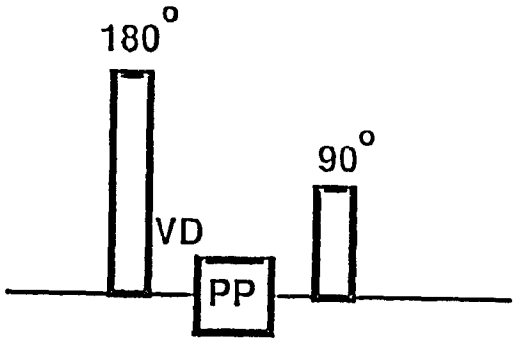
180°
90°
VD
PP

(b)

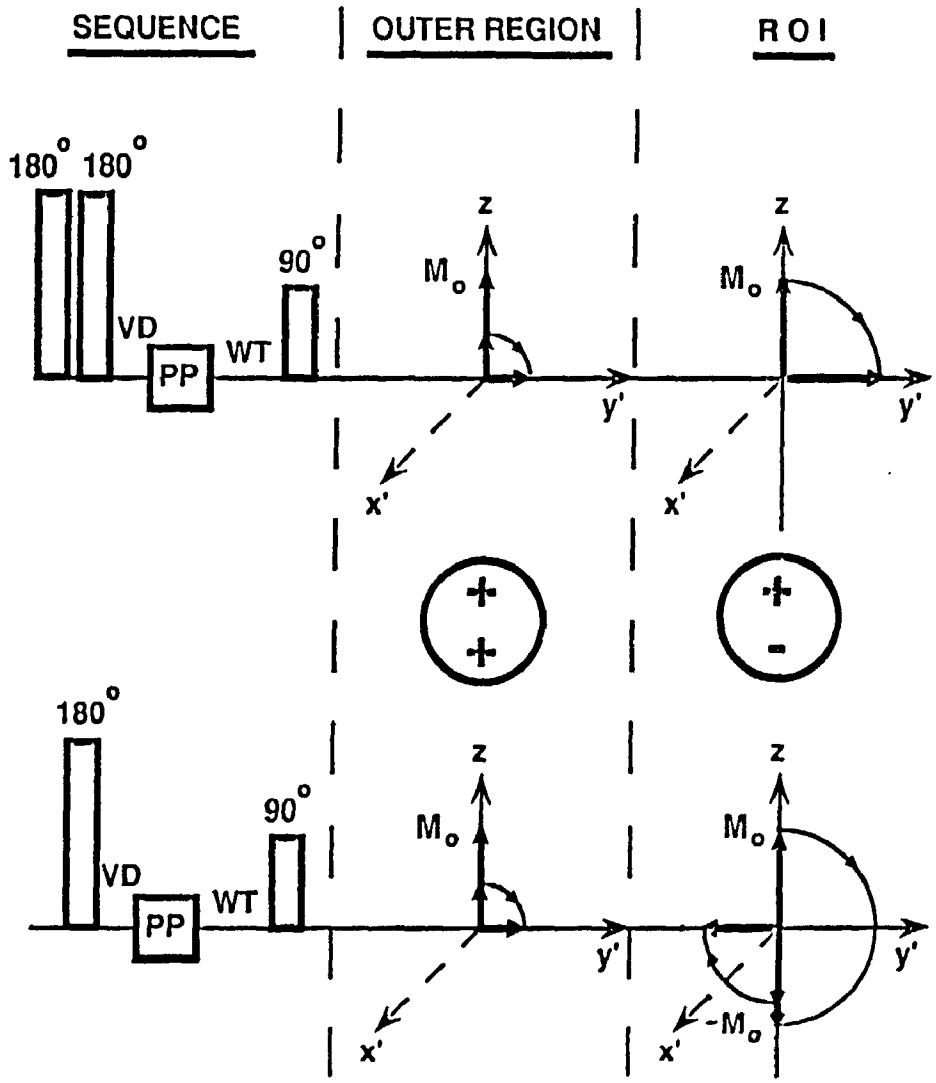
SEQUENCE
OUTER REGION
ROI
180°
180°
90°
VD
PP
WT
z
M₀
y'
x'
+
+
+
-
180°
90°
VD
PP
WT
z
M₀
y'
x'
-M₀

FIG. A.5. Pulse sequence to acquire T_2 relaxation data from a localized ROI and the data subtraction scheme, same as in Fig. A.4b: (a) a CPMG sequence is applied immediately after the PP sequence to acquire T_2 relaxation data from the localized ROI on a compensated gradient system; (b) on an uncompensated system, a non-selective 180° rf pulse is turned on/off in front of the PP sequence, and the difference of the two acquisitions (one with and the other without 180° rf pulse) is used to cancel the contribution to the relaxation data from the ROI of the outer volume magnetization, recovered during the waiting time (WT) allowed between the PP and the 90° pulse for the eddy currents to settle down.

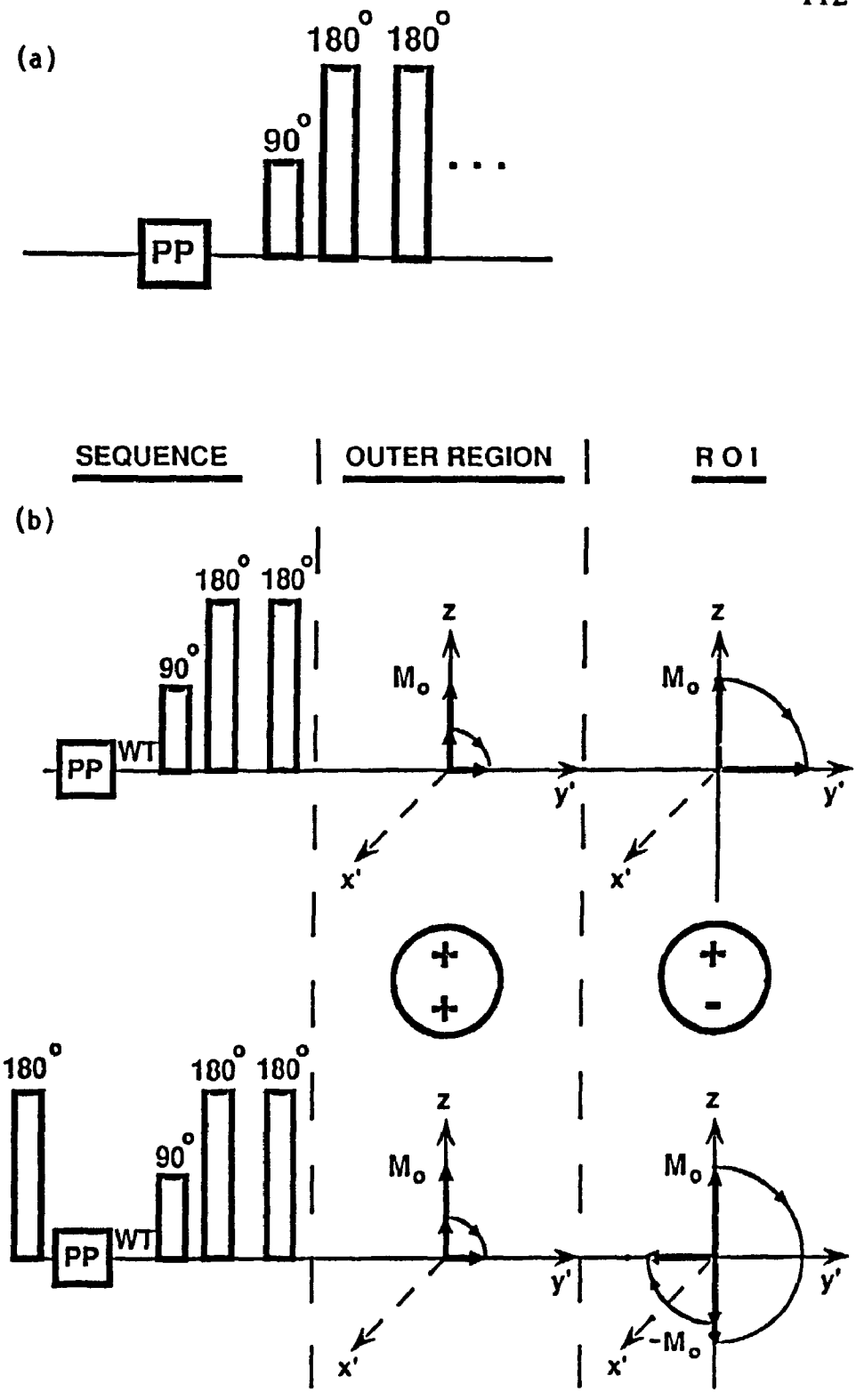
(a)
180°
180°
90°
PP
(b)
SEQUENCE
OUTER REGION
ROI
180°
180°
90°
PP
WT
z
M_o
y'
x'
+
+
+
-
180°
180°
180°
90°
PP
WT
z
M_o
y'
x'
$-M_o$

number of TEs were used to sample the T_2 decay curve.

Finally, the imager was used to obtain IR images for eleven different TIs ranging from 115 to 5015 ms, and sixteen echo-images to sample the relaxation curves. The phantom consisted of a bundle of vials of the same samples of various concentrations, as mentioned above. In each case, transverse slice images of the phantom with a slice thickness of 6 mm, FOV of 60 mm, TE of 30 ms, and an image matrix of 128 x 128, were used for collecting relaxation data.

All T_1, T_2 measurements on various concentrations of copper sulphate solution are shown in tables 2 and 3, respectively. Localized T_1 data agree within 6% and T_2 data within 8% with the corresponding spectrometer measurements, as described above. The localized and imager data were similar. The plots of relaxation rates against concentration are shown in Fig. A.6. From this preliminary study, it appears that the relationship between the relaxation rates and the concentration is linear (see Fig. A.6); however, further study with more data points on the graphs of Figs. A.6a and A.6b is needed to validate the linear relationship.

A.4 *Discussion*

In this Appendix, the modified version of Projection Presaturation was used to localize a small ROI by presaturating a relatively large outer region accurately. A data subtraction scheme was used to eliminate the effect of partial recovery of saturated spins on the relaxation data. The conventional IR and CPMG methods of relaxation time measurements in combination with the modified localization sequence provided multi-point relaxation data in a reasonably short time (< 6 minutes); however, on eddy current

TABLE 2

Longitudinal relaxation time measurements[a] on copper sulphate solutions

Copper Sulphate concentration (mM)	T_1 (ms)		
	Imager as Spectrometer	Imager with Localization	Imager without Localization
1.0	968	1005	1050
2.0	556	568	578
6.0	246	260	270

TABLE 3

Transverse relaxation time measurements[a] on copper sulphate solutions

Copper Sulphate concentration (mM)	T_2 (ms)		
	Imager as Spectrometer	Imager with Localization	Imager without Localization
1.0	427	397	385
2.0	355	341	323
6.0	128	120	116

a All measurements have an estimated error of less than 4%.

FIG. A.6. Relaxation rates, obtained from tables 2 and 3, plotted against various sample concentrations: (a) Longitudinal relaxation rate ($1/T_1$ s^{-1}) vs copper sulphate concentration (mM); (b) Transverse relaxation rate ($1/T_2$ s^{-1}) vs copper sulphate concentration. In either graph, the spectrometer data are shown as triangles, the localized data as squares, and the imager data as circles. Localized T_1 data agree within 6% and T_2 data within 8% with the corresponding spectrometer measurements. The relationship between the relaxation rates and the concentration appears to be the linear.

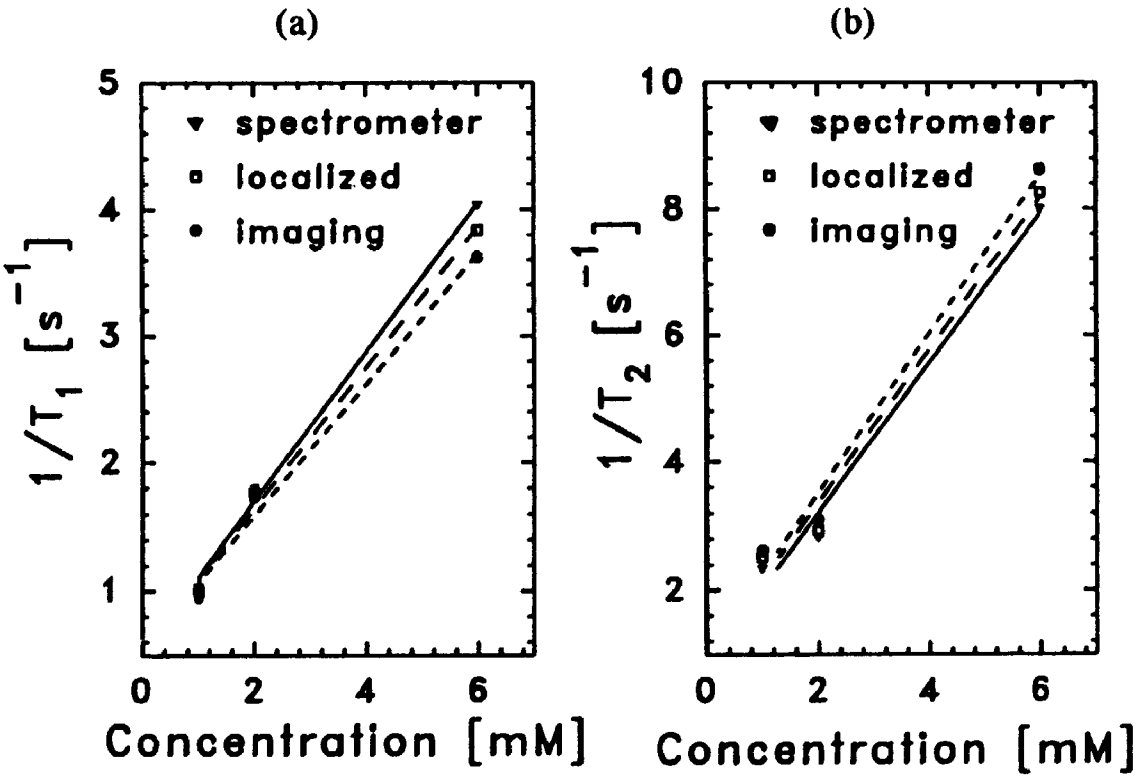
(a)
(b)
spectrometer
localized
imaging
$1/T_1$ [s^{-1}]
$1/T_2$ [s^{-1}]
Concentration [mM]
Concentration [mM]

compensated systems, the total time need not exceed 3 minutes. The spectrometer and localized data agreed within 8%. The imager and localized data were similar. The relationship between relaxation rates and concentration appeared to be the linear.

Though the localized relaxometry by Projection Presaturation was demonstrated on a stationary phantom, the technique should be quite suitable to *in vivo* studies as well. In the *in vivo* situation, the ROI signal is usually contaminated by the "foreign material" brought into the ROI by blood flow. Since in Projection Presaturation, the localization of the ROI is performed by outer volume suppression in a single-shot, any contamination of the ROI signal from outside caused by blood flow will automatically be eliminated. Because the Projection Presaturation avoids any excitation of the ROI magnetization during the localization, the ROI signal is T_2 independent. For this reason, localized volume relaxometry by this method is most suitable even for short T_2 species. Since phase encoding is not needed, relaxation curves can be well sampled in time to check up on the multi-component behavior of a tissue volume, where appropriate. Secondly, adequate sampling of the baseline of the relaxation curves makes the calculated relaxation times less prone to the effect of mistuning of the rf pulses.

The ROI signal in the case of the modified version of Projection Presaturation which uses a data subtraction scheme is not totally unaffected. The additional 180^{o} pulse (Figs. A.4 and A.5) inverts the ROI magnetization, which then recovers over the period of TL plus WT resulting in the reduction of the ROI signal after subtraction. However, this signal loss should have no effect on the accuracy of T_1, T_2 measurements, as found in this study.

Overall, localized relaxometry by Projection Presaturation should have an advantage over the imaging technique. The major advantage of estimating the relaxation time from a set of conventional MR images is the high spatial resolution of the ROI. Also, the S/N ratio of the relaxation data from a ROI in the image benefits from the signal that accumulates over the phase encoding steps. However, for a localized ROI size equal to the ROI size in the image (for an image ROI that extends over several voxels), the S/N ratio of the localized ROI data for an equal scan time is usually superior to that of the image ROI data (*57*). Therefore, the high S/N ratio of the localized data can be traded off against the reduction in the total relaxation data collection time. Furthermore, localized volume relaxometry avoids errors in the estimation of relaxation times, which occur in 2D (*58-60*) or 1D (*61*) imaging because of tip-angle variation across the slice selection.

The good agreement between the imaging and localized data, reported here, may be attributed to several factors, including good rf and magnetic field homogeneities over the extent of the centered small vials chosen for imaging, and the relatively large number of images used to sample the relaxation curves, as compared to clinical MRI, which generally uses a few, typically four or fewer, images for the same purpose. However, in a common clinical situation, not all of the above mentioned choices can be made, and, thus, the agreement between imaging and the localized data is expected to be far less.

In summary, considering the accuracy of localization by outer volume suppression, the high S/N ratio of relaxation data acquired in a relatively short time, and the accuracy of relaxation time measurement, the Projection Presaturation method may

come to be preferred over the imaging technique for measuring relaxation times *in vivo*, particularly, in the region where flow/motion cause contamination of the ROI data. However, in order to establish the full superiority of the PP over imaging methods, further study on the localized relaxometry by PP, preferrably in vivo, is needed. Furthermore, the use of PP in conjunction with an add/subtract data cycle (if needed) and the fast spectrometer techniques for T_1 measurement, such as the one proposed by Look and Locker (*62*), instead of IR, should enable one to acquire localized T_1 data in a much shorter time (a few seconds), so that the total time for T_1, T_2 data collection should not take more than a few seconds.

REFERENCES

1. F. Bloch, W. W. Hansen, and M. E. Packard, Nuclear Induction, *Phys. Rev.* **69**, 127 (1946).

2. E. M. Purcell, H. C. Torrey, and R. V. Pound, Resonance Absorption by Nuclear Magnetic Moments in a Solid, *Phys. Rev.* **69**, 37 (1946).

3. P. A. Bottomley, T. H. Foster and R. D. Darrow, Depth-Resolved Surface-Coil Spectroscopy (DRESS) for *in Vivo* ^{1}H, ^{31}P, and ^{13}C NMR, *J. Magn. Reson.* **59**, 338 (1984).

4. W. P. Aue, S. Muller, T. A. Cross, and J. Seelig, Volume-Selective Excitation. A Novel Approach to Topical NMR, *J. Magn. Reson.* **56**, 350 (1984).

5. P. R. Luyten, A. J. H. Marien, B. Sijtsma and J. A. Den Hollander, Solvent-Suppressed Spatially Resolved Spectroscopy. An Approach to High-Resolution NMR on a Whole-Body MR System, *J. Magn. Reson.* **67**, 148 (1986).

6. R. J. Ordridge, A. Connelly and J. A. B. Lohman, Image-Selected *in Vivo* Spectroscopy (ISIS). A New Technique for Spatially Selective NMR Spectroscopy, *J. Magn. Reson.* **66**, 283 (1986).

7. J. Granot, Selective Volume Excitation Using Stimulated Echoes (VEST). Applications to Spatially Localized Spectroscopy and Imaging, *J. Magn. Reson.* **70**, 488 (1986).

8. J. Frahm, K.-D. Merboldt, and W. Hanicke, Localized Proton Spectroscopy Using Stimulated Echoes, *J. Magn. Reson.* **72**, 502 (1987).

9. C. J. Hardy, P. A. Bottomley, M. O'donnell, and P. Roemer, Optimization of Two-Dimensional Spatially Selective NMR Pulses by Simulated Annealing, *J. Magn. Reson.* **77**, 233 (1988).

10. J. Pauly, D. Nishimura, and A. Macovski, A K-Space Analysis of Small-Tip-Angle Excitation, *J. Magn. Reson.* **81**, 43 (1989).

11. B. K. Rutt, Selective Excitation by Filtered Backprojection, in "Proceedings, 7th Annual Meeting of the Society of Magnetic Resonance in Medicine", "Works in Progress", p. 145, Society of Magnetic Resonance in Medicine, San Francisco, 1988.

12. P. A. Bottomley and C. J. Hardy, PROGRESS in Efficient Three-Dimensional Spatially Localized *in Vivo* ^{31}P NMR Spectroscopy Using Multidimensional

Spatially Selective (ρ) Pulses, *J. Magn. Reson.* **74**, 550 (1987).

13. C. J. Hardy, P. A. Bottomley and P. B. Roemer, Off-axis Spatial Localization with Frequency Modulated Nuclear Magnetic Resonance Rotating (ρ) Pulses, *J. Appl. Phys.* **63(9)**, 1 May 1988.

14. A. Connelly, C. Counsell, J. A. B. Lohman and R. J. Ordridge, Outer Volume Suppressed Image Related in Vivo Spectroscopy (OSIRIS), a High-Sensitivity Localization Technique, *J. Magn. Reson.* **78**, 519 (1988).

15. D. M. Doddrell, J. M. Bulsing, G. J. Galloway, W. M. Brooks, J. Field, M. Irving and H. Baddeley, Discrete Isolation from Gradient-Governed Elimination of Resonances. DIGGER, a New Technique for *in Vivo* Volume-Selected NMR Spectroscopy, *J. Magn. Reson.* **70**, 319 (1986).

16. W. M. Chew, L.-H. Chang, D. P. Flamig and T. L. James, The SWIFT Method for *in Vivo* Localized Excitation (SMILE), *J. Magn. Reson.* **75**, 523 (1987).

17. A. T. Hsu, W. W. Hunter, JR., P. Schmalbrock and A. G. Marshall, Stored Waveform Inverse Fourier-Transform (SWIFT) Excitation for Water-Suppressed Whole-body Slice-Selected Proton Chemical Shift Spectra at 1.5 Tesla, *J. Magn. Reson.* **72**, 75 (1987).

18. R. Gonzalez-Mendez, H. Engeseth, A. A. B. Gibson, J. DE Olivares, L. Litt and T. L. James, The Modulation Theorem in Tailored Radiofrequency Excitation and its Application to a Notch Filter, *J. Magn. Reson.* **78**, 308 (1988).

19. U. Klose, Space-Selective Saturation by Frequency Modulated Pulses, in "Proceedings, 7th Annual Meeting of the Society of Magnetic Resonance in Medicine", Vol. 2, p.1059, Society of Magnetic Resonance in Medicine, San Francisco, 1988.

20. A. Haase, Localization of Unaffected Spins in NMR Imaging and Spectroscopy (LOCUS Spectroscopy), *Magn. Reson. Med.* **3**, 963, (1986).

21. D. M. Doddrell, W. M. Brooks, J. M. Bulsing, J. Field, M. G. Irving and H. Baddeley, Spatial and Chemical-Shift-Encoded Excitation. SPACE, a New Technique for Volume-Selected NMR Spectroscopy, *J. Magn. Reson.* **68**, 367 (1986).

22. A. N. Garroway, P. K. Grannell, and P. Mansfield, Image Formation in NMR by a Selective Irradiative Process, *J. Phys. C:7*, L457 (1974).

23. A. P. Crawley and R. M. Henkelman, Accurate Measurement of Proton Relaxation Times from a Localized Volume, in "Proceeding, 7th Annual Meeting of the Society of Magnetic Resonance in Medicine", vol. 1, p. 229, Society of Magnetic Resonance in Medicine, San Francisco, 1988.

24. W. S. Hinshaw, Image Formation by Nuclear Magnetic Resonance: The Sensitive-Point Method, *J. Appl. Phys.* **47**, 3709 (1976).

25. W. S. Hinshaw, P. A. Bottomley, and G. N. Holland, Radiographic Thin-Section Image of the Human Wrist by Nuclear Magnetic Resonance, *Nature* **270**, 722 (1977).

26. R. Sauter, S. Mueller and H. Weber, Localization in *in Vivo* ^{31}P NMR Spectroscopy by Combining Surface Coils and Slice-Selective Saturation, *J. Magn. Reson.* **75**, 167 (1987).

27. S. Singh and B. K. Rutt, Three-Dimensional Spatial Presaturation: A Fast Technique for Spatial Localization of Arbitrary Shapes in MR Imaging and Spectroscopy, in "Proceedings, 74th Annual Meeting of the Radiological Society of North America", Radiology 169(P), p. 390, Chicago, 1988.

28. S. Singh and B. K. Rutt, A Fast Technique for Accurate Volume Localization by Rotating Gradient, in "Proceedings, 8th Annual Meeting of the Society of Magnetic Resonance in Medicine", Vol. 1, p. 29, Society of Magnetic Resonance in Medicine, Amsterdam, 1989.

29. S. Singh and B. K. Rutt, Single-Shot Localization of Very Small Off-axis Regions of Interest by Projection Presaturation, in "Proceedings, 8th Annual Meeting of the Society for Magnetic Resonance Imaging," Book of Abstracts, p. 115, Society for Magnetic Resonance Imaging, Washington, D.C., 1990.

30. S. Singh, B. K. Rutt, and R. M. Henkelman, Projection Presaturation: A Fast and Accurate Technique for Multidimensional Spatial Localization, *J. Magn. Reson.* 87, 567 (1990).

31. S. Singh, S. Napel and B. K. Rutt, Single-Shot Localization of Multiple Regions of Interest by Projection Presaturation, in "Proceedings, 9th Annual Meeting of the Society of Magnetic Resonance in Medicine", Vol. 1, p. 599, Society of Magnetic Resonance in Medicine, New York, 1990.

32. S. Singh and B. K. Rutt, Projection Presaturation II: Single-Shot Localization of Multiple Regions of Interest, *J. Magn. Reson.* **90**, 313-329 (1990).

33. S. Singh, S. Napel and B. K. Rutt, Accurate Localization of a Single, Arbitrarily Shaped Region of Interest by a Slowly Varying Gradient, in "Proceedings, 2nd Annual Meeting of the Canadian Organization of Medical Physicists", Montreal, 1990.

34. S. Singh, B. K. Rutt, and C. P. S. Taylor, Accurate Proton Relaxation Times Measurements from a Localized Region, in "Proceedings, 9th Annual Meeting of the Society of Magnetic Resonance in Medicine", "Works in Progress", p. 1167, Society of Magnetic Resonance in Medicine, New York, 1990.

35. S. Singh, B. K. Rutt, and C. P. S. Taylor, Some Applications of Projection Presaturation in Imaging and Spectroscopy, in "Proceedings, 9th Annual Meeting of the Society of Magnetic Resonance in Medicine", "Works in Progress", p. 1347, Society of Magnetic Resonance in Medicine, New York, 1990.

36. D. I. Hoult, The Solution of the Bloch Equations in the Presence of a Varying B_1 Field - An Approach to Selective Pulse Analysis, *J. Magn. Reson.* 35, 66 (1979).

37. T. J. Lawry, G. S. Karczmar, M. W. Weiner and G. B. Matson, Computer Simulation of MRS Localization Techniques: An Analysis of ISIS, *Magn. Reson. Med.* 9, 299 (1989).

38. V. Smith and T. L. James, Notch Band Tailored Excitation Using Optimal Control Theory, in "Proceedings, 7th Annual Meeting of the Society of Magnetic Resonance in Medicine", Vol. 2, p. 1026, Society of Magnetic Resonance in Medicine, San Francisco, 1988.

39. J. Pauly, S. Conolly, D. Nishimura and A. Macovski, Slice-Selective Excitation for Very Short T_2 Species, in "Proceedings, 8th Annual Meeting of the Society of Magnetic Resonance in Medicine", Vol. 1, p. 28, Society of Magnetic Resonance in Medicine, Amsterdam, 1989.

40. J. C. Sharp and M. O. Leach, Conformal NMR Spectroscopy: Accurate Localization to Noncuboidal Volumes with Optimum SNR, *Magn. Reson. Med.* 11, 376 (1989).

41. T. Ernst and J. Hennig, Double-Volume ^{1}H-Spectroscopy with Interleaved Acquisitions Using Tilted Gradients, in "Proceedings, 8th Annual Meeting of the Society of Magnetic Resonance in Medicine," Vol. 1, p. 247, Society of Magnetic Resonance in Medicine, Amsterdam, 1989.

42. U. Klose, *in Vivo* Proton Spectroscopy in the Presence of Eddy Currents, *Magn. Reson. Med.* 14, 26 (1990).

43. C. Y. Rim, J. B. Ra, and Z. H. Cho, A Single-Shot 3-D Volume Selection Technique, in "Proceedings, 8th Annual Meeting of the Society of Magnetic Resonance in Medicine," Vol. 1, p. 30, Society of Magnetic Resonance in Medicine, Amsterdam, 1989.

44. A. J. S. DE Crespigny, T. A. Carpenter, A. G. Webb, and L. D. Hall, Region of Interest Selection by Outer Volume Saturation, in "Proceedings, 8th Annual Meeting of the Society of Magnetic Resonance in Medicine," Vol. 2, p. 641, Society of Magnetic Resonance in Medicine, Amsterdam, 1989.

45. P. Mansfield, Multi-Planar Image Formation Using NMR Spin Echoes, *J. Phys. C: Sol. State Phys.* **10**, L55 (1977).

46. J. P. Felmlee, and R. L. Ehman, Spatial Presaturation: A Method for Suppressing Flow Artifacts and Improving Depiction of Vascular Anatomy in MR Imaging, *Radiology* **164**, 559 (1987).

47. A. R. Young, G. M. Bydder, and D. J. Bryant, Problems with Achieving Saturation Using Methods Based on Burst of rf Pulses with Spoilers in Magnetic Resonance Imaging, *Magn. Reson. Med.* **11**, 127 (1989).

48. L. Axel and L. Dougherty, MR Imaging of Motion with Spatial Modulation of Magnetization, *Radiology* **171**, 841 (1989).

49. P. J. Hore, A New Method for Water Suppression in the Proton NMR Spectra of Aquous Solutions, *J. Magn. Reson.* **55**, 283 (1983).

50. S. Conolly, D. Nishimura, and A. Macovski, *IEEE Trans. Med. Imaging*, MI-5, 106 (1986).

51. J. T. Ngo and P. G. Morris, General Solution to the NMR Excitation Problem for Noninteracting Spins, *Magn. Reson. Med.* **5**, 217 (1987).

52. E. D. Becker, "High Resolution NMR," Academic Press, 1980.

53. H. Y. Carr, and E. M. Purcell, Effects of Diffusion on Free Precession in Nuclear Magnetic Resonance Experiments, *Phys. Rev.* **94**, 630 (1954).

54. S. Meiboom, and D. Gill, Modified Spin-Echo Method for Measuring Nuclear Relaxation Times, *Rev. Sci. Instrum.* **29**, 688 (1958).

55. R. L. Vold, R. R. Vold, and H. E. Simon, Errors in Measurements of Transverse Relaxation Rates, *J. Magn. Reson.* **11**, 283 (1973).

56. S. Singh, B. K. Rutt, and C. P. S. Taylor, Accurate Measurement of Proton Relaxation Times From a Localized Volume, *Magn. Reson. Med.* (submitted).

57. W. A. Edelstein, G. H. Glover, C. J. Hardy, and R. W. Redington, The Intrinsic Signal-to-Noise Ratio in NMR Imaging, *Magn. Reson. Med.* 3, 604 (1986).

58. A. P. Crawley, and R. M. Henkelman, Errors in T_2 Estimation Using Multislice Multiple Echo Imaging, *Magn. Reson. Med.* 4, 34 (1987).

59. S. Majumdar, and J. C. Gore, Effects of Selective Pulses on the Measurement of T_2 and Apparent Diffusion in Multiecho MRI, *Magn. Reson. Med.* 4, 120 (1987).

60. B. R. Rosen, I. L. Pykett, and T. J. Brady, Spin Lattice Relaxation Time Measurements in Two-Dimensional Nuclear Magnetic Resonance Imaging: Corrections for Plane Selection and Pulse Sequence, *J. Comp. Assist. Tomog.* 8, 195 (1984).

61. T. Morrone, Errors in Spin-Lattice Relaxation Time Measurements from Restricted Volumes, *Magn. Reson. Med.* 5, 434 (1987).

62. D. C. Look, and D. R. Locker, *Rev. Sci. Instrum.* 41, 250 (1970).